Engineering plasmonic bimetallic nanostructures for energy conversion

Matias Herran

München 2023

Engineering plasmonic bimetallic nanostructures for energy conversion

Matias Herran

Dissertation
to obtain the doctoral degree of natural sciences (Dr. rer. nat.)
at the Faculty of Physics
of the Ludwig–Maximilians–Universität
München

submitted by
Matias Herran

13th of February, 2023
München

First Examiner: Prof. Dr. Emiliano Cortes
Second Examiner: Prof. Dr. Thomas Bein
Day of oral examination: 29/03/2023

List of Publications, Conferences and Awards

Scientific Publications of Results Presented in This Work

- S. Ezendam., **M. Herran**, L. Nan, C. Gruber, Y. Kang, F. Gröbmeyer, R. Lin, J. Gargiulo, A. Sousa-Castillo, and E. Cortés.

  Hybrid Plasmonic Nanomaterials for Hydrogen Generation and Carbon Dioxide Reduction

  ACS Energy Letters 7(2), 778-815. (2022)

- **M. Herran**, A. Sousa-Castillo, C. Fan, S. Lee, W. Xie, M. Döblinger, B. Auguié and E. Cortés

  Tailoring Plasmonic Bimetallic Nanocatalysts Toward Sunlight-Driven H2 Production

  Advanced Functional Materials 32(38), p.2203418. (2022)

- J. Gargiulo, **M. Herran**, I.L. Violi, A. Sousa-Castillo, L.P. Martinez, S. Ezendam, M. Barella, H. Gieseler, R. Grzeschik, S. Schlücker, S.A. Maier, F.D. Stefani and E. Cortés.

  Single particle thermometry in bimetallic plasmonic nanostuctures

  Nature Communications (2023) *under review*

- **M. Herran**, S. Jürgensen, M. Kessens, D. Hoeing, A. Köppen, A. Sousa-Castillo, W.J. Parak, H. Lange, S. Reich, F. Schulz and E. Cortés.

  Plasmonic Bimetallic Two-Dimensional Supercrystals for H_2 Generation

  (2023) *Submitted*

Patent

- **M. Herran**, Dr. Florian Schulz and Prof. Dr. Emiliano Cortés

  Embedding of catalytically active nanoparticles into superstructures of plasmonic nanoparticles to enhance the photocatalytic activity

  Registration number: 22 186 109.9 (2022)

Additional publications of my time as a PhD student

- Q. Wang, K. Liu, K. Hu, C. Cai, H. Li, **M. Herran**, Y.R. Lu, T.S. Chan, C. Mao, J. Fu, S. Zhang, Y. Liang, E. Cortés and M. Liu

  Attenuating metal-substrate conjugation in atomically dispersed nickel catalysts for electroreduction of CO_2 to CO

  Nature Communications 13, 1, 6082 (2022)

- M.Y. Paredes, L.P. Martinez, B.C. Barja, M.C. Marchi, **M. Herran**, G. Grinblat, A.V. Bragas, E. Cortés and A.F. Scarpettini.

  Efficient method of arsenic removal from water based on photocatalytic oxidation by a plasmonic–magnetic nanosystem

  Environmental Science: Nano 10, 166 - 177. (2023)

Conferences and Workshops

- *10^{th} SolTech Conference* (Talk)
  München, Germany. November 2021.
- *Workshop on Light: Its Nature and Its Use* (Poster)
  Venice, Italy. May 2022.
- *London Plasmonic Forum*(Talk) London, UK. June 2022.
- *Gordon Research Conference on Noble Metal Nanoparticles* (Poster)
  Massachusetts, USA. June 2022.
- *INASCON Conference* (Talk)
  München, Germany. August 2022.
- *Workshop Bridging the Gap: Nano Meets Quantum, CeNS* (Poster)
  Venice, Italy. September 2022.
- *Particle Based Materials Symposium* (Talk)
  Erlangen, Germany. October 2022.

Awards

- CeNS Travel Award

Zusammenfassung

Durch die Kombination von plasmonischen Nanopartikeln mit katalytischen Metallen kann eine neue Klasse von Photokatalysatoren hergestellt werden, die sowohl die Prinzipien der optischen als auch der heterogenen Katalyse vereint. In dieser Konfiguration werden die chemischen Reaktionen, die in der katalytischen Komponente stattfinden, durch sichtbares Licht angetrieben, das von plasmonischen Nanopartikeln fokussiert wird. Eines der Hauptanliegen dieser Hybride ist es, zu verstehen, wie die Energie vom plasmonischen auf das katalytische reaktive Zentrum übertragen wird, was notwendig ist, um die Vorteile dieser Kombination zu maximieren. Angeregte Ladungsträger, elektromagnetische Felder und sogar Wärme sind im Wesentlichen die Mittel, mit denen die Energie an das reaktive Zentrum übertragen werden kann. Diese Wege hängen davon ab, wie die Materialien miteinander interagieren; so ist für den Ladungstransfer oder die Wärmeübertragung eine Grenzfläche erforderlich, während für andere Wege ein Zwischenraum zwischen den Komponenten geschaffen werden muss.

Es ist von zentraler Bedeutung zu bestimmen, welcher dieser Wege die Leistung plasmonischer bimetallischer Photokatalysatoren moduliert, um eine maximale Effizienz bei der Umwandlung von Licht in chemische Energie zu erreichen. In diesem Zusammenhang wurden im Rahmen dieser Arbeit die folgenden Aspekte plasmonischer bimetallischer Systeme untersucht:

- Die Struktur-Performance-Korrelation
- Fähigkeit, Licht in Wärme umzuwandeln
- Der Übergang von einer kolloidalen Suspension zu einer 2D-planaren Konfiguration mit optimierter Geometrie, die die Licht-Katalysator-Interaktion verstärkt.

Unsere Beobachtungen deuten darauf hin, dass die Strukturen, in denen das katalytische Metall in einem Abstand von weniger als einem Nanometer zum plasmonischen Nanopartikel (Antennen-Reaktor) positioniert ist, einen höheren Anstieg der Reaktionsraten bewirken können. Neben der geringen Beeinträchtigung der optischen Eigenschaften sind die plasmonischen Nanopartikel in der Lage, über die Bildung optischer Hotspots die ansonsten geringe Absorption der katalytischen Metalle im sichtbaren Bereich zu erhöhen. Durch die Wechselwirkung mit Licht werden angeregte Ladungsträger in der Nähe der Adsorbat-Reaktor-Grenzfläche erzeugt, die für die adsorbierten Moleküle nutzbar gemacht werden können, um deren Umwandlung zu erleichtern. Die thermische Analyse hat gezeigt,

dass die Wärmeabgabe der plasmonischen Antenne nicht ausreicht, um den Reaktionsschub bei Sonneneinstrahlung zu erklären, was uns zu dem Schluss kommen ließ, dass die angeregten Ladungsträger ein wesentlicher Faktor für die Ratenerhöhung sind. Schließlich wurde die bevorzugte Konformation zu einem 2D-Superkristall erweitert, der eine große Dichte an Hotspots aufweist, die von den katalytischen Metallen genutzt werden können. Beim Testen dieser Struktur für die Dehydrierung von Ameisensäure führte sie zu einer der größten Produktionen, die bisher für diesen H_2-Träger berichtet wurden.

Summary

A new class of photocatalysts gathering both optical and heterogeneous catalysis principles can be produced by combining plasmonic nanoparticles with catalytic metals. In this configuration, chemical reactions taking place in the catalytic component are powered by the visible light focused by plasmonic nanoparticles. Understanding how energy is transferred from the plasmonic to the catalytic reactive center, necessary to maximize the benefits of this combination, is one of the main concerns of these hybrids. Excited carriers, electromagnetic fields, and even heat are essentially the means by which the energy can be delivered to the reactive center. These pathways strongly depend on how the materials interact; for instance, charge transfer or heat transfer pathways require the presence of an interface, while other pathways need the construction of a gap between the components.

It is central to determine which of these pathways modulates the performance of plasmonic bimetallic photocatalysts in order to obtain the maximum efficiency on converting light into chemical energy. In this regard, the following aspects of plasmonic bimetallic systems were investigated in the course of this thesis:

- The structure-performance correlation
- Ability to convert light into heat
- The transition from a colloidal suspension to a 2D planar configuration with optimized geometry, boosting the light-catalyst interaction.

Our observations point out that those structures in which the catalytic metal is positioned at sub-nanometer distance with respect to the plasmonic nanoparticle (antenna-reactor), are able to produce a higher boost in reaction rates. In addition to the little detriment of the optical properties, the plasmonic nanoparticles are able to increase the otherwise small absorption of the catalytic metals in the visible range via optical hotspots formation. As a result of the interaction with light, excited carriers are generated in proximity to the adsorbate-reactor interface, where can be utilized for the adsorbed molecules to facilitate their transformation. Thermal analysis proved that the plasmonic antenna's heat output is insufficient to account for the reaction boost at solar irradiances, which allowed us to conclude that the excited carriers are a significant factor in the rate enhancement. Finally, the preferred conformation was extended as a 2D supercrystal offering a large density of hotspots which catalytic metals can take advantage from. When testing

this structure for Formic Acid dehydrogenation, it resulted in one of the largest production reported so far for this H_2 carrier.

Contents

List of Figures

List of Tables

Chapter 1

Introduction

Over the last 50 years our society has witnessed tremendous technological advances. Digital telecommunications, smart cars, the possibility to pinpoint our locations and navigate around the globe within seconds, or the internet itself are just a few examples of these outstanding inventions. However, and unfortunately, all these industrial developments come at a price. The energy demands to manufacture products present in our daily life are increasing at an incredible pace, which is translated as an rise in energy consumption. [1]. The majority of this demanded energy is primarily supplied by the combustion of fossil fuels (making up to 80% [1]), a common denomination to group carbon-based products such as oil, gas and coal. The excessive amount of greenhouse as a result of burning fossil fuels suppose one of the greatest challenges we are facing nowadays, the global warming [2]. The reason relies on the large emissions of CO_2, which regulates the temperature of the Earth by trapping sunlight radiation within the atmosphere [3, 4]. Nowadays, the concentration of CO_2 overcome 400 ppm and is the largest recorded ever [5].

To mitigate the current situation, the focus has been set on decarbonizing the economies by 2050 [6, 7], motivating thus the search of alternative energy sources, such as H_2 [2], and sustainable processes that can fulfill the energy demands. Here is where **Plasmonic** nanostructures gain relevance. The boom of nanotechnology -just two decades ago- provide the ability to fabricate materials of nanometer (nm) size range with very accurate control, and the most exciting fact is that they present different properties than both the bulk or atomic counterpart. Particularly, Plasmonic Nanoparticles (PNPs), metallic nanoparticles based on gold (Au), silver (Ag), copper (Cu), Aluminium (Al), among others, exhibit a strong interaction with light within the visible range of the electromagnetic spectrum, being spectrally coincident with the maximum of emitted light by the sun.

The implementation of PNPs as photocatalysts dates approximately from 2000-2010 [8,9,10,11], giving birth to a new field of research denominated "*Plasmonic Catalysis*" [12]. Since then, numerous studies have shown their ability to administer the captured light and supply it to molecules to undergo chemical transformations, even when operating at solar irradiances [9, 13]. Lately, PNPs were combined with transition metals -active metals for catalyis-, seeking for a better exploitation of the constituents [14, 15]. In principle, this combination of materials enables to achieve a larger efficiency on allocating the solar energy

harvested by PNPs in product molecules generated in the reactive surface of catalytic metals. Therefore, one could in principle envision their application in processes where fuels (e.g. H_2) can be generated by powering bimetallic photocatalysts with sunlight.

The scope of this work relies on the interesting physical phenomena occurring in plasmonic bimetallic nanostructures, from which we can take advantage from to drive chemical reactions. In this regard, **Chapter 2** provides a robust description of the fundamental phenomena taking place when exciting PNPs with light and how the catalytic metals benefit from this. Their colloidal preparation played a major role throughout this thesis, and **Chapter 3** summarizes the thinking behind the procedures, as well as the techniques and devices employed to characterize them optical, chemical and catalitically. We proceeded by investigating (**Chapter 4**) the correlation between the spatial arrangement of constituents and its light-driven performance. To understand this further, in **Chapter 5** studies were elaborated on their ability to convert the incoming light into local heat, which helped to gain insight on its contribution to the reaction. Finally, through the knowledge gained in past studies, in **Chapter 6** a transition from colloidal suspensions to two dimensional configurations is proposed as a potential photocatalysts to boost the interaction between the incoming light and plasmonic bimetallic nanoparticles.

Chapter 2

Plasmonics: fundamentals and applications in catalysis

This chapter is dedicated to discuss the fundamental phenomena that lead to a comprehensive analysis of plasmon-driven chemical reactions. First, the chapter starts with a theoretical description in which how a quasi-static approach enables to find useful expressions to understand the excitation of Localized-Surface Plasmon Resonances (LSPR) and subsequent events. It proceeds providing an overview on how molecules can take advantage of these phenomena and undergo chemical transformation, which will help to understand the motivation on their use in catalysis. Finally, the chapter concludes with a summary of relevant findings on plasmonic-catalytic metal hybrid structures and fundamentals of their fabrication.

2.1 Localized Surface Plasmon Resonances (LSPR)

2.1.1 Quasi-static approximation

Localized surface plasmon resonances (LSPR) are oscillating modes resulting from the interaction of electromagnetic fields with sub-wavelength metallic particles ($\lambda \gg d, diamater$). These resonances arise from the fact that the nuclei exert a restoring force to the free electron cloud distorted by the driving field [16, 17]. The physical principles of LSPR will be discussed in this section, starting from the fundamental quasi-static model to finally achieve an analytical description for the particular interaction of driving electromagnetic fields and sub-wavelengths metallic particles. The description will be uniquely developed for metallic entities, although it is still valid for some highly semiconductors [18].

The quasi-static approximation describes the interaction of an isotropic sphere of diameter d interacting with a constant electric field over the dimensions of the particle [19]. Figure 2.1 depicts the described image where this sphere, surrounded by an arbitrary non-absorbing medium with dielectric constant ε_m, interacts an uniform static electric field $\mathbf{E} = \mathrm{E}_0\ \mathrm{z}$. The field lines are parallel to the z-direction at sufficient distance from the sphere.

It is known that metals are characterized by positive nuclei surrounded by unbound electrons, which move freely across the material. Hence, in response to the electric field, the metallic sphere is polarized pulling electrons towards the opposite direction of the field, forming a dipole. The response of metals is dictated by its own dielectric function (ε), which will be discussed later.

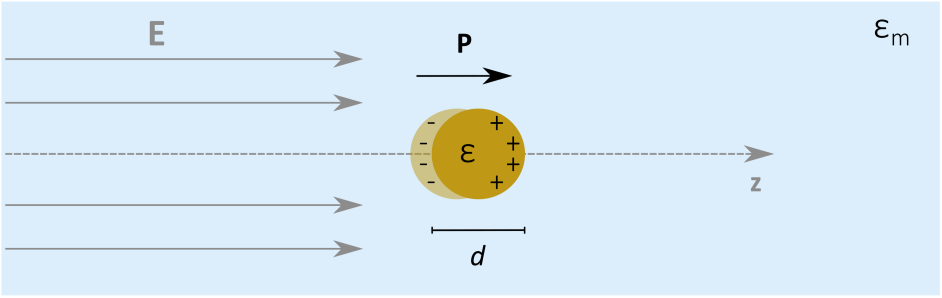

Figure 2.1: **Interaction between electric fields and metallic nanoparticles: Quasi-static approximation.**Particle of diameter d ($d<<\lambda$) embedded in an homogeneous and non-absorbing medium. The particle is polarized due to the interaction with electrostatic fields.

Because of the interaction with the metallic sphere, the electric field will be distorted. To find the spatial distribution of the electric field inside and outside the particle, Laplace equation ($\nabla^2\Phi$=0) must be solved taking into account the continuity at the interface.

$$\vec{E}_{inside} = -\nabla\Phi_{inside}, \qquad \vec{E}_{outside} = -\nabla\Phi_2 \tag{2.1}$$

where

$$\nabla^2\Phi_{inside} = 0 \quad (r < a, a = d/2), \qquad \nabla^2\Phi_{outside} = 0 (r > a) \tag{2.2}$$

The boundary conditions dictate

$$\Phi_{inside} = \Phi_{outside}, \qquad \varepsilon\frac{\partial\Phi_{inside}}{\partial r} = \varepsilon_m\frac{\partial\Phi_{outside}}{\partial r}, (r = a) \tag{2.3}$$

In addition, it is required that far from the particle the electric field is unperturbed by the particle

$$\lim_{r\to\infty}\Phi_2 = -E_0\ r\ cos(\theta) = -E_0 z \tag{2.4}$$

The solutions that satisfy the aforementioned conditions are presented in Equation 2.5 and 2.6.

$$\Phi_{inside} = -\left(\frac{3\varepsilon_m}{\varepsilon + 2\varepsilon_m}\right) E_0\ r\ cos(\theta) \tag{2.5}$$

$$\Phi_{outside} = -E_0\ r\ cos(\theta) + \left(\frac{\varepsilon - \varepsilon_m}{\varepsilon + 2\varepsilon_m}\right) E_0\ d^3\ \frac{cos(\theta)}{r^2} \tag{2.6}$$

The expression for the potential outside the particle (Equation 2.6) contains an additional term accounting for the superposition of the applied field and that of an ideal dipole, which turns out to be proportional to the applied field, **E**. Thus, the applied field induces a dipole moment proportional to the field E_0. Now the expression outside the particle is rewritten as

$$\Phi_{outside} = -E_0 \ r \ cos(\theta) + \frac{\vec{p}\cdot\vec{r}}{4\pi\varepsilon_0\varepsilon_m r^3} \ \Rightarrow \ \vec{p} = 4\pi\varepsilon_0\varepsilon_m d^3 \left(\frac{\varepsilon-\varepsilon_m}{\varepsilon+2\varepsilon_m}\right)\vec{E}_0 \tag{2.7}$$

By definition, the polarizability (α) is the ratio of the module of the induced dipole $\vec{p}$ and the module of the electric field **E** that produces that dipole. Since $\vec{p} = \alpha\vec{E}_0$, now we can define the polarizability as it follows (Equation 2.8).

$$\alpha = 4\pi\varepsilon_0\varepsilon_m d^3 \left(\frac{\varepsilon-\varepsilon_m}{\varepsilon+2\varepsilon_m}\right) \tag{2.8}$$

When analizing the expression found for the polarizability (α), it is important to stress that it depends on both, the volume of the particle ($\propto$ d^3) and also the dielectric function of the material (ε).

Now, the expression for the spatial distribution of the electric field can found by taking E = - $\nabla\Phi$, resulting in:

$$E_{inside} = \left(\frac{3\varepsilon_m}{\varepsilon+2\varepsilon_m}\right)E_0 \tag{2.9}$$

$$E_{outisde} = E_0 + \frac{3\vec{n}(\vec{n}\cdot\vec{p})-\vec{p}}{4\pi\varepsilon_0\varepsilon_m}\frac{1}{r^3} \tag{2.10}$$

One important feature must be highlighted in the expressions found for the polarizability and the electric fields. They all present a dependence on the dielectric function of the metallic particle. When analyzing them, the polarizability (α) and hence, the electric fields, maximize at the condition in which Re[ε]$\approx$ -2ε_m and Im[ε]$\approx$0 are simultaneously met. This finding establishes one of the fundamental conditions for materials to support LSPR, that is: only materials with negative dielectric functions can support these modes [16]. Due to the nature of free conducting electrons, which move in the opposite direction than the incoming field, metals present a negative dielectric function, being suitable materials for LSPR excitation. Typically, the negative dielectric function of metals is not constant and presents a dependence with the frequency of the incoming electric field, thus $\varepsilon = \varepsilon(\omega)$, as well as, $\alpha = \alpha(\omega)$. The Drude model, presented in Appendix A, enables to find an expression for the dielectric function of metals which is shown in Equation 2.11. The plasma frequency in Drude's model is a reference value of frequencies at which the free electrons of the metals stops following the electric field and from that value on, they are considered *"transparents"* [20]. However, it is known that this classical approach breaksdown at higher frequencies and other processes such as photoelectron emission can occur [21]. Moreover, γ accounts for the resistance to the move of the free electron cloud (*damping*).

$$\varepsilon(\omega) = 1 - \frac{\omega_{plasma}}{\omega + i\gamma\omega} \tag{2.11}$$

Once described the quasi-static model, we can move on to the interaction between sub-wavelengths particles and driving fields. Electromagnetic radiation is considered as waves that vary in both, time and space. An electric field in the form of a plane wave $E(\omega) = E_0 \exp^{-i\omega t}$ induces a dipole in the form of $p = \varepsilon_m \alpha(\omega) E_0 \exp^{-i\omega t}$. The dipolar oscillation of the sub-wavelength particle reaches its maximum amplitude when the Re[ε]≈ -2ε_m and Im[ε]≈0. As we are under the condition that $\lambda \gg d$, the assumption that the entire particle is polarized homogeneously still remains, neglecting retardation effects. The induced polarization of the particle due to the driving field is shown in Fig 2.2.

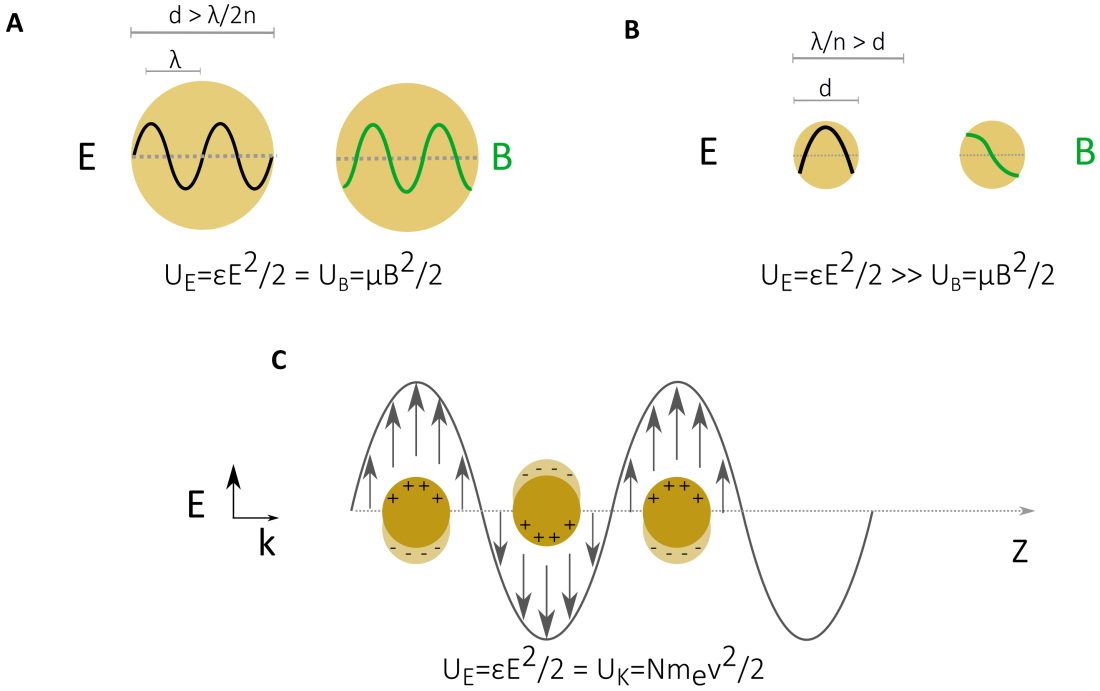

Figure 2.2: **Self-sustained oscillations and LSPR.(A)** Particle interacting with electromagnetic driving field when d> λ. The energy is continuously exchanged between electric and magnetic fields, making self-sustained oscillation possible. **(B)** Similar interaction but now in a regime at which the particle is smaller than wavelength (d< λ). **(C)** Sub-wavelength particle interacting with electromagnetic driving field. The energy balance is restored since electric energy is converted in kinetic energy of the conduction electrons. **(A)** and **(B)** adapted from [22].

The formation of an oscillating dipole suggest that the free electrons gain energy to move in a certain direction. Therefore, it is worth to analyze how is this interaction from the energy point of view. Travelling electromagnetic waves carry energy which is periodically exchanged from electric (E) to magnetic fields (B) in every half-cycle, always satisfying u=u_E+u_B. Similarly to what occurs in vacuum, if the particle of diameter

d is large enough for the wave to complete a cycle ($d > \lambda/\eta$, Figure 2.2A), the stored energy is transferred from the electric field $u{=}u_E \sim E\varepsilon^2/2$ to the magnetic field $u{=}u_B \sim B\mu^2/2$ in every half-cycle. Nevertheless, the particle is smaller than the wavelength ($d << \lambda/2\eta$), so that the field spatial dependence should become $\sin(\pi z/d)$, making self-sustaining oscillations impossible due to the energy imbalance ($u_E \gg u_H$, Figure 2.2B). However, the free electrons offer an alternative way to store energy in a form collective motion (Kinetic energy, $u_K \sim 1/2\ \varepsilon_0(\omega_{Plasmon}/\omega)^2E^2$) and thus restore the energy balance (Figure 2.2C) [22]. At the frequencies at which the polarizability maximizes, more energy is transferred to the oscillating electrons. Unfortunately, the possibility to allocate energy in the collective motion of free electrons comes at a price. Similar to what occurs in the harmonic oscillator, if there were no losses (leak of energy from the system), the energy would be transferred from the electrons to the E fields and then back to the electrons. However, the inherent collisions among the electrons themselves, as well as with the lattice, determine the finite lifetime these self-sustained oscillations. We will further discuss the mechanisms by which the energy is dissipated in the following sections.

To summarize, the formalism developed in this section enabled to find basic expressions to understand the so-called LSPR. Electromagnetic driving fields can transfer energy to the free electron clouds of sub-wavelength metallic particles by forcing them to move collectively. The remaining positive background exerts a force that pulls them back towards the nuclei, giving rise to a resonant behaviour. As a result of the interaction, the intensity of the electric field at the surface of the particles is enhanced with respect to the incoming one. The enhancement of the electric field is the reason why plasmonic particles were vastly employed in the broad field of spectroscopies and microscopies [23].

2.1.2 Optical properties of sub-wavelengths particles

The transfer of energy from the electromagnetic wave to the free electron of the metals and the associated losses manifest as an extinction of light. This extinction has two main contributions which are the *Scattering* and the *Absorption* (transformation of electromagnetic energy into other forms), both depicted in Figures 2.2A and B. The scattering can be understood as a deviation of the path of the light upon encounter with the particle, while the absorption is indeed more complicated and involves promotion of electrons to excited states. We will further describe this in Section 2.1.3. Expressions for the extinction, absorption and scattering cross-sections (σ) can be found by evaluating the flux of the poyinting vector, which describes the balance between the input and output of energy. The reader is referred to reference [19] for the thorough analysis. The expressions are presented in Equations 2.12, 2.13 and 2.14.

$$\sigma_{Absorption} = k \times Im[\alpha] = 4\pi k \left(\frac{d}{2}\right)^3 Im\left[\frac{\varepsilon(\omega)\varepsilon_m}{\varepsilon(\omega) - 2\varepsilon_m}\right] \tag{2.12}$$

$$\sigma_{Scattering} = \frac{k^4}{6\pi}|\alpha|^2 = \frac{8\pi}{3}k^4\left(\frac{d}{2}\right)^6 \left|\frac{\varepsilon(\omega) - \varepsilon_m}{\varepsilon(\omega) - 2\varepsilon_m}\right|^2 \tag{2.13}$$

$$\sigma_{Extinction} = \sigma_{Absorption} + \sigma_{Scattering} = 9\frac{\omega}{c}\varepsilon_m^{3/2}V\frac{\varepsilon_2}{(\varepsilon_1 + 2\varepsilon_m)^2 + \varepsilon_2^2} \tag{2.14}$$

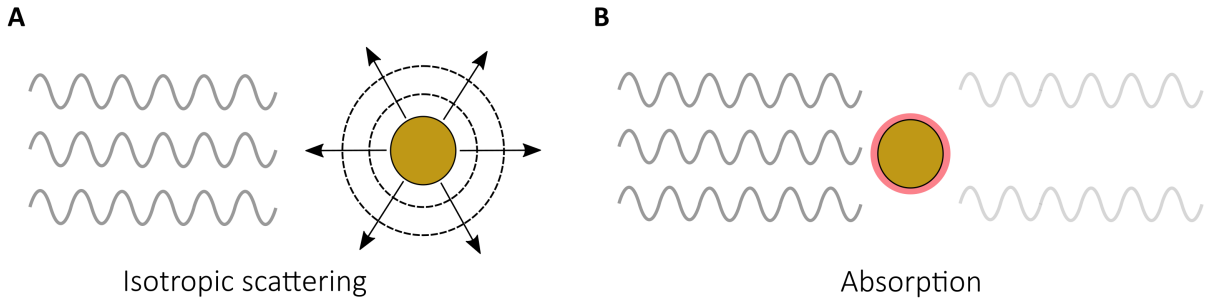

Figure 2.3: **Scattering and Absorption(A)** Scattering of light in all directions by particles smaller than the wavelength. **(B)** Absorption of light by NPs smaller than the wavelength.

The terms ε_1 and ε_2 correspond to the real and imaginary part of the dielectric function found in Drude model ($\varepsilon(\omega) = \varepsilon_1 + i\varepsilon_2$). The absorption scales with d^3, while the scattering does it with d^6, therefore it is expected that the former governs for smaller particles, whereas the scattering becomes the dominant one for larger particles, as summarized in Figure 2.4. The extinction cross-section ($\sigma_{Extinciton}$) given by Equation 2.14 for 10, 50 and 100 nm Au spherical particles are shown in Figure 2.4A, at which it can be realized that there is a factor of 10^2 between the smallest and the largest sizes. However, the ratio between the absorption and the scattering contributions is not constant throughout the size range, as expected from Equations 2.12 and 2.13. Indeed, the scattering grows larger as the particles increase in size (illustrated in Figure 2.4B).

A very remarkable effect occurs due to the resonant nature of the particles. At those frequencies at which the polarizabilty (α) is maximized, sub-wavelength particles exhibit optical cross-section ($\sigma_{Absorption}$) exceeding the geometrical cross-section by more than one order of magnitude ($\sigma_{Extinciton}/\pi a^2 > 1$). The reason for this outstanding effect is because when illuminating them on-resonance the electromagnetic waves are strongly deviated, finally converging towards the particle. This phenomenon is well-known for macroscopic objects and is denominated "Antenna Effect". Figure 2.5 shows the field lines of the Poynting vector (excluding that scattered) for a particle illuminated on and off-resonance, depicting the above described effect. At the LSPR frequency, the fields deflect towards the nanoparticle, resulting in a greater extinction of light with respect to the off-resonance situation in which the field would pass by without any impediment nearby the particle [24].

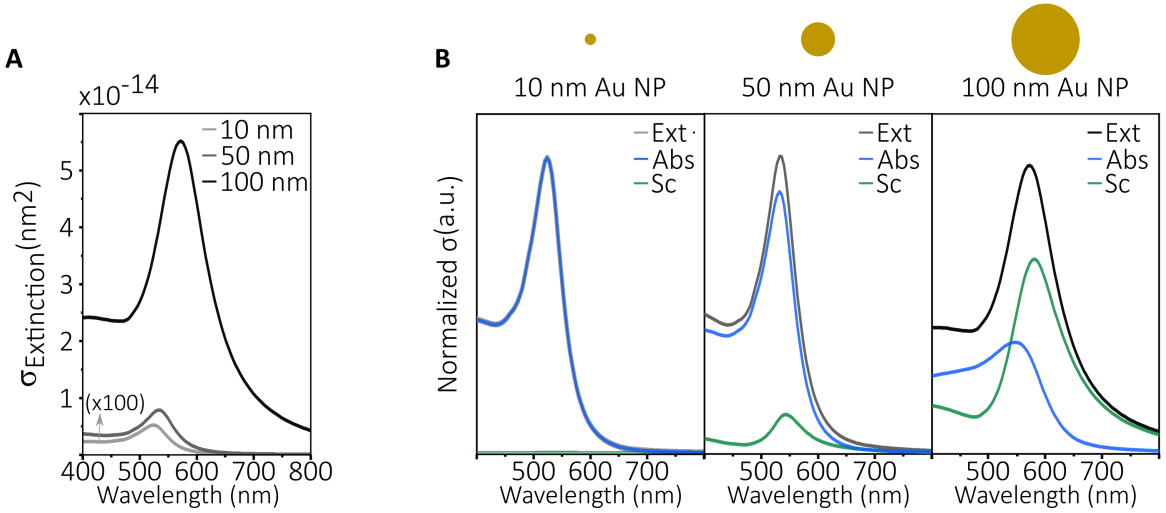

Figure 2.4: **Size dependence in extinction, absorption and scattering of spherical Au NPs** **(A)** Extinction cross-section ($\sigma_{Extinciton}$) of 10, 50 and 100 nm Au NPs. $\sigma^{10nm}_{Extinciton}$ is was multiplied by 100. **(B)** absorption and scattering contributions to the extinction for the abovementioned particles. The absorption dominates for small particles, while the scattering does it for larger (∼100 nm) particles

All the features described so far for LSPR are valid for sphere-like particles. However, this approach breaks down either when the size of the particle is comparable to the wavelength (giving rise to higher order modes e.g. quadrupole) or the particle has an anisotropic shape (rod-like, triangle, stars, etc.) [25]. For a more accurate description we have to dive into Mie theory, which delivers analytical formulae for the aforementioned expressions. However, this goes beyond the content needed to describe the findings of this work and classical books are referred to Reference [26].

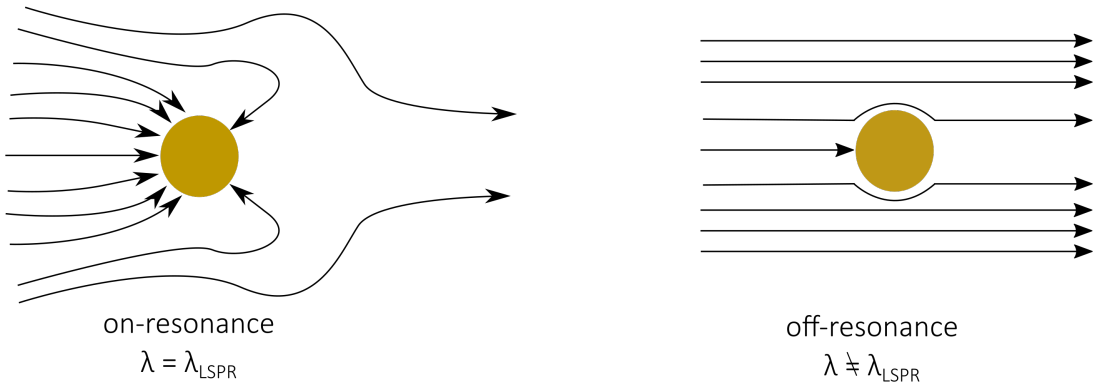

Figure 2.5: **Antenna Effect.** When subwavelengths particles are irradiated with light at LSPR conditions, the trajectory of the Poynting vector is deviated towards the particle, resulting in a large optical cross-section, several order of magnitude than the geometric one. Nevertheless, only the that go straight to the particle interact with it when the wavelength dismatch the LSPR (off-resonance). Adapted from [24]

2.1.3 Dynamics and losses in LSPR

The strong interaction of light and PNPs enables to allocate energy in the collective motion of conduction electrons of the metal. Similar to what occurs in a harmonic oscillator, energy goes back and forth between the kinetic energy of the electrons and the energy allocated in the electric field. Nevertheless, LSPR possesses a limited lifetime - in the order of femto- to picoseconds regime - since the energy stored as kinetic kinetic energy is damped at a rate commensurate to the electron-electron (γ_{e-e}) and electron-phonon (γ_{e-ph}) scattering rates. The *losses*, identified as the leak of energy stored in LSPR will be described in this section. The description will be carried out more in a quantum approach, instead the classic description employed so far.

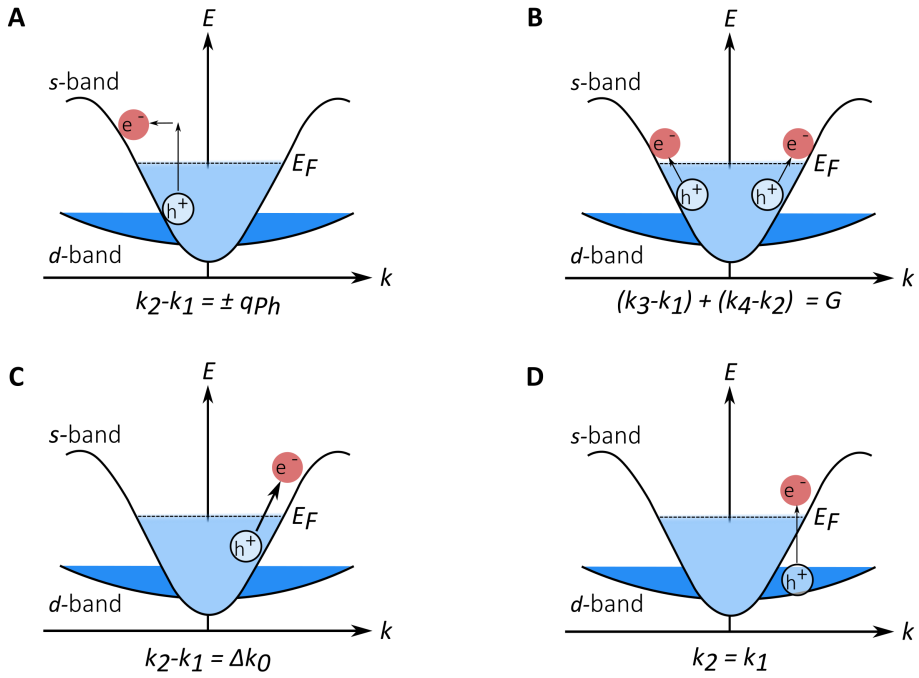

Figure 2.6: **Plasmon absorption(A)** Phonon-assisted intraband transition. The phonon supplies the demanded momentum for the transition. Generates one hot hole and one hot electron. **(B)** Electron-electron scattering, which provides two holes and two electrons with approximately $\hbar\omega/4$. **(C)** Landau damping **(D)** Inter-band transition. This transition do not require external momentun and generate a hot hole and an electron right above the Fermi level. Adapted from [22].

The absorption of a plasmon is a more complex phenomenon which triggers a set of cascade effects relevant for catalysis applications [27]. The absorption of photons can take place by means of different ways, all summarized in Figure 2.6 and described as follows.

Typically, the electronic properties of plasmonic metals are characterized by a Fermi Level (highest occupied level, E_F) located in a *s*-band with a deep lying and fully occupied *d*-band, as illustrated. Essentially, there are four ways for electron promotion to excited states [22], which can be grouped into two categories: *Intraband* and *Interband* transitions.

The former typically refer to s-to-s promotions, which are proved to demand moment conservation. One way to accomplish such transition is by acquiring momentum from a phonon (Figure 2.6A), which yields two carriers (hole and electron) far from the energy of the Fermi level, meaning with larger energy with respect to the one dictated by the thermal energy. This is the reason why in the literature these are known as hot carriers ($\hbar\omega \gg k_B T$). Alternatively, what can occur is that two electrons are promoted to excited states via electron-electron scattering, although unlike the past example it generates two electrons and two holes with energies right above and below the Fermi-level. Since the energy of the incident photon is shared between all carriers ($\hbar\omega/4$), this mechanism leads to the creation of excited carrier with comparatively lower energy.

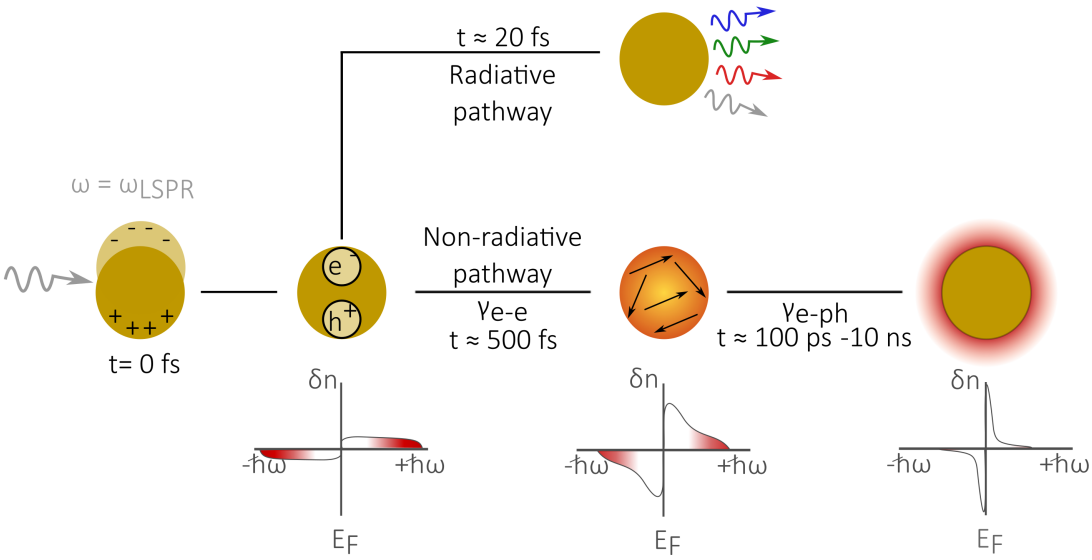

Figure 2.7: **Dynamics in LSPR decay.** The energy stored in the collective motion of the conduction electrons ends up in the generation of excited carriers (holes and electrons). The electron-hole pair can decay either radiatively in the first ∼20 fs, in which either a resonant, stokes or anti-stokes photon can be emitted (photoluminescence), or non-radiatively via electron-electron scattering. The colission of excited carriers among themselves leads to a distribution of the energy of electrons which can be fit with a Fermi-Dirac distribution (∼ 500 fs). The energy is further dissipated through electron-phonon scattering, which ends up releasing heat towards the near environment, thus restoring the initial situation (∼10 ns). Adapted from [28] and [29].

The third mechanism is a diagonal process acknowledged as *Landau damping*. The occurrence of photon absorption is due to the presence of surface plasmon polaritons (SPP), which deliver the requested moment for the transition [22]. The mechanism results in a hot electron and hot hole. Last one, involves the so-called *Interband* transitions, at which electrons are promoted from bands with lower energy (often d-bands) to bands with higher energy (s-band) as shown in Figure 2.6D). The *d-to-s* transitions yield electrons with low energy (right above the Fermi Level, while generate an energetic hole and are straight transitions, meaning that they do not require any additional source to supply

any moment. In addition to the imaginary part of the metal, the probability of plasmon absorption for metallic nanoparticles is proportional to the square of the electric field ($Absorption \propto |E_{inside}|^2$) inside the NP [28,30,31], as it will be shown later in Section 2.2.2. Upon resonant illumination, it is dramatically enhanced due to the antenna effect [24].

The non-thermalized electrons created when illuminating on-resonance, can decay either *radiatively*, by the re-emission of photons to the far-field or *non-radiatively*, via heat generation [28]. These pathways are summarizes in Figure 2.7. The radiative pathway consist on the emission of photons upon carriers recombination, often refer to as photoluminescence [32]. Similar to what occurs in molecules, photons with lower, equal or larger energy can be emitted [33, 34, 35, 36], being named accordingly. The ones with larger or smaller energy are denominated as *Anti-stokes* and *Stokes* photons (coloured arrows in sketch), respectively. Alternatively, if the radiative pathway does not occur, the energy input is lost in a non-radiative pathway. It involves the collision of excited electron among themselves (electron-electron scattering, γ_{e-e}), which occurs between the first hundreds of femtoseconds. The electron-electron scattering redistribute the energy, giving rise to a thermalized distributions of excited carriers nearby the Fermi Level, which correspond to a Fermi-Dirac distribution for electrons. The energy is further dissipated via excitation of low-energy vibrational modes of the crystal (acoustic phonons). The electron-phonon scattering (γ_{e-ph}) take place around $\sim$ 100 ps - 10 ns after excitation. Ultimately, heat is released towards the local environment, restoring the initial situation of the nanoparticle, prior to LSPR excitation. A sketch on carriers energy distribution is shown at the bottom of Figure 2.7, in illustrating each of the steps described above [29, 37].

$$\Delta\omega = \gamma = \sum_i \tau_i^{-1} = \tau_{e-e}^{-1} + \tau_{eh}^{-1} \tag{2.15}$$

All these steps were deeply investigated via time-resolved spectroscopy and were helpful to understand the mechanism governing the relaxation of the stored energy into the collective motion of the conduction electrons of metallic sub-wavelengths nanoparticles [32]. The losses can be now all integrated into a single expression for γ, the damping constant in Drude model (Equation 2.15). Similar to what occurs for a harmonic oscillator interacting with a driving force, the damping constant is correlated to the bandwidth of the resonance. The more the channels for the energy to dissipate, the broader the resonance. The Q-factor ($Q=\omega/\Delta\omega$) was defined as a metric for the quality of the resonator, since it accounts for how much energy is dissipated in each oscillation cycle [38].

Hotspots The ability to squeeze light into sub-wavelengths scales is greatly boosted when the distance between to adjacent PNPss is reduced down to a few nanometers (5-30 nm). The fact that the free electron oscillation of adjacent PNPs can couple at such distances results in the formation of optical hotspots along the axis of the dimer [39, 40]. Typically, the dimers present two resonances, transversal (perpendicular) and longitudinal (parallel) to the dimer axis. While the spectral position of the transversal mode resemble the resonance of a monomer, indicating a poor coupling between the antennae, the lon-

gitudinal mode is red-shifted. The coupling results in a remarkable enhancement on the intensity of the electric field ($\sim 10^4$ times), affecting dramatically its spatial profile. For example, for spherical monomers, the field enhancement when the dipolar mode is excited mainly occurs at the edges for the nanoparticles, as illustrated in the top panel in Figure Figure 2.8A. Nevertheless, when dimerized, the intensity of the electric field enhancement is greatly boosted and confined to the interparticle gap (bottom panel Figure 2.8A). The electric field enhancement, as well as the red-shift, strongly depends of the gap in the dimer (Figure Figure 2.8B) [41, 42].

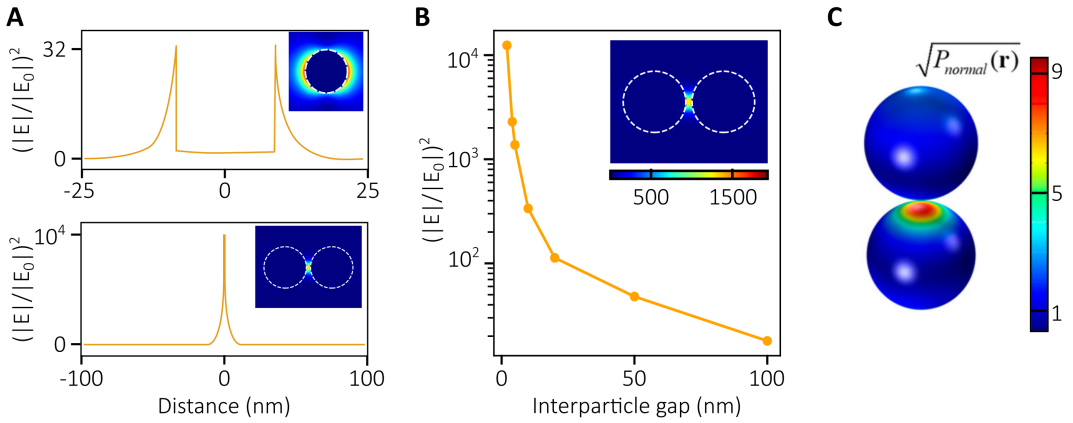

Figure 2.8: **Optical hotspots. (A)** Top: Electric field intensity profile across the center of a single PNP. Bottom: Electric field intensity profile along the axis of a dimer comprised by two indistinct PNPs. The intensity of the electric field is amplified in a factor of 10^4 and is strongly confined at the gap between the monomers. **(B)** Interparticle gap dependence of the electric field intensity at the hotspot. **(C)** Absorbed power map for a dimer showing the local effects. Due to the larger confinement of the electri field, a larger local absorption rate is seen at the hotspot. Adapted from [43, 44]

The larger confinement of the field to the interparticle gap has also an impact on hot carriers generation. Due to the $\mathbf{E}_{in}^2$ dependence, a large fraction of the total hot carriers within the nanoparticles can be locally generated at the optical hotspots, confirming the correlation between larger confinement with the increased local absorption on the nanoparticles [29,45]. This even occurs in spite of the very little surface exposed by each monomer. Figure 2.8C shows the absorbed power when the longitudinal mode is excited for a dimer comprised of two equal Au nanospheres, representing the local hot carriers generation rate. Therefore, optical hotspots can serve as active sites for molecules to pick up carriers and undergo chemical transformations [46, 47, 48]. The biggest limitation is that the hotspots area represents a low percentage of the total surface area, therefore engineering the hotspots is definitely an appealing direction for the field to progress.

2.2 Plasmonic NPs in catalysis

Chemical reactions have different natures, for instance, while dissociation reactions demands the bond between atoms to be activated and elongated to promote its scission, Reduction and Oxidation (redox) reactions involve the exchange of electrons to form products. Until now, we know that the resonant illumination of metallic nanoparticles with sub-wavelengths dimensions yields the generation of enhanced electric fields, energetic electrons and holes and local heat. Hence, the utilization of PNPs in catalytic processes seems to be straightforward, since all these subsequent processes after LSPR excitation can be beneficial to trigger chemical reactions. For example, elevated temperature at the surface of nanoparticles can activate the bonds or the hot carriers can be injected into molecules [11].

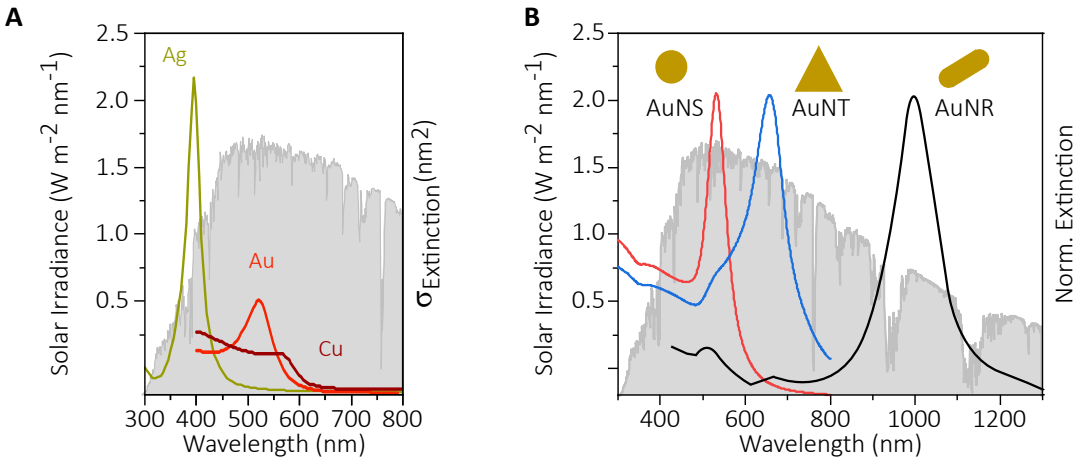

Figure 2.9: **PNPss as solar energy harvesters. (A)** Overlap between the solar irradiance and the dipolar LSPR of 10 nm Ag, Au and Cu NPs. the sun serves as a source of light, while the PNPs are materials that harvest the solar energy and transduce into chemical energy. **(B)** LSPR of Au NPs with spherical, triangular and rod-like shapes. The manipulation of the shape enables to access up to the NIR region of the sun's emission spectrum. **(A)** Adapted from [43].

The perfection on nanomaterial's synthesis and light manipulation properties of PNPs gave rise to a new field in which they can operate as photocatalysts harnessing light to assist chemical transformations. In this regards, most of attention was received by Silver (Ag), Gold (Au) and Copper (Cu) owing to the presence of their resonances within the visible spectral region, which are coincident with the peak of sunlight emission (Figure 2.9A), and their relative low losses [49]. Precisely, Ag and Au were extensively explored due to their stronger interaction with light. Indeed, the broad tunability of the size and shape of Au- and Ag-based nanomaterials (e.g. nanorods, nanotriangles) enabled to even access to Near Infrared (NIR) via the new resonances arising with the different shapes (Figure 2.9B) [50, 51, 52].

First reports on PNPs in photocatalysis date from almost ten years ago [9,10,11,53] and since then, the field of Plasmonic Catalysis grew fast due to the systematic boost on reaction rates upon LSPR excitation. Due to the fact that PNPs can operate a solar irradiances [9],

the field pursued the goal to utilize the sun as a source of light, converting its emitted energy into a valuable compounds to our society. In this configuration, the sun operates emitting a large number of photons of different energies, and PNPs serve as harvesters due to their boosted absorption at resonance [24]. Finally, through the generation of enhanced electric fields, hot carriers and local heat, they can facilitate chemical reactions.

There is not a single way in which a molecule can undergo a transformation with the assistance of LSPR. In this regard, several studies were conducted to elaborate on the mechanisms by means of which the molecules are activated. Here, the three most often reported mechanisms will be briefly discussed stressing the main differences among them.

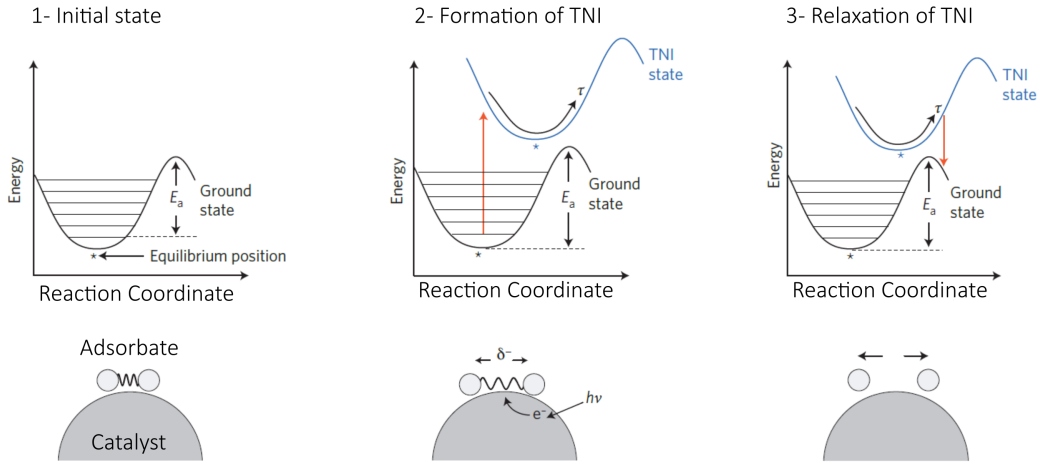

Figure 2.10: **Transient Negative Ion formation** The initial state illustrates the interaction of a molecule adsorbed at the surface of a PNPs. Upon illumination, an excited electron is pumped into the anti-bonding orbitals of the molecule, forming a Transient Negative Ion (TNI). The energy supplied by the electron forces the molecule to move in a excited PES. Once the electron is retrieved to the metal, the adsorbate goes back to the ground state, but with additional energy to overcome the activation barrier for its dissociation. Adapted from [10].

2.2.1 Hot carriers

The highly energetic carriers generated upon plasmon excitation has a lifetime of ∼20 fs until they start losing energy, while chemical reactions usually occur at longer times [54]. However, a steady state can be achieved under continuous illumination and thus, both electrons and holes can assist the molecules undergoing chemical transformations [55]. All explored reactions assisted by hot carriers so far can fit into the three general mechanisms discussed below.

Transient Negative Ion This mechanism picks up concepts of Desorption Induced by Electronic Transitions (DIET) and Desorption Induced by Multiple Electronic Transitions (DIMET) to mainly describe how dissociative molecular reactions occur at the surface of

PNPs upon LSPR excitation [10, 56, 57]. It involves the scattering of excited electrons to the adsorbed molecules at the surface of the NPs for a very short period of time, typically $\sim$ 10-20 fs. The entire mechanism is presented in Figure 2.10. Specifically, upon LSPR excitation, electrons are pumped into the anti-bonding molecular orbitals forming a transient negative ion (TNI) or transient anion. With the energy provided by the excited carrier, the TNI is transferred to a higher potential energy surface (PES), in which the equilibrium distance between atoms is elongated in comparison with the ground state. The molecules travels along the excited PES gaining kinetic energy delivered by the additional electron. Finally, the electron is back-transferred to the Fermi level of the metal and the molecule returns to the ground state, with sufficient energy to overcome the activation barrier for dissociation process.

Either when driven by temperature or by excited electrons, the final state of the adsorbed molecules involves a vibrational excitation, such that they can overcome the dissociation energy barrier [56]. The advantage of plasmon-driven dissociation reactions over those thermally driven relies that LSPR can activate the molecules at much lower temperatures and using visible light and almost solar irradiances [9, 10].

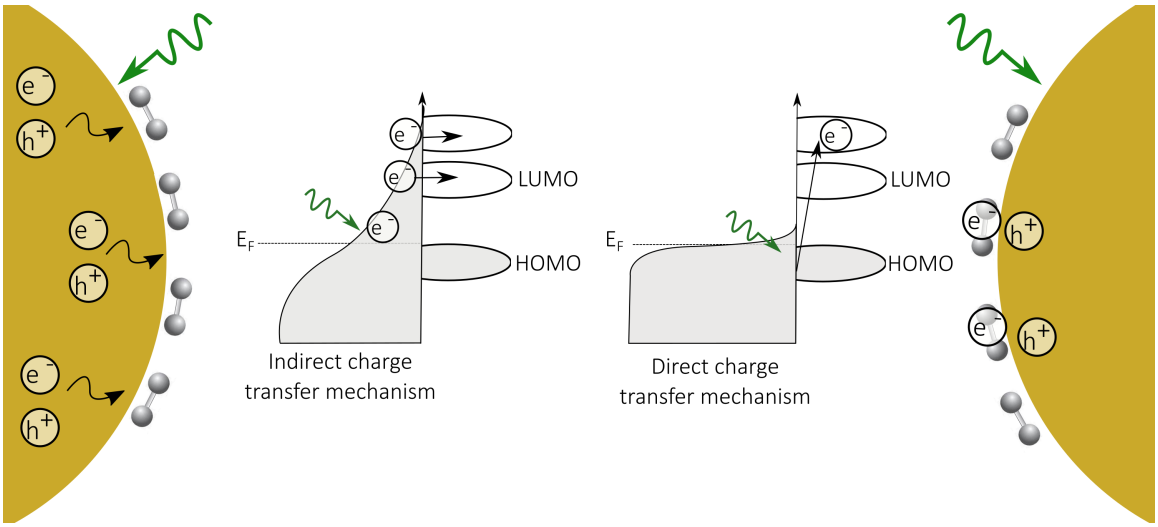

Figure 2.11: **Indirect vs. direct electron transfer.** Left: Indirect charge transfer mechanism. the energy allocated in the LSPR is distributed within the metal via electron-electron scattering, yielding a thermalized energy distribution for carriers. If holes or electrons have sufficient energy, the carrier can be transferred to the adsorbed molecule, inducing the chemical reaction. Right: Direct charge transfer mechanism. electrons (holes) are pumped to the interfacial states of the adsorbate-metal complex, while the hole (electron) remain within the metal, to be neutralized by a side reaction. Adapted from [14].

Indirect charge transfer As mentioned when describing the dynamics of LSPR decay, the scattering events of the non-thermal carriers leads to a thermalized Fermi-Dirac distribution on the electrons energy. If those carriers reach the surface and posses sufficient energy, can be pumped into the anti-bonding orbitals of the molecules, as depicted in the left side of Figure 2.11 [55]. In this illustration, the plasmonic component is a sphere like

Au NP, excited with green photons. The carriers injection rate is strongly correlated to the distance - in energy - of those anti-bonding orbital with respect of the Fermi level of the metal. Hence, the adsorbate's states closer to the Fermi level will experience larger injection rate. This mechanism do not allow for the control on the products outcome, which compromises the selectivity of the reactions. It involves an electron (hole) transfer and is complemented with a reaction that harvests the remaining hole (electron), so the initial condition can be restored.

Chemical interface damping Unlike the other mechanisms, this has been proposed for molecules that are chemisorbed to the metallic surface. The hybridization of metal-molecules orbitals opens up a new dissipation channel for the plasmon decay. Hence, the excitation of LSPR results in momentum-conserved transitions to interfacial states arising from the hybridization [55, 58, 59, 60]. Here, electron-electron scattering events inside the nanoparticles are avoided and electrons are directly pumped into unpopulated states of the adsorbate-metal interface, while the holes remain at the metal. The mechanism is illustrated on the right side of Figure 2.11. The nature of the mechanism suppose the ability to target specific states with resonant photons and thus, govern the selectivity of the reaction. This is the reason why it demands the formation of those hybrid interfacial states.

2.2.2 Local Heat

The heat contribution can be easily understood due to the exponential dependence of reaction rates with the temperature, which has been described by Arrhenius in 1884. The exponential factor in equation 2.16 includes the ratio between the *Activation barrier,* E_a and the temperature. The activation barrier is a minimum in energy that molecules must overcome to be converted into products. Hence, depending on the energy barrier, a little increase in the temperature could lead to a significant increase in the reaction rate. We know now that at last, PNPs generate local heat at their respective surface [28]. Therefore, molecules adsorbed at the PNPs' surface can experience a temperature which might differ from the bulk temperature.

$$k = Ae^{-(E_a/k_BT)} \tag{2.16}$$

At a single-particle level, the power absorbed by a PNP can be simply expressed as the product between the absorption cross section σ_{Abs}, and the irradiance and estimated by integrating the product throughout the spectral range.

$$Q = \sigma_{Abs}(\lambda) \times I(\lambda) \tag{2.17}$$

The expression above for the heat can be rewritten as follows taking into account Equation 2.12 and the fact that I=($\eta c\varepsilon_0 \ |\mathbf{E}_0|^2$) [31, 61]

$$Q = \frac{\eta^2 \omega}{2} Im(\varepsilon(\omega)) \int_{NP} |\mathbf{E}(r)|^2 \, dr \tag{2.18}$$

Thus, the heat generation is proportional to the square of the electric field inside the nanoparticle due to the fact that is only generated via light absorption in the nanoparticle.

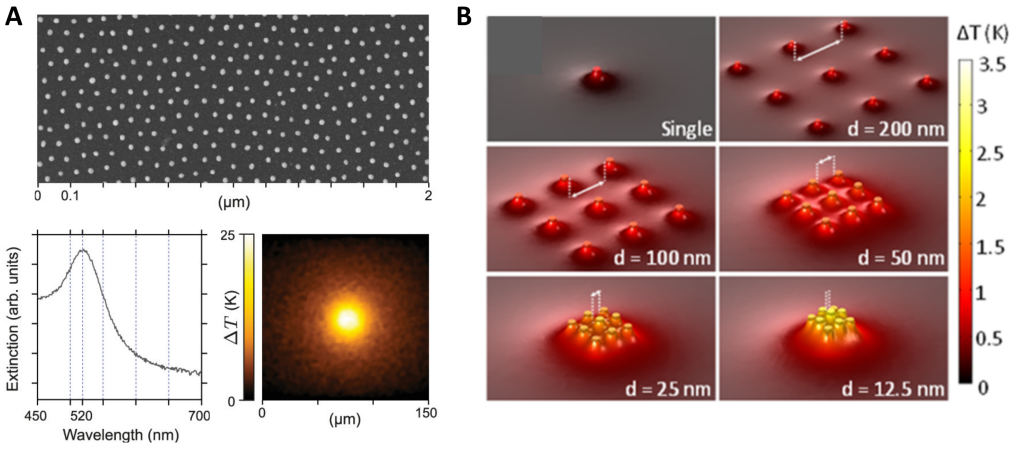

Figure 2.12: **Temperature increase in Plasmonics.(A)** 2D hexagonal proving true the collective heating effect in spite of optical decoupling. **(B)** Calculation showing that even if the particles are close in space and the same power is delivered to them, collective effects are present and can mislead to thermal contributions in plasmon-driven catalysis. **(A)** adapted from [30], **(B)** adapted from [62].

An interesting situation occurs when particles are close enough in space. At distances shorter than $\sim$ 100 nm) the nanoparticle no longer behave individually and instead start being thermally coupled, even though they remain optically decoupled [30]. This is an important aspect to be taken into account, since could lead to a potential underestimation of the temperature contribution in reaction rates. As an example, Figure 2.12A shows the temperature increase for a 2D hexagonal array of Au nanoparticles in a regime that are far away to optically interact among each others. The additional contribution to the temperature rise due to the collective heating effect can lead to a difference of at least 10°C with single-particle measurements. Additionally, an example in which the same power is delivered to arrays with different distances between the resonators is seen. In this case the particles move from a regime at which are well separated to a regime at which they start being optically coupled [62]. Similar collective effects are seen in this example at which the arrays clearly improve the conversion of light into heat. Therefore, the proper assessment of the temperature that an adsorbate would experience at the surface of a PNPs is extremely important in this field, since the combination of collective effects and the exponential dependence of the reaction rates could lead to misinterpretations [63, 64, 65, 66].

2.3 Bimetallic Nanocatalysts

Numerous examples have demonstrated that there is a boost in the reaction rates through the excitation of LSPR in plasmonic nanoantennas. Nevertheless, the losses of plasmonic materials hinder the full exploitation of such materials for sustainable technologies. Several strategies were approached to take advantage of their unique optical properties despite of the losses. Most of them are based on the incorporation of PNPs into multi-component systems (e.g. in combination with semiconductors, 2D materials, perovskites, transition metals, among others), at which the plasmonic constituent serves either as an antenna, focusing the light, an energetic carriers provider or local heater, while the second component acts as a reactive center. This enabled to use the losses more efficiently [67,68]. These concepts are properly illustrated in Figure 2.13, where the plasmonic component is represented by a Au nanorod, while the top and bottom panels show the secondary materials and the benefits of such combination, respectively. Among the profit are improved charge extraction, augmented solar absorption in the second material, stability and improved selectivity towards in reaction products.

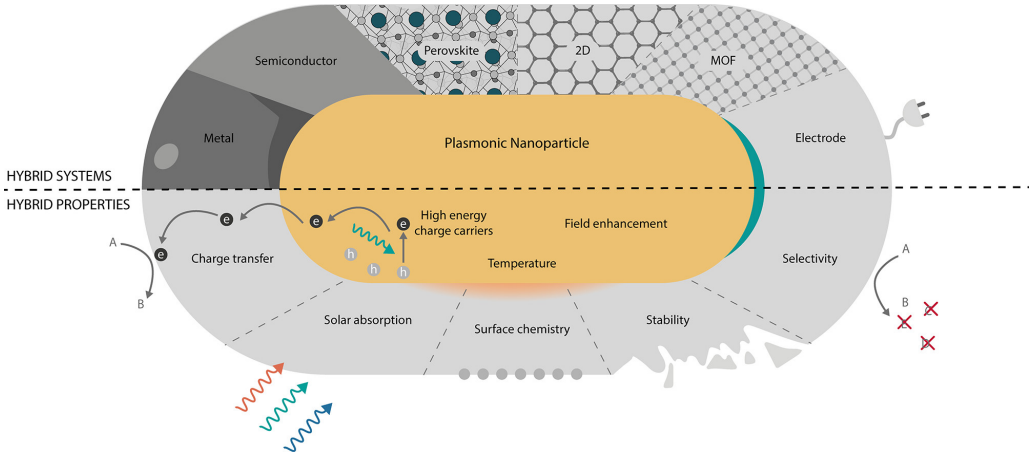

Figure 2.13: **Hybrid plasmonic nanomaterials.** The combination of PNPs with secondary materials, such as metals, semiconductors, perovskites, among others, leads to a boost in several aspects as charge carrier extraction, chemical reaction's selectivity or enhanced solar absorption. Adapted from [69].

In the framework of this thesis, PNPs were mainly combined with transition metals (Pt, Pd, Ru, Rh, etc.) to accomplish bimetallics structure that gather the principles of heterogeneous catalysis with the ones of plasmonics. Transition metals owe their outstanding reactivity to the allocation of the Fermi level on d-bands, as it will be explained later. In this section we will briefly explain the ultimate findings reported for such structures, which will help the reader to put into context our results and contributions to the field.

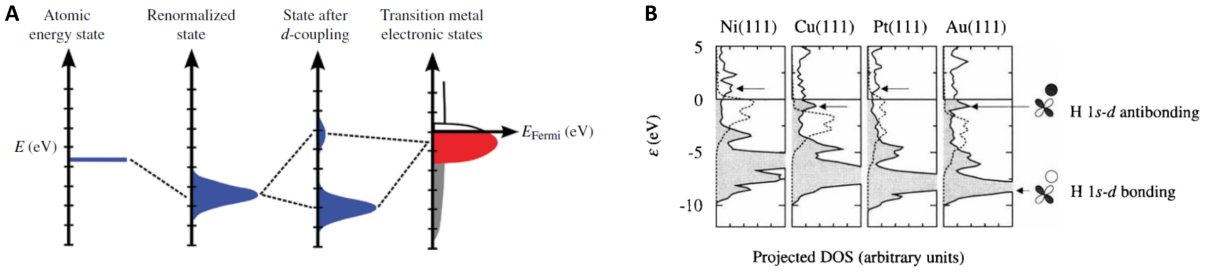

Figure 2.14: **d-band theory for transition metals. (A)** Hybridization theory at the metal-molecule interface. The position of the Fermi level with respect to the hibridization between the *d*-band of metals and molecular orbitals is what determines the affinity of the molecule for the surface. **(B)** Theory predicting the binding of H atoms to (111) metallic surfaces of Ni, Cu, Pt and Au. The theory predicts correctly the inertness of Au since it populates the anti-bonding state as well as the boding. The solid line points out the Fermi Level of the metals, while the arrow indicate the antibonding states at the metal-hydrogen interface. The shady curves are the d-band projected states of the metal. **(A)** adapted from [70], **(B)** adapted from [71].

The main motivation in complementing the so-called d-band metals with plasmonic materials relies on their cooperative functionalities. While we vastly described the benefits of plasmonic metals in terms of light-matter interaction, they present very low affinity towards molecules adsorption. Indeed, Au is acknowledged as the most noble metal and we will briefly explain the reason why [71]. The inertness of plasmonic metals implies a big limitation towards their application for catalytic purposes. Conversely, transition metals provide the remarkable capability to bind molecules in their respective surfaces and trigger the reorganization of atoms deriving in reaction products.

A theoretical description on the ability of metals to chemisorb molecules was provided by Norskov and co-workers [72]. In their model, they proposed that as the molecules approach to the surface, the molecular orbitals start interacting with the orbitals of the atoms at the very outermost layer of the metal. A classic scheme of their approach is presented in Figure 2.14A. Metals have two type of orbitals, the *sp*- and the *d*-bands. While the former is formed by the overlap of *s* and *p* atomic orbitals of the metals, resulting in a very broad band, the *d*-bands are typically more localized and narrow. Due to their inherent delocalization, the *sp*-band interact stronger with the molecules in comparison with the *d*-bands. When the molecules couple to the *sp*-band, bonding states are created, process denominated renormalization of the orbitals. Most common scenario across all metals is that the bonding orbitals lies deep down in energy and are completely populated. In a second step, the renormalized orbitals couple to the *d*-band, forming bonding and anti-bonding states below and above of the renormalized orbitals, respectively. Under the assumption that all transition metals interact similarly with approaching molecules through the broad *sp*-band ($\Delta E_{sp-band} < 0, \approx constant$ in Equation 2.19), the ability of the metals to form bind molecules strongly depends on the relative position between the Fermi level and the new anti-bonding orbital formed upon coupling with the *d*-band (ΔE_{d-band}). An example of the binding of H atoms on metallic surfaces is provided in Figure 2.14B, which

exemplifies the concept mentioned in this paragraph.

$$\Delta E_{Adsorption} = \Delta E_{sp-band} + \Delta E_{d-band} \tag{2.19}$$

It is known that for metals such as Au or Ag, commonly used as plasmonics metals, the Fermi level falls into a *s*-band, accompanied by deep-lying *d*-band. Therefore, both bonding and anti-bonding states are formed below the energy of the Fermi level, which in combination with the large availability of electrons in the metal, end up being completely populated. Hence, the fast desorption of molecules is promoted (Figure 2.15A). However, the scenario is different for metals such as Pt, Pd, etc. Their Fermi level is intersected by a *d*-band and the anti-bonding orbitals are generally above the Fermi level, enabling to only populate them partially (Figure 2.15B). Consequently, the adsorbates remain bound to the surface. However, a very strong adsorption can be counterproductive. In this regard, the surfaces should be prone to bind molecules, but the strength should not be excessive, as otherwise a large input of energy would be required to desorb products. It means, the active sites offered for an active surface for a chemical reaction to happen are passivated by the molecule. The concept is often referred to as "poisoning" the surface.

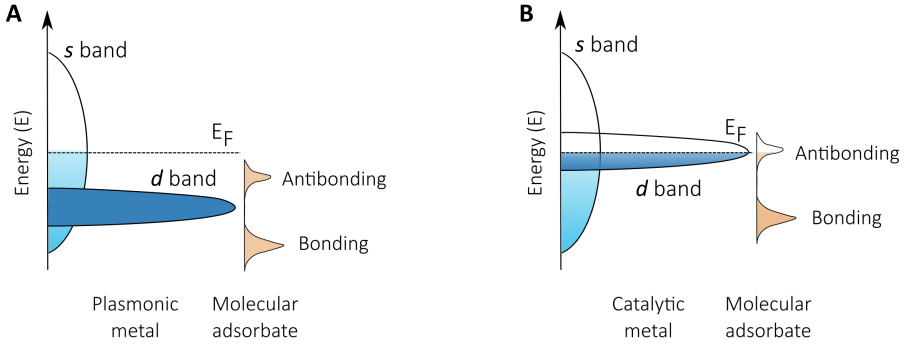

Figure 2.15: **Comparison of the affinity of plasmonic and catalytic metals for molecules. (A)** Due to the deep-lying d-band of plasmonic metals, the anti-bonding molecules are populated since the Fermi level falls into a *s*-band promoting the poor adsorptive properties of plasmonic metals. Irrespective of the excitation of carriers, they do not strongly bind molecules. **(B)** Unlike plasmonic metals, the Fermi level is intercepted by a *d*-band and the anti-bonding is poorly populated, what accounts for the good affinity presented by catalytic metals. Then upon carrier excitation, they can trigger a chemical reaction in the adsorbed molecules. Adapted from [14].

The intuitive combination of those materials was proven to be fruitful in terms of production, since there are many examples reported in which hybrid structure outperforms the individual constituents [73,74,75,76]. Interestingly, several ways to combine both materials were reported and the opto-catalytic properties strongly correlate to the structural properties the all-in-one structure, which determine how the constituents interact [77]. Below we will provide a brief discussion on the different phenomena arising upon combination, intending to remark on their inherent differences.

2.3.1 Core@Shell structures

The term of *Core@Shell* structures intuitively leads to visualize a composition at which one material is encapsulated into the other. This is typically the case, although here we will also include those at which the second material partially coat the first one. Schemes of these type of structures are provided in Figures 2.16A,B. Generally, in this configuration the plasmonic metals act as a core, whilst the catalytic one is the outermost layer, such that the surface can be exposed to conduct chemical reactions. From now on the notation core@shell will denote for a plasmonic@catalytic nanostructure. The accomplishment of core@shell structures in a wet chemistry approach involves an initial step at which first the core is fabricated, acting as a template for the deposition of the catalytic metal. By controlling the amount of precursor, the outcome can be a fully or partially coated structure.

The inclusion of a catalytic metal into the structure has a strong influence on the optical properties, altering them dramatically. The spatial absorption profile of a bare Ag nanocube (edgl length$\sim$ 70 nm) versus the same cube coated with an homogeneous Pt shell of 1 nm thick (Ag@Pt) are presented in Figure 2.16C. The sole inclusion of such a tiny amount of Pt reversed the relative absorption in the components. While for bare Ag nanocubes the core was the main absorber, a large fraction of light was absorbed by the 1 nm of Pt shell in the bimetallic nanostructure, exciting *d-to-s* transitions in Pt. This was also confirmed by mapping the dissipation power, which was shown to occur through the Pt thin layer. This findings pointed out the fact that upon hybridization, energy can be funnelled towards the catalytic center.

Nevertheless, to complete the story, besides the spatial absorption profile, it is important to know how much of the incident light is intercepted and finally absorbed by the structure. Typically, late transiton metals introduce damping to the system, worsening the quality of the antenna (lower Q-factor). This concept is depicted in Figure 2.16D in which the extinction cross-section of a Au nanorod core and a Pd shell of $\sim$ 2 nm was compared versus the additive cross-section of each of them separately [77]. It can clearly be seen from the example that when the two components were interfaced, the resonance was blue-shifted and notably damped and broadened. The damping and the broadening are typical features for increasing damping on resonators, a clear threat for plasmonic properties. Experimental signatures of this behaviour recently investigated by comparing the scattering of bare Au nanorods and tip-coated Au@Pd nanorods at the single particle level [78]. Figure 2.16E shows the normalized scattering spectra of both Au and Au@Pd rods, indicating the clear broadening for the bimetallic system. The reason of the broadening of the bandwidth was assigned to an additional dissipative energy channel involving charge transfer from the core to the Pd phase. Finally, time-resolved dynamics were conducted in Au@Pt spherical nanoparticles, which confirmed the acceleration of the excited carriers kinetics by the presence of a Pt shell when compared to the initial Au nanoparticle (Figure 2.16F) [79]. The faster dissipation was confirmed to take place due to the injection of hot carriers into the Pt shell after being generated in the Au core, as indicated in Figure 2.16G. To be noted, partially coated core@shell nanostructures generally present a lesser dampening of the LSPR [73, 79].

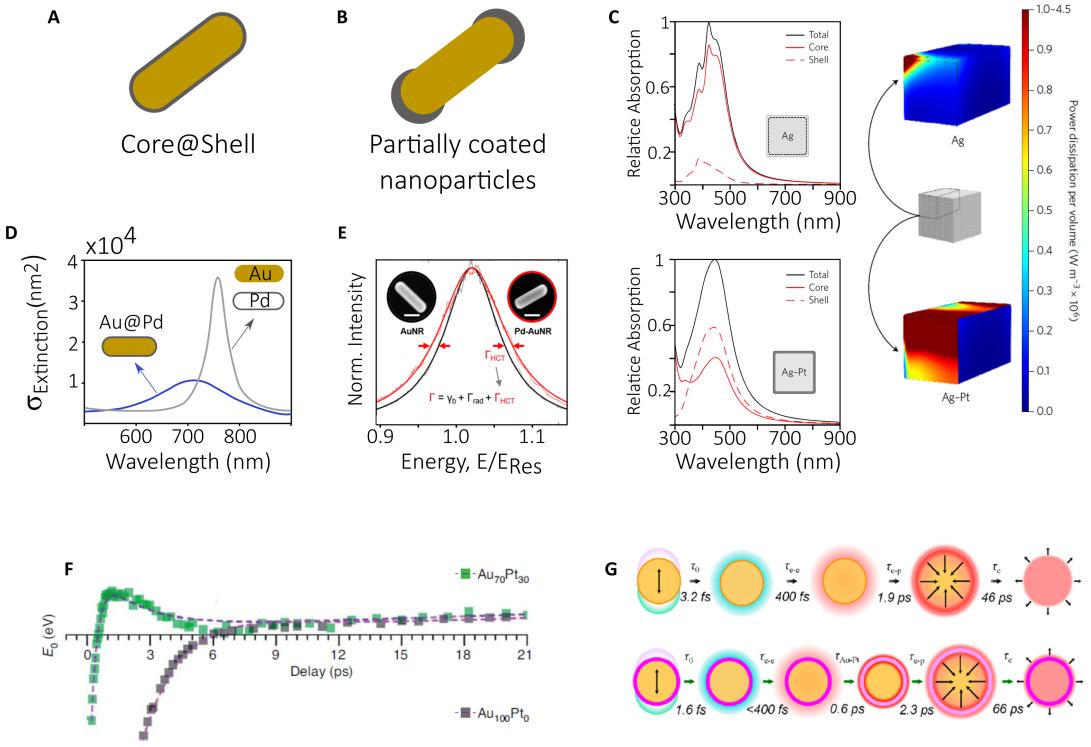

Figure 2.16: **Core@Shell bimetallic structures.** **(A,B)** Illustration of fully coated and partially coated nanoparticles, both referred to as core@shell configurations in this thesis. **(C)** Altered spatially resolved relative absorption. The core absorbs the most for a monometallic Ag nanocube of $\sim$ 70 nm, while the shell conducts the largest absorption fraction when 1 nm Pt shell is introduced in the system. The power dissipation analysis shows that the energy is released throughout the entire surface for the bimetallic nanocube. **(D)** Comparison of σ_{Ext} of a Au@Pd nanorod versus the additive cross section of the constituents separately. This shows the significant damping that takes places when the materials are interfaced. **(E)** Signature of the damping was also observed when tracking the scattering a the single-particle level. The broadening of the signal was attributed to plasmonic-to-catalytic metal charge transfer. **(F,G)** Studies on the dynamics of a monometallic Au NP and Au@Pt core@shell confirmed the faster dissipation of excited carriers due to the presence of a catalytic metal. The reason was confirmed to be a transfer of carriers to the Pt shell, where they lose their energy faster. **(C)** adapted from [80], **(D)** adapted from [77], **(E)** adapted from [78], **(F,G)** adapted from [79].

All in all, the vast study of *core@shell* structures confirmed that in spite of the dampening of the plasmonic resonance, their photocatalytic activity is boosted in comparison with either constituents separately. The reason why is because energy can be funneled to the catalytic metals either by boosting its absorption or by supplying excited carriers from the plasmonic component. In this regard, partially coated hybrid bimetallic catalysts seem to be more convenient since these the LSPR is slightly damped and the benefits of the interface can be exploited towards hot carrier transfer. Due to the lossy nature of late transition metals (large Im $[\varepsilon(\omega)]$), the thickness of the coating should not exceed the mean free path as otherwise the electrons would scatter, losing energy and being unable to reach the metal-molecule interface. Last, other effects take place when a metal with

certain lattice parameter is deposited onto another with different spatial dimensions [81]. This is known as "strain" effect the solid shrinks or "tensile strain" if the solid elongates. Changes in the lattice constant impact on electronic properties and thus, reactivity, as we will discuss for alloys in subsection 2.3.3.

2.3.2 Antenna-reactor structures

A second way to arrange the constituents into a single structure is the *Antenna-Reactor* geometry (sketch in Figure 2.17A), also often referred to as *Core-Satellites*. The concept was originated due to the ability to locate catalytic nanoparticles in the near-environment of PNPs.

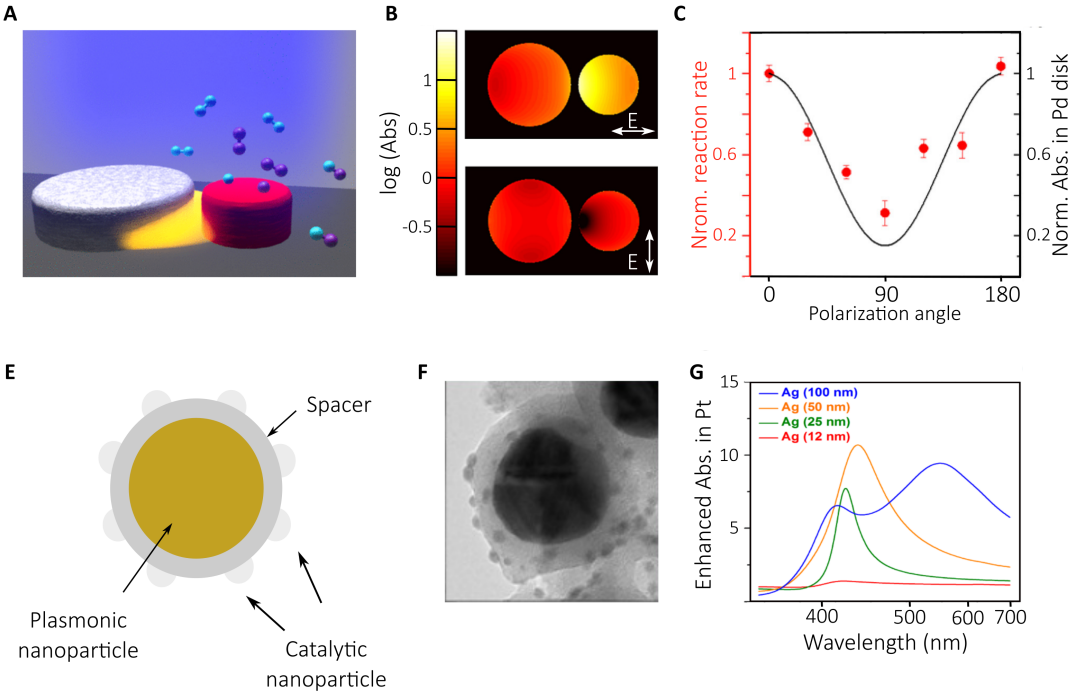

Figure 2.17: **Antenna-Reactor (A)** Illustration of an antenna-reactor system comprised of an Al disk (antenna) and a Pd disk (reactor). **(B)** Absorption profile of antenna-reactor in (A) illuminated on resonance with parallel and perpendicular polarizations with respect to the axis of the system. More energy is absorbed by the reactor when the incident light is polarized parellel to the system. **(C)** Reactivity of the antenna reactor with respect of the angle between the polarized light and the bimetallic complex. The larger activity is seen when more energy is funnelled to the Pd disk **(D)** Illustration of a colloidal antenna-reactor system. The interface between the material is avoided by using a spacer. **(E)** TEM image of a Au-Pt antenna reactor in which a 10 nm SiO_2 spacer is used. Many particles are used and activated when using unpolarized light. **(F)** The absorption enhancement follows the resonance of the antenna, as demonstrated for Ag antennas within a range of sizes spanning from 10 to 100 nm. **(A,B,C)** adapted from [82], **(F,G)** adapted from [83].

In general, the physical contact between the two is avoided to preserve the optical

properties provided by the plasmonic component. The catalytic center is normally placed at distances larger than 1 nm, to avoid quantum effects, and smaller than 10 nm to power the active metal. Similar to what occurs in dimers, the formation of an interparticle gap leads to a confinement of the electric field in that region.

Antenna-reactor pairs can be fabricated either via top-down or bottom-up methods. The synergy of the constituents in this configuration was first proven using a sample prepared via top-down methods. Figure 2.17A shows illustrates an example at which an Al disk represented the plasmonic constituent, while a small Pd disk was employed as an active center [82]. An interesting phenomena was observed due to the asymmetry of the binary system. Similarly to what occurs in dimers, the electric field is greatly enhanced at the interparticle gap when the polarized light along the axis of the antenna-reactor complex is used. As a result, a larger absorption can be induced in the catalitic active center, as it is shown in Figure 2.17B when both polarizations are used to illuminate the structure. This stronger absorption has an impact on the reactivity of the catalytic center as revealed when varying the angle between the antenna-reactor and the linearly polarized light (Figure 2.17C).

The concept was further extended and similarly, this structure was also realized with a colloidal approach [83]. To maintain the material separated the strategy involved the coating of pre-fabricated cores with a thin isolating shell (e.g. SiO_2), followed by the reduction of precursor on the isolating shell (Figure 2.17D). The advantage of this approach was to locate many more active centers around the main core, so when unpolarized light is utilized, all of them can be simultaneously activated. A boosted absorption in catalytic particles was still observed, correlated with a higher activity. The energy funneled to the catalytic material has been determined to follow the resonant behaviour of plasmonic components (2.17F), as expected.

2.3.3 Alloys

The last way to combine two metals that will be discussed in this thesis are the *Alloys*. The advantage of these type of bimetallic structures, in comparison with the already mentioned, is the capability to tailor the composition of each metal and fabricate what can be considered as different materials in both, optical and catalytic regards. Figure 2.18A shows an example of how the *d*-band of an alloy changes with composition [84].

The composition of the alloy plays an important role, since the optoelectronic properties are strongly dependent of it. For instance, the dielectric function of an alloy can not be simply calculated in a linear way ($\varepsilon_{Alloy} \neq X\varepsilon_{Plasmonic} + Y\varepsilon_{Catalytic}$, X and Y representing the fractions) [85]. Still, likewise the core@shell structures, the inclusion of catalytic metals can also be interpreted as an increase in the the dampening due to the increase in the overall imaginary part of $\varepsilon_{Alloy}(\omega)$.

Moreover, alloy-induced tensile and strain effects occur with the presence of a second metal as a result of the elongation or shrinking of interatomic distance. Due to the lager (lesser) overlap of the atomic orbitals, the *d*-band is narrowed (widened), and the Fermi level upshifted (downshifted). As the occupancy of the antibonding orbitals of adsorbed

molecules strongly depends to its relative position with respect to the Fermi Level, the affinity of the molecule to the surface can be either boosted or worsened [86]. The tunability of such parameter is a feature that is not presented in other configurations.

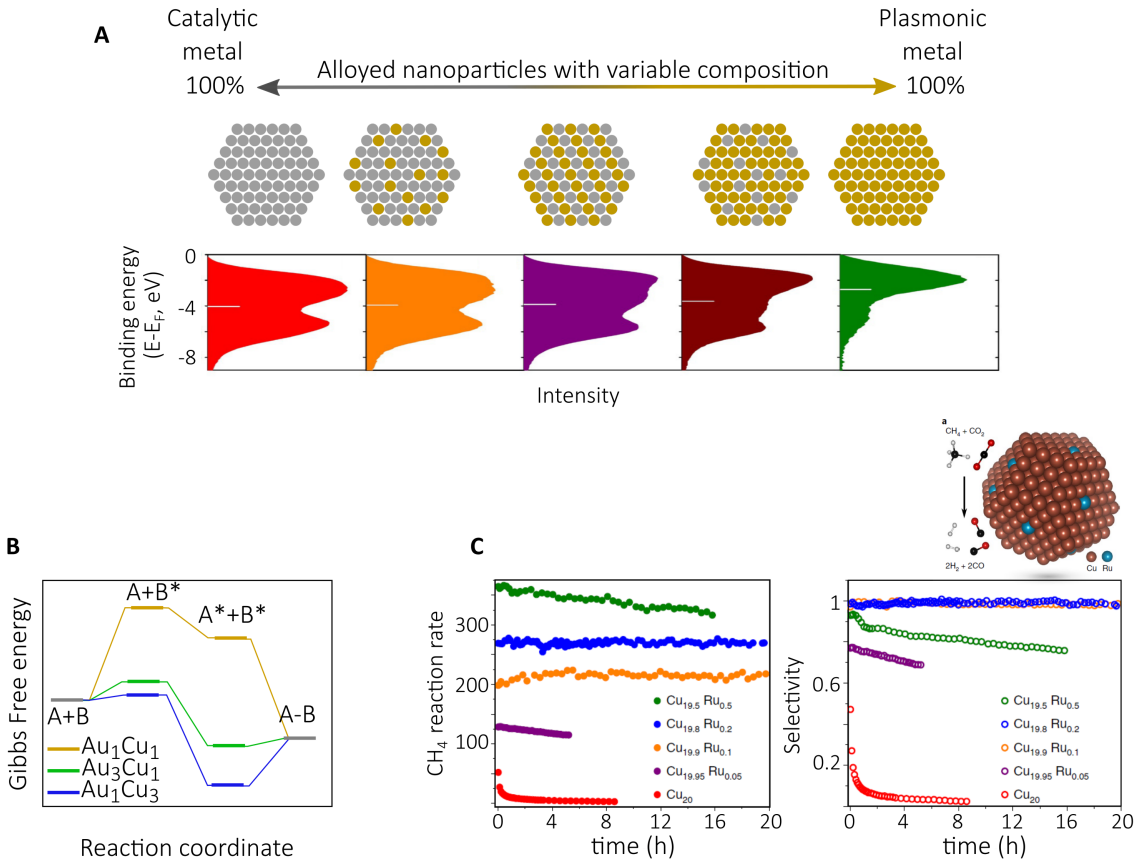

Figure 2.18: **Alloyed nanostructures (A)** Set of alloyed nanoparticles with varying composition. The electronic properties of the alloyed nanoparticles strongly depend on the composition. **(B)** Changes in intermediate activation barrier as a function of the composition of the alloy. It is possible to induce a faster desorption or change the selectivity of the reaction by tuning the composition of the alloys. **(C)** Single atom catalysis in Cu-Ru nanostructures. The ultra-low quantities of Ru enabled to reach a still high reaction rate and a selectivitx of 100%, which lasted for at least 20 h. **(A)** adapted from [84], **(C)** adapted from [87].

One of the main benefits in alloying two metals is the ability to the modulate the activation barriers of processes involving the formation of reaction intermediates, as depicted in Figure 2.18B. This is particularly interesting for the rate limiting step (RLS) of a chemical reaction. It is known that a reaction assisted by a surfaces is not a process in which atoms immediately re-organize to form the products. Instead, the scission and formation of bonds typically take place in different elemental steps of the reaction pathway. As each of these elemental steps possess different energy barriers, the one with the largest is the one that slows down the overall reaction rate. The acceleration of the RLS by targeting

an alloy with certain composition in which the materials cooperate positively is a strategy to circumventing this aspect of chemical reactions. Additionally, this suppose the ability to tilt the selectivity in reactions with more than a pathway, a very important field of heterogeneous catalysis. This is a very promising of alloys since specific products can be targeted. None of the above mentioned structures have the ability to modify the reaction pathway of chemical reactions, what allows to postulate that alloys will become key players in plasmon-driven catalysis.

Recently, alloys with a very low amount of catalytic metals have been extensively studied [88]. This sub-field is known as single-atom catalysis. Moving towards single atom catalysis is even more promising since the inclusion of catalytic metals at the atomic scale suppose very little damping in comparison with more concentrated samples or even core@shell structures, hence keeping the optical properties unaffected, and also decreasing the overall price of those catalysts, a transition metals are often expensive. An example in which Cu-Ru photocatalysts with different compositions (all of them diluted) were tested towards methane reforming, and interestingly, when reaching the single atom regime, the bimetallic catalyst still showed a high activity, and more important, showed a selectivity towards dehydrogenation pathway of 100% sustained at least for 20 h (2.18C) [87].

In spite of the advantages mentioned in the prior paragraph, the alloys systems face some limitations. For example, once fabricated, the metals can diffuse or undergo phase separaton, ending with a gradient of optoelectronic properties and very localized associated effects [89]. Additionally, from the synthesis point of view, it is still hard to design nanocrystals with define shape in which the alloy composition extends constantly throughout the crystal.

2.4 Theoretical background on nanoparticles fabrication

The above mentioned configurations for plasmonic bimetallic photocatalysts will be synthesized via using wet chemistry to conduct photocatalytic and photothermal analyses and it is necessary to understand the principles behind their preparation.

2.4.1 Homogeneous Nucleation Theory

The fabrication of nanoparticles can be approached either employing top-down or bottom-up methods. The former refers to the break-down of a bulk material into smaller fragments down to the nanorange (e.g. ball milling), while the latter involves the creation of nanostructures starting from smaller precursors (e.g. reduction of ions in solution). Across this thesis, all nanostructures employed in the studies were fabricated with bottom-up approaches. Hence, it is worth to shortly describe the fundamentals of the process.

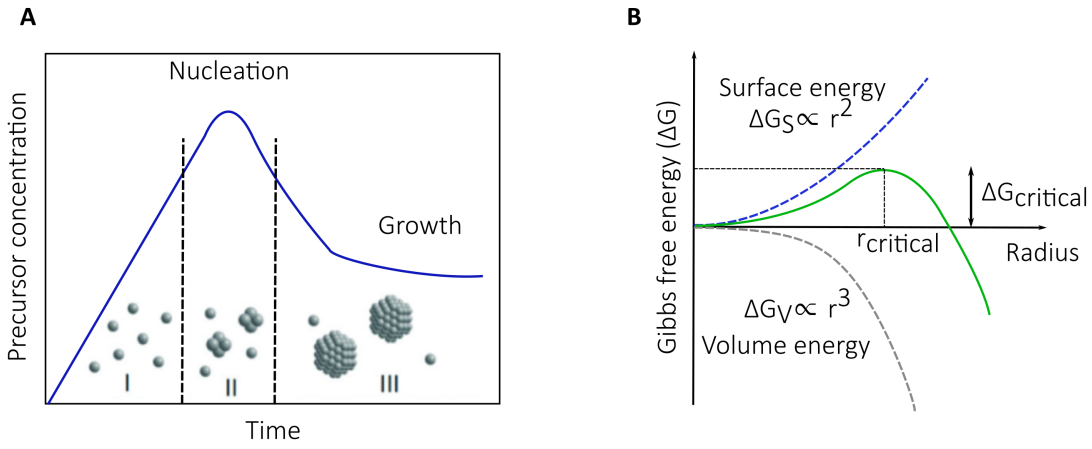

Figure 2.19: **Growth of nanocrystals (A)** Lamer's model dividing homogeneous (phases I and II) and heterogeneous processes in crytal's growth in solution. Once the cluster surpassed the required energy for their formation, the addition of monomers deposit upon the clusters, initiating the growth. **(B)** Gibbs free energy diagram for the formation of metallic clusters in solution. The surface energy dominates for small sizes, while the volume energy does for larger sizes. The critical radius ($r_{critical}$) is the minimum size that the cluster most overcome to be favored thermodynamically and avoid its segregation. **(A,B)** adapted from [90].

The fabrication of metallic nanoparticles in solution from the reduction of ions suppose the formation of a new crystalline phase. According to Lamer's model, we can separate the process in three phases, as illustrated in Figure 2.19A. The first in which upon reduction agent addition, the concentration of atoms with zero valence start to be generated, incrementing their concentration until they reach a critical level (supersaturation), in which the situation collapse to the aggregation of individual atoms to form the initial clusters. This burst-nucleation is acknowledged as the phase 2 and is assumed to be occur at an infinite speed. The last phase of the process is the growth, in which the concentration of monomers diminished and they start depositing onto the previously formed clusters to reach the targeted size. While phase I and II are considered within homogeneous nucleation, phase III belongs to heterogeneous nucleation.

We can borrow a few concepts developed in Homogeneous Nucleation Theory to gain insight in how the formation of nuclei occurs [90, 91]. The change in Gibbs free energy evaluates the energy difference between the cluster (final) and the ions in solution (initial) and has the form of:

$$\Delta G = -\frac{4\pi k_B T}{3V_m} r^3 \ln S + 4\pi\gamma r^2 \tag{2.20}$$

Where k_B is the Boltzmann constant, T the temperature, V_m is the molar volume of the material, γ is the surface tension and S represents the supersaturation of the solution. Due to the opposing signs of the volume and surface contributions and their dependence on the radius we can expect that the surface term is larger for smaller radius, while the volume contribution prevail for larger ones. Therefore, by differentiating with respect to

the radius (*critical radius*) we can find a condition at which the formation starts to be favoured thermodynamically.

$$\frac{d\Delta G}{dr} = 0 \quad \rightarrow \quad r_{crit} = \frac{2\gamma V_m}{k_B T \ln S} \tag{2.21}$$

Equation 2.21 provides a reference value which the clusters must overcome to endure the formation process. Otherwise, due to the large instability, they break re-dissolving into the solution (Figure 2.19B).

By evaluating the Gibbs free energy at the critical radius (ΔG (r=$r_{critical}$)), we can now estimate a nucleation rate by assuming an Arrhenius process.

$$\Delta G_{Critical} = 4\pi\gamma r^2_{critical} \quad \rightarrow \quad \frac{dN}{dt} = A \exp\left(\frac{-\Delta G_{Critical}}{k_B T}\right) \tag{2.22}$$

One important aspect of the synthesis, that should not be overlooked, is the role of the surfactants. The stability of the colloidal suspensions is threatened by the attractive nature of van der Waals forces, as dictated by the always positive effective Hamacker constant for interactions between identical bodies. It means, that even though the nanoparticles can be fabricated, they will end up pulling each other to form a macrocluster from the individual particles. This processes is known as coalescence. Particularly in plasmonics, this is very important as the closeness of particles could lead to dramatic changes in the optical-, thermo- and catalytic properties of the particles. To avoid the coalescence, nanoparticles are coated with ligands who provide the stability for the particles to remain separated.

Water is the most common solvent employed for nanoparticles synthesis. Therefore, to overcome the attractive forces, the ligands normally present a formal charge, thus repealing each other by means of coulombic forces. Examples of ligands are quaternary amines (NR_4^+) or molecules with carboxylic groups (-COO^-). The presence of formal charges at the surface of the nanoparticle leads to a re-organization of water and dissolved ions take place around the nanoparticle. The most common way to picture this process is presented in Figure 2.20. The negatively charged surface binds positively charged ions forming a compact atomic layer (*Stern layer*). This is followed by a second layer comprised of counter-ions and more cations although with a larger freedom in comparison with the first one. The boundary of the second layer is often referred to as *Slipping plane*, from which the diffuse layer starts, where atoms has a random distribution as in the bulk. The electric potential at the slipping plane has received the name of ζ-potential (units in millivolts, mV) and serves as a metric for the stability of the particle. The parameter can be determined experimentally and it is often observed that if $0 < \zeta < 20$ mV the stability of the colloids is incipient, while for ζ >30 mV the stability is moderate and the solutions have been proved to last even months.

Understanding the surface chemistry is not only important to extend the lifetime of the particles. Dominating the surface chemistry of colloids provides the opportunity of manipulate the nanoparticles in a way that serve as building blocks for more complex structures [92, 93, 94] . In this regard, external agents such as pH, temperature, gas pressure,

ionic strength, magnetic fields and so on can act as stimuli to induce the controlled aggregation to reach macrocompounds [95]. Specially in the field of plasmonics, the controlled aggregation is a key player for the design of new structures with unprecedented optical response, which differ by far from the optical behaviour of individual constituents [96].

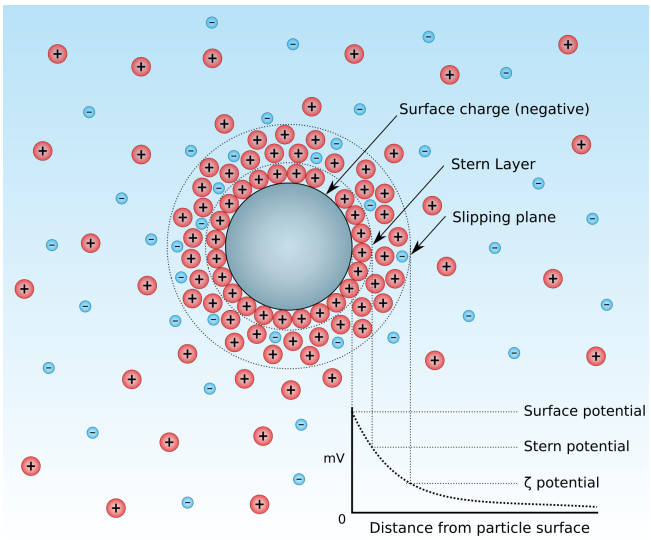

Figure 2.20: **Stern Model for spheres with charged interfaces** Sketch illustrating the spatial distribution of ions in the presence of charged nanoparticles. The Stern layer is an atomic layer of positive ions on negatively charged interfaces, followed by a second layer of with both anions and cations, denominated slipping layer. From that layer on, the ions has a random location due to the screening of the first layers (diffuse layer). The ζ-potential, accounting for the stability of the NPs, is the electric potential at the slipping layer. Image extracted from [97]

Chapter 3

Materials and Methods

This chapter is dedicated to provide a brief description of the chosen techniques that enabled to interpret experimental results and thus, build little by little the findings comprising this thesis. The chapter starts describing the methodology employed to fabricate metallic nanocrystals with specific sizes, and continues providing a detailed explanation on the manipulation of their surface chemistry to assembly individual nanostructures into more complex structures. Last, the reader will find homemade setups for photocatalytic experiments, as well as customized facilities which allowed to study the systems in depth.

3.1 Synthesis of Metal-based NPs

The art of fabricating nanomaterials has been extensively developed in the last 20-to-30 years, and nowadays one can find a vast amount of metals and semiconductors that were shaped in unaccountable forms. However, the presence of such nanostructures dates from very ancient times (Lycurgus cup, 4 d.c.), in which the still unknown Au-based nanoparticles were incorporated in glass to provide fascinating color to glassware. In 1857, the experimentalist Michael Faraday was who correlated the AuNPs with the optical properties observed macroscopically [98]. In this thesis, the synthesis of nanoparticles via wet chemistry was the main method for sample fabrication and the motivation relies in its faster and massive production with respect to top-down methodologies.

The colloidal approach to nanoparticles synthesis always involves the presence of a salt containing the metal in oxidized chemical states (M^{+n}). In order to bring them to zero valence, an entity providing the necessary electrons is required, acknowledged as *reducing agent*. Typical reduction agents are trisodium citrate (Na_3Cit), Sodium Borohydride ($NaBH_4$), Ascorbic acid (AA), Oleylamine, among others. Not all of them possess the same power and are similarly activated, in terms of reactivity, when used at the same conditions and can be ranked. For instance, while $NaBH_4$ is very reactive and reduces mostly everything that faces, AA is in comparison a milder one. Others need to be activated at high temperatures, such as Na_3Cit and Oleylamine, to be able to perform as reducing agents.

The third essential component of the synthesis, as important as the past two, are the

ligands. Their absence does not mean that nanoparticles can not be formed. Instead, their importance relies on the ability to stabilize the formed nanoparticles, since otherwise, the attractive VdW forces would pull them together, leading to uncontrolled aggregation. The nature of the ligand is strongly correlated to the solvent in which the synthesis takes place. The most common medium is H_2O, therefore, the ligands present charged group or polar groups to favor the repulsion between the individual nanoparticles. However, similar concept can be applied in organic media, just benefiting from unpolar molecules to keep them separated. It is important to give the surface chemistry the attention it deserves, specially for plasmonic materials, since it the stability could be easily compromised by changes in pH, temperature, ionic strength, polarity of the solvent, etc., strongly affecting their optical behaviour. Interestingly, some molecules (Na_3Cit or Oleylamine) can play a dual role since they not only reduce the salt, but also stabilize the nanoparticle. Finally, the interaction between the ligands and the surfaces also matters, as sometimes they can direct the growth of the nanocrystals.

Despite of there are still many aspects of nanoparticles synthesis that remain unknown, the deep understanding gained throughout the years of experience have giving to synthetic researchers the ability to shape nanomaterials strategically, pursuing desired properties. Especially in this thesis, as we can anticipate at this point, the well-defined architecture allowed us to shed light on the interaction of plasmonic and catalytic metals and pave the way in their structural-perfomance correlation for photocatalytic purposes. Below, we provide details about the synthesis and setup utilized to characterize the nanoaprticles, as well as to test their photocatalytic activity.

3.1.1 Au nanospheres (AuNS)

Au nanospheres (AuNS) were fabricated following the report from Zheng et al. [99], slightly modified to achieve larger volumes. The synthetic route allows the tunability of the particles from basically 5 to 150 nm. Figure 3.1 presents a sketch of the synthesis.

A general sketch of the procedure is presented in Figure 3.1. As observed. the Au precursor is reduced to Au^0 atoms by $NaBH_4$, a very strong reducing agent, in the presence of Cetyl Trimethyl Ammonium bromide (CTAB). The atoms start clustering (< 1 nm in size), as evidenced by the brownish color in the solution. These clusters are normally stable for a few hours. A certain volume of the seeds is then diluted in a CTAC (C= chloride) solutions and Au precursor is added in the presence of a AA, causing the growth of cluster to form ~ 10 nm AuNS, later used as *seeds*. The size of the seeds is not fixed and can be regulated by tuning the clusters:precursor ratio. Finally, to achieve the desired size, the seeds are diluted and Au precursor is now pumped in at a controlled rate in the presence of Ascorbic Acid (AA) and CTAC. The pumping rate is a very important parameter, since the Au atoms' deposition must occur at a similar rate at which the less coordinated atoms at the nanosphere's surface diffuse away to find a less energetic configuration. This surface diffusion, promoted by the CTA molecules, enable to preserve the sphere-like shape and smooth surface [100]. It is important to know if the size difference between the seeds and the targeted one is very large, additional steps must be taken to achieve the final size. The

appealing feature of this methods over others relies on its simplicity, reproducibility -due to the use of the pump- and the possibility to tune their dimensions very accurately in a wide range of diameter. Specifically, tailoring the size enables to gain an oustanding control to tune of LSRP of nanospheres, as well as the absorption and scattering contributions.

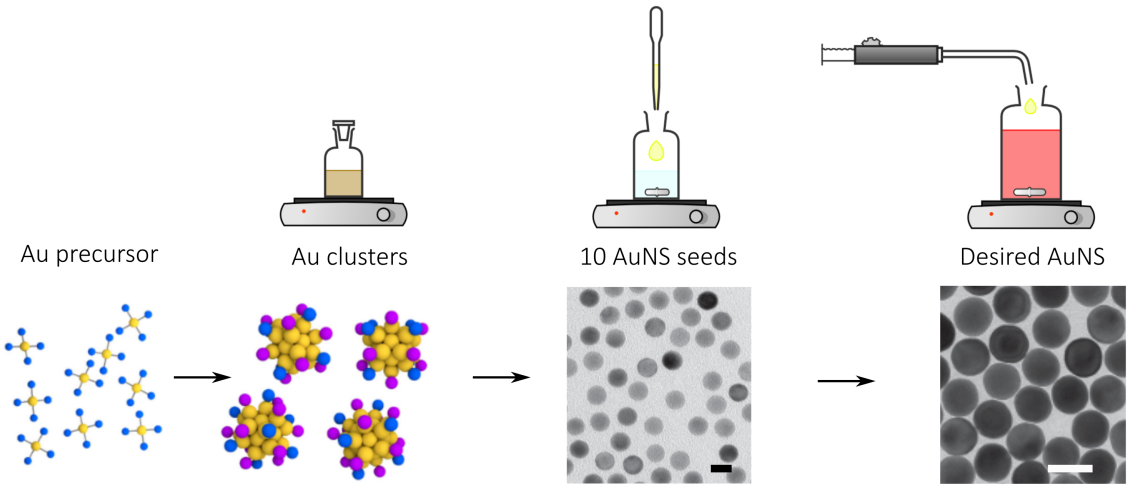

Figure 3.1: **Synthesis AuNS.**The well-established protocol starts with the reduction of Au salts to form subnanometer clusters. The clusters are then growth to achieve 10 nm AuNS, which are later used as seeds to accomplish the desired size by pumping Au precursor at low and controlled rate. The slow Au precursor addition enables the low-coordinated surface atoms to diffuse, preserving the spherical shape in the growing process. Adapted from [101].

In this thesis we synthesized AuNS with 10, 22, 60 an 67 nm, showing the versatility offered by the method. Details on the nanoparticle synthesis are provided in Appendix B. The as-synthesized AuNS served in all projects as the plasmonic component in the hybrid systems.

3.1.2 Synthesis of satellites

Palladium (Pd) and Platinum (Pt) are transition metals which has received significant attention since the creation of nanometer scale materials are a daily task. The reason behind this interest is driven by their catalytic properties, since unlike plasmonic materials, their LSPR lies deep in the UV and are very much damped. For instance, Pd serve as catalyst in Heck or Suzuki reactions, in which alkyl chains end up coupling to unsaturated alkenes (creation of C-C bond) - worth Chemistry Nobel Prize in 2010 -. Similarly, Pt catalyzes the H_2 from H^+ or facilitates the combustion of hydrocarbon. Manufacturing catalysts within nanometer range based on these active metals allows to take more advantage of their reactive surface due to the large surface-to-volume ratio of nanocatalysts.

In this thesis, we employed them as the reactive centers of our hybrid catalysts owing its use to their elevated activity towards H_2 generation from Formic Acid (nowadays used as a H_2 carrier). In the case of Pd NPs, its precursor was reduced by AA at high temperatures, in the presence of Polyvinylpyrrolidone (PVP) in solution, serving as stabilizing agent of the resulting NPs. The PVP provides the negative charge for them to be stable for years. Likewise, Pt nanoparticles were fabricated by reducing Pt precursor with $NaBH_4$, stabilized in this case by citrate molecules also present in solution. The details are presented in Appendix B.

3.1.3 Bimetallic NPs preparation

The motivation on the preparation of bimetallic NPs has been mentioned in the introduction. Since not all metals perform the same either optically or catalytically, accomplishing a bimetallic structure can in principle gather a single entity with complementary functionalities. Understanding their interaction in the final hybrid NPs is what motivated this thesis. Below a description on the synthetic routes for their fabrication.

Core@shell NPs The name given to these structures is very descriptive. Basically, this is the terminology adopted for any structure in which one material (core) is encapsulated by a second one (shell). Core@shell NPs (CS NPs) of different compositions and sizes were fabricated in this thesis and to realize them, it was necessary to develop different routes.

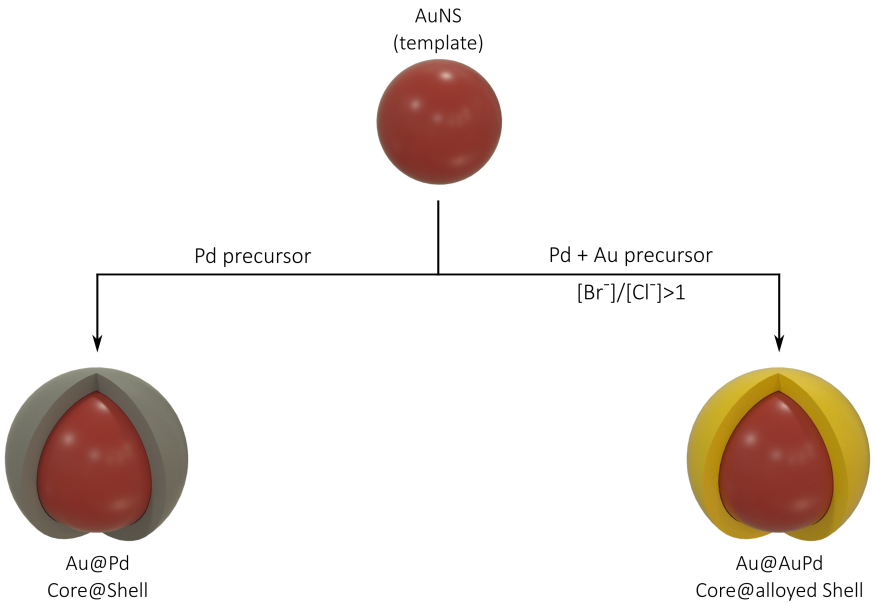

Figure 3.2: **Core@Shell NPs.**Previously fabricated AuNS serve as templates where the metallic or bimetallic shell is deposited. Unlike the monometallic (Pd in scheme) shell, to obtained a bimetallic alloyed shell, it was necessary to adjust the Br-to-Cl ratio, since its modulate the spatial distribution of the materials by controllin the precursor's reduction rate. If they differ by a lot, instead an alloyed one, two separated phases would be obtained at the shell.

For instance, to achieve Au@Pd CS NPs, we developed a seeded-mediated method in which Pd precursor was reduced onto previously fabricated AuNS (Section 3.1.1) at high temperatures. CTAB was once more the stabilizing molecule. By controlling the ratio between number of AuNS (N_{AuNS}) and the added precursor, it was possible to tune the thickness of the shell. In this work we aimed to work with shell ranging between 1-5 nm. The method also proved to work for different core sizes, when the same deposition was carried out on AuNS of 60 and 67 nm. So, essentially the developed synthetic route enabled to obtain Au@Pd in which both the core size and the shell thickness can be tuned, offering a large set of particles that can be fabricated.

The method is not only constrained to fabricate monometallic shells. Beyond single metal layers, multimetallic coatings can be formed by simultaneous deposition of two different metals' precursors. Indeed, similar to a Au@Pd CS NPs, we also deposited Au and Pd, intending to obtain an alloyed shell. It is worth mentioning that additional steps might be taken to achieve the final product. Due to the different reduction potential of the precursors ($E^{\circ}_{AuCl_4^-/Au} > E^{\circ}_{PdCl_4^{-2}/Pd}$), it was required to equalize their reduction rate to induce their concomitant deposition. It has been shown that the $[Br^-]/[Cl^-]$ is a crucial factor modulating the final chemical composition of Au/Pd NPs, therefore we successfully tuned it to favour the alloy formation in the shell [102].

Core-Satellites The term core-satellite (also antenna-reactor) is used in this thesis for those structures in which a PNP are surrounded by catalytic metals, creating sub-nanometer interparticles gaps. In the literature one can find several ways to achieve such a conformation.

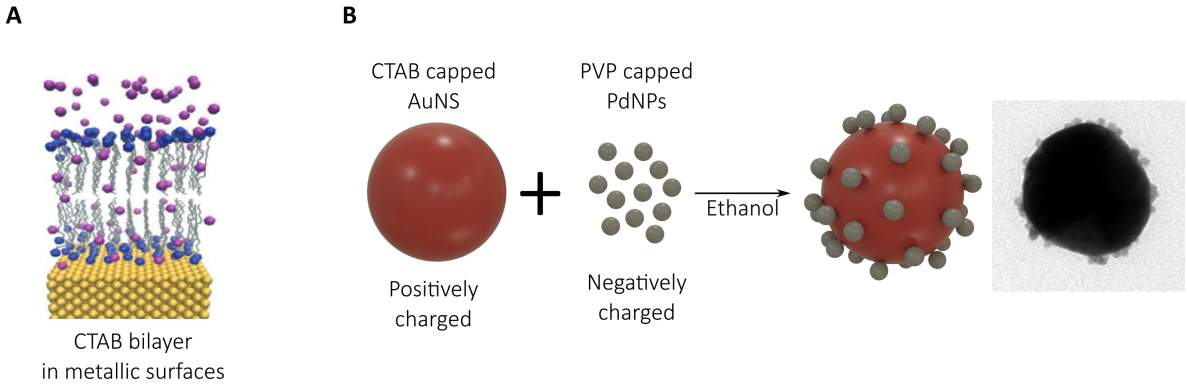

Figure 3.3: **Synthesis of Antenna-Reactor.(A)** CTAB stabilizes the synthesized AuNS by forming a double layer in which the hyprophobic tails are pointing towards the inner part, while the positively charged amines bind the Au surface and interact with the solvent. To obtain an antenna-reactor configuration, ethanol was employed as a stimulus, partially dissolving the double layer. The remaining CTAB molecules attract the negatively charged PdNPs, resulting in the final structure **(B)**. **(A)** Adapted from [103]

For example, some of the methods involve the inclusion of a very thin layer of SiO_2,

used as a spacer between the two nanoparticles [104, 105, 106], while other involve the use of molecules bridging the two nanoparticles (e.g. dithiols) [107]. Nevertheless, in these approaches, the catalytic metal is anchored by a thiol group (-SH). Due to the nature of the bond (covalent), the surface is restricted for molecules to react, thus reducing the catalysts' capabilities. To avoid it, a new method was developed here, which consisted in solvent-induced assembly [95].

In order to explain how the structures were obtained here, it is necessary to dive deeper in the way that surface molecules impart the stability in metallic nanoparticles. CTAB is an amphiphilic molecules, meaninig that it is defined by a hydrophilic (quaternary amines) region and a hydrophobic region (C_{16} alky chain). Therefore, for CTAB to stabilize NPs in aqueous medium, they form a bilayer in which the alkyl chains are sandwiched between the positively charged amines, one bound to the Au surface, the other interacting with H_2O molecules 3.3A [103]. The stability of CTAB capped NPs is sensitive to all kind of stimulus that deteriorate the double layer, and has been shown that ethanol can act as such an agent [108].

The assembly was therefore obtained as follows: ethanol is added to a solution of CTAB capped AuNS, partially dissolving the CTAB bilayer and introducing instability. The ethanol addition is immediately followed by the incorporation of negatively charged nanoparticles. The remaining positively charged molecules at the AuNS' surfaces attract the negative particles to finally yield the core-satellite structure (Figure 3.3B). Pd and Au@Pd NPs were employed as satellites, both around 5 nm in size and coated with PVP.

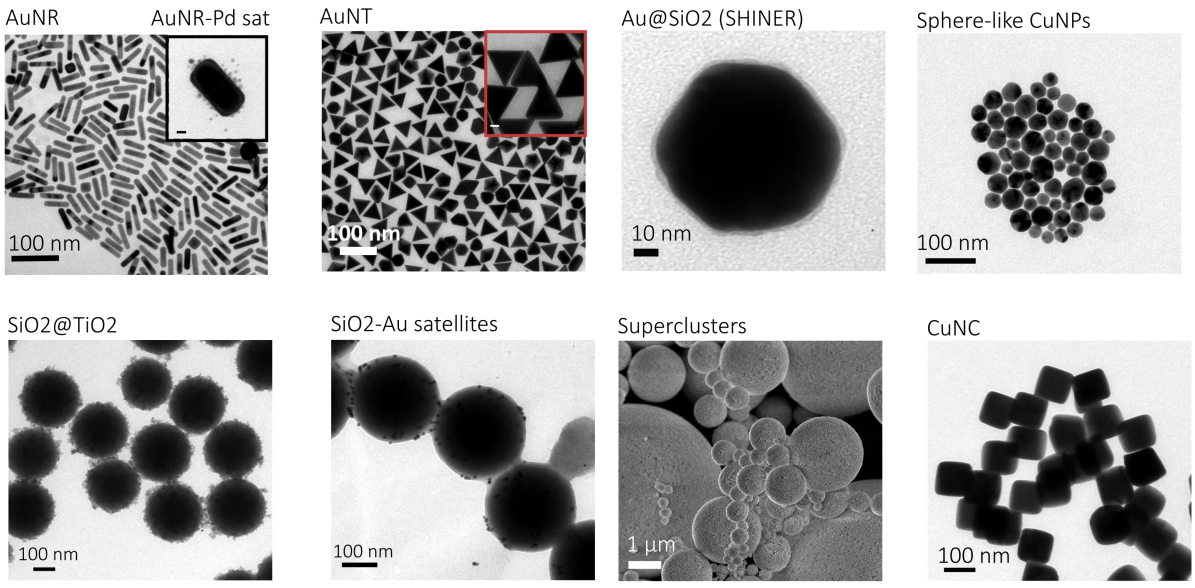

Figure 3.4: **Additional nanostructures.**These structures were also fabricated for different projects. The aim is to show the variety of shapes, sizes and combination of materials (metals and semi-conductors) that can be attained in colloidal fabrication of nanostructures.

3.1.4 Additional structures

The description given so far about the syntheses will help the reader to understand the results and interpretations provided in the next chapters. However, to conclude with the section fully dedicated to the synthesis, Figure 3.4 shows additional structures conducted in a similar time frame of this thesis. The demonstrate the variety of nanostructures that can be achieved if one masters the synthesis of nanoparticles. Examples of these, in my personal opinion, wonderful structures are Au nanorods (AuNR) and Au nanotriangles (AuNT). As they share the same surfactant as AuNS, the extension of the assembly was proven for the AuNR (inset). Also, structures denominated as SHINERS, composed of Au cores coated with thin SiO_2, were prepared. Synthesis on other metals (Ag, Cu) were also prepared. Similarly, it was possible to synthesize SiO_2 spheres with tunable sizes ranging between 200-600 nm using the well-known Stöber method. 10 nm AuNS or ∼5 nm TiO_2 was deposited on them. Copper oxide cubes Cu_2O were also succesfully synthesized. Last, micrometer spheres were obtained by assembling Au and Au@Pt nanoparticles giving rise to Superclusters.

3.1.5 Metasurfaces fabrication

We mentioned already that there are several strategies to trigger an assembly between colloidal nanoparticles. However, those methodologies use to breakdown if one wants to extend the assembly to larger regimes. Recently, a very sophisticated approach was described to achieve the assembly of AuNS into hexagonal closed packing (hcp) arrays [93]. The method relies on the governing hydrophobic interaction among the stabilizers. To achieve these structures, the CTAB at the surface of AuNS is first replaced by thiolated polystyrene (PSS), promoting their transfer from aqueous solvent to organic media (normally, toluene). If the solvent is slowly evaporated at a very low rate, the strong interaction between the PSS chains is what directs the assembly and the hexagonal arrangement. Hence, it is possible nowadays to use the nanoparticles as units to manufacture complex structures. Specifically for this approach, there are several parameters that can be adjusted based on the needs. The methods has been proven to work for different AuNS sizes functionalized with PSS of different lengths [109]. Since the optical properties of this type of structures were exploited to drive photocatalysis, a broader description of them is provided in Chapter 6.

3.2 Methods for NPs characterization

Here the reader will be provided with a brief description on techniques and setups that allowed us to correlate the catalyst performance with variables associated to its spatial distribution, metallic loads and final photocatalytic response.

3.2.1 UV-Vis spectroscopy

Ultraviolet-Visible spectroscopy (UV-Vis) is a well-established technique that enables to evaluate the interaction of the synthesized NPs with light corresponding to that particular wavelength range. Traditionally, the spectra were reported as absorbance as a function of the wavelength, due to the fact that electronic transitions in molecular complexes take place in that regime. However, a more accurate term when using it to study PNPs is *Extinction*. As mentioned, the extinction of light has two main reasons, which are absorption and scattering.

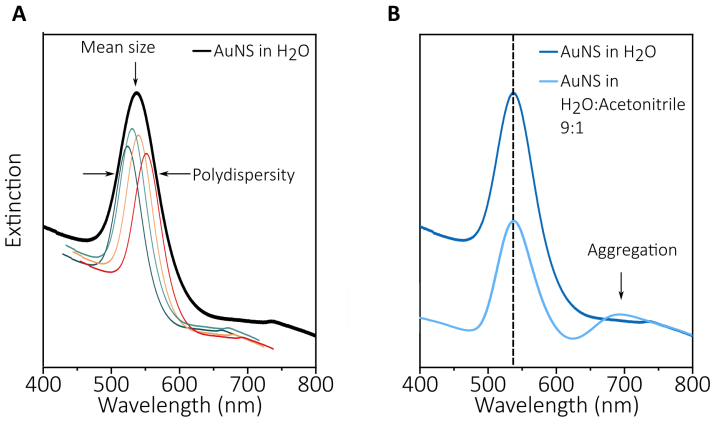

Figure 3.5: **UV-Vis spectroscopy.(A)** The black line represents the LSPR dipolar mode of a AuNS sample. The maximum provides information of the size range of the AuNS, while the bandwidth is correlated to its polydispersity. **(B)** Due to the strong optical coupling of PNPs when in close proximity, UV-Vis is also a good reported of the aggregation state of the sample.

Although rather simple, UV-Vis spectroscopy contains very valuable information related to the the size, polydispersity and stability of colloidal PNPs. As seen in Figure 2.4, the spectral position of the LSPR strongly dependes on the size. Specifically, it red-shifts with the increasing sizes. Thus, the spectrum determination can be used as a first approximation to the size range of the resulting PNPs. Moreover, besides being a proxy of the intrinsinc losses, the bandwidth also provides information about the polydispersity of the sample. If the size range of the fabricated PNPs is rather wide, it will be manifested in the LSPR bandwidth, since smallest particles will present blue-shifted resonances compared to the mean size, while largest would present a red-shift (Figure 3.5A.

Also, UV-Vis spectroscopy is a good reported of coalescence or partial aggregation of colloidal NPs. If the stability is reduced, some particles will be aggregated even in solution, and they will present a complete different spectral profile owing to their LSPR coupling. Therefore, shoulders at longer wavelengths are observable (Figure 3.5B) All in all, UV-Vis spectrosocopy is an easy technique, but powerful technique, that can be utilized in a daily basis as a reporter of dimensional parameters of the prepared PNPs sample, polydispertsity, absorption-to-scattering ratios, as well as their stability. All measurements in this thesis were conducted using a model Lambda 750 from Perkin Elmer.

3.3 Dynamic Light Scattering

Dynamic light scattering is a analytical technique that allows to gain information of the dimensions and also the surface charges of colloids. Unlike electron microscopies, it is not necessary to dry the sample and information can be obtained while NPs are suspended in solution. Its results are complementary to what is obtained with UV-Vis spectroscopy.

Essentially, the working principles are based on tracking over time the back scattered light from NPs suspended in solution upon interaction with the incoming laser. By correlating the fluctuations on the intensity of the scattered light over the time caused by the Brownian motion of the nanoparticles, it is possible to estimate the hydrodynamic radius of the scatterer (NPs). The dimensional parameters obtained via DLS are always larger than those obtained from microscopies such as Transmission Electron Microscopy (TEM) and the reason why is because ligands are included in the determination of the hydrodynamic radius. Furthermore, since the intensity of scattered light strongly depends on the size od the body (Rayleigh Scattering $I \propto r^6$), DLS is very sensitive to the formation of clusters of nanoparticles.

Nevertheless, the significance of DLS comes from the capability to determine the *Zeta Potential* (ζ) of the NPs. If an electrical potential is applied to the cuvette, the charged NPs will displace due to the electrostatic interaction (*electrophoresis*), causing again fluctuations in the scattered light. The ratio between the velocity at which the particles are displaced and the applied electric field (E) is defined as the electrophoretic mobility (μ_e), which has been demonstrated by Smoluchowski that depends linearly with ζ (Equation 3.1).

$$\mu_e = \frac{v}{E} = \frac{\varepsilon_r \varepsilon \zeta}{\eta} \tag{3.1}$$

Where ε_r and η are the relative permittivity and viscosity of the medium, typically H_2O. Therefore, DLS is also a useful technique which provides information about the size of the nanoparticles, stability and more impotantly, surface charge. All measurements were carried out using a Zetasizer Pro from Malvern Panalytical (λ= 632 nm).

3.3.1 Inductively coupled plasma - Atomic Emission Spectroscopy

This destructive spectroscopic method enables to determine the content of chemical elements through the detection of their characteristic emission lines. In a typical procedure, the sample is pumped into a plasma flame (Ar) at ∼6000 K and as a result of the interaction with the plasma, all constituents are broken apart to single atoms. The isolated atoms are subsequently excited and decay emitting characteristic photons, whose wavelength corresponds to the energy difference between the two levels involved in the transition. Therefore, well-defined spectral lines can be identified for each element, allowing its quantification. The sensitivity of the method enables to quantify the elements even when they are present at traces levels ($\sim \mu g\ L^{-1}$).

The sample preparation consists in the digestion of metallic NPs before the analysis. Normally, the NPs are dissolved in 1 mL of reversed aqua regia (HNO_3:HCl 3:1) and diluted

to 4 mL with HCl 2% wt. The determinations of metallic loads in this thesis were later employed to carry out a comparison on the catalysts' performances. All measurements were obtained using the spectrometer Agilent 5800 and calibration curves were always obtained using commercial standards for reliable quantification.

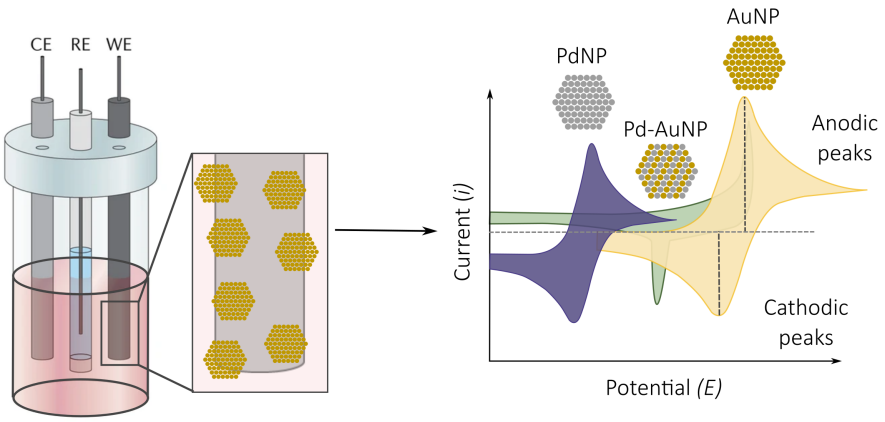

Figure 3.6: **Cyclic Voltammetry.**A three-electrode cell is composed by a reference, a counter and the working electrode (RE,CE and WE, respectively). By sweeping the potential of the WE with respect of the RE, it is possible to sense charge transfer processes occurring at the surface of the WE, manifesting as current. Supported NPs of different compositions can play the WE and thus, gain insight of their surface composition. In metallic particles the cathodic peaks use to refer to the reduction of of surface oxides, while the anodic peaks to its formation.

3.4 Cyclic voltammetry

Cyclic voltammetry (CV) is an electrochemical technique enabling to investigate charge transfer processes, such as reduction and oxidation reactions, occurring at the surface of the electrodes. In such experiments, the electric potential (E) is a tool that forces the system to advance either in its reductive or oxidative direction by applying negative or positive potentials with respect to a reference electrode. Therefore, in a typical plot of electric potential vs current (E vs. i), the potential is a metric for the input energy required to induce the reaction, while the current accounts for the reaction rate. Figure 3.6 illustrates a three-electrodes cell similar to the one used in this thesis. In our setup, we used a Ag/AgCl reference electrode (RE), a Pt mesh serve as counter electrode (CE) and the Flurine-doped tin oxide (FTO) supported PNPs played the working electrode (WE). To fabricate the WE, the investigated systems were dropcasted on an ITO piece and once dried, a commercial Nafion solution was also dropcasted to keep the catalysts supported during the analysis.

This technique was used to gain insight on the surface composition of nanoparticles, since changes in surface composition will be manifested as a shift in the position of E. The voltammograms were obtained in KOH (0.5 M) at a scan rate of 0.05 V/s. The solutions

were bubbled with N2 for 30 min before the experiments. A total number of 30 cycles were recorded and the last one is always shown. The electrochemical investigation of the electronic properties of the NPs were investigated with a 760 E potentiostat from CH instruments.

3.4.1 Electron Microscopies

Transmission Electron Microscopy Electron microscopes were invented as an alternative to the diffraction limited optical microscopes, which fail to resolve fine details of materials with dimensions smaller than approximately half of the wavelength used in optical microscopes (visible range). In a simple way, an electron beam delivers electron which are accelerated with voltage towards the sample (target). The electrons passing through the sample (*transmitted electrons)* are then collected by a camera, creating an image out of their interaction with the body. Due to the fact that electrons can be scattered away by spurious bodies, the imaging process is carried out in vacuum. With the increasing ability to fabricate materials in the nanometer range, Transmission Electron Microscopy (TEM) became an important tool for the morphological and dimensional characterization of the nanoparticles.

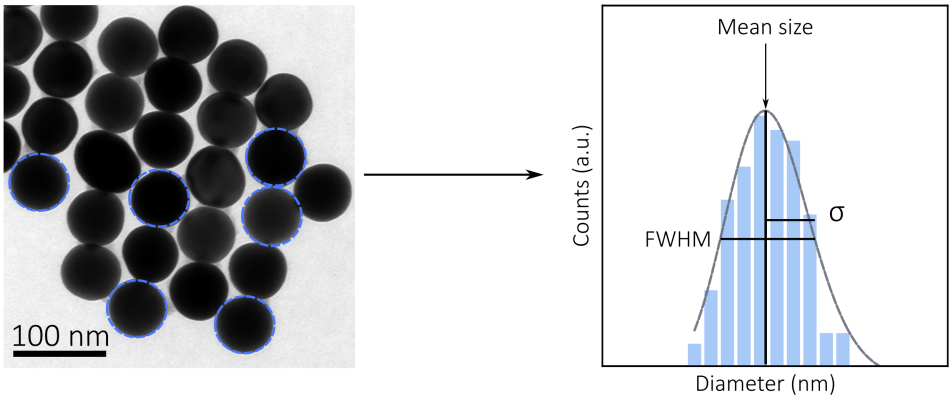

Figure 3.7: **Data treatment in TEM images.**A TEM image with sufficient resolution was employed to determine the size and shape of the NPs. In a typical procedure, the NPs are assumed spherical and the diameter can be determined by the cirular cross-section. By fitting a resulting histogram, it is possible estimate statistically the mean size and the polidistersity of the population. Gauss function was always use for the fit and the sizes were reported as Mean size$\pm\sigma$, obtained from the fit.

TEM was extensively used in this thesis to characterize the shape, size and spatial distribution of bimetallic nanoparticles attained via wet chemistry. The sample preparation consisted on drop-casting a solution of colloidal PNPs onto carbon/formvar 200 mesh Cu grids, letting the solvent evaporate at room temperature. Once dried, the samples were gently rinsed with EtOH to remove the presence of ligands. The imaging was performed on a commercial microscope from JEOL (model JEM-1011 operated at 80 kV). Figure 3.7 shows the analytical procedure employed to determine the size of PNPs. The images were

analyzed using a ImageJ, a free software enabling to determine the area of the nanoparticle. The synthesized nanoparticles were mostly spheres, therefore, a circular shape was assumed from which the diameter was determined. Statistic analysis were always conducted with populations of N>100, fitting the resulting histogram with a Gaussian function. The results were always reported as mean diameter ± standard deviation.

Scanning Electron Microscopy Similar to what has been briefly described for TEM, a scanning electron microscopes (SEM) also works by accelerating the a beam of electron towards the sample. Nevertheless, instead collecting the transmitted electrons, the scattered electrons from the surface of the sample are collected. Due to the fact that scattered electrons are detected, SEM enables to obtain a three dimensional perspective of the sample and primarily its surface, since typically scattered electrons come from from different depths within the sample. For this reason, SEM and TEM are complementary.

Here we used to confirm the self-assembly of NPs conduced in solution, as well as the number of layers in metasurfaces, as shown in Chapter 4. For the analysis, silicon (Si) wafers were employed as support for the drop-casted NPs. Samples were also rinsed with ethanol before being imaged. were observed by using a Zeiss Ultra Plus high-resolution SEM operated at 10 kV.

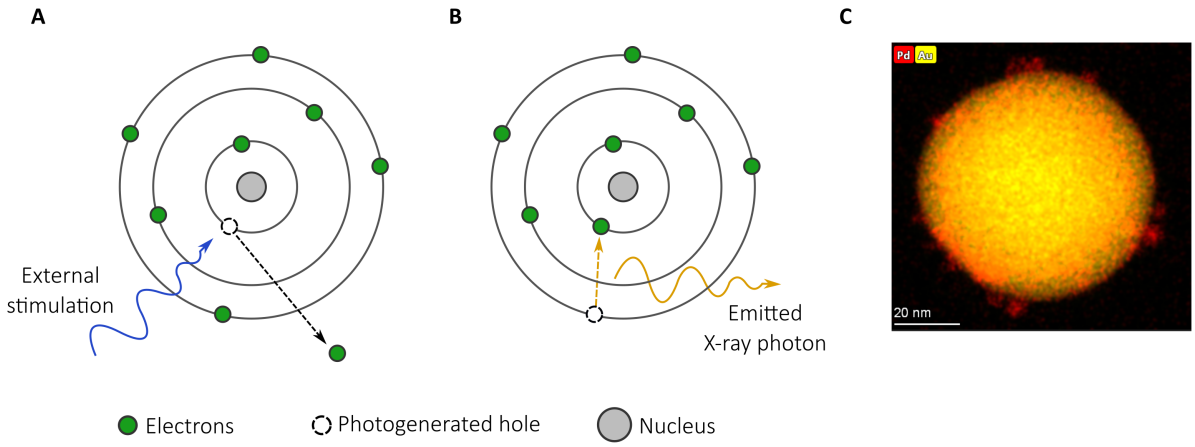

Figure 3.8: **Energy dispersive X-Ray spectroscopy.(A)** The scheme shows the photoemission of an electron occupying an inner electronic level, resulting in the formation of a photogenerated hole. The emission can be cause either with X-rays or electron beam. **(B)** Electrons on higher electronic levels fill the photogenerated holes, emitting a characteristic photon whose energy is equal to the energy difference of the involved levels. Due to the discrete nature of the electronic levels, different elements can now be identified and thus, mapped to assess the spatial distribution of the constituents of NPs **(C)**.

3.4.2 Energy dispersive X-ray spectroscopy

The fundamental principles of Energy dispersive X-ray spectroscopy (EDX) relies on the the photoejection of electrons occupying inner levels of an element's discrete electronic

states (Figure 3.8A) by either absorbing an X-ray photon or the collision with accelerated electrons coming from a beam. The resulting photogenerated hole is later occupied by electrons on higher electronic levels, which decay emitting an X-ray characteristic photon (Figure 3.8). The detection of the emitted photons allows to identify chemical elements. For this reason, EDX is often employed to map the spatial distribution of chemical elements.

EDX was utilized to determine the successful deposition of one metal on top of the other in CS NPs, as well as to confirm that the two metallic constituents of bimetallic samples can be arranged with different spatial configuration. The sample was prepared in the same way as for TEM analysis. The analysis was performed at 300 kV on a probe corrected Titan Themis equipped with a Super-X EDX detector.

3.5 Antistokes Thermometry

The determination of surface temperature in PNPs has been one of the greatest concerns of the field. Recently, Anti-Stokes thermometry has been proposed as one of the methodologies enabling to access to such property at the single-particle level. The method benefits from the photoluminescence (PL) of PNPs, exploiting the temperature-dependence of Anti-Stokes (AS) photon emission (shorter λ) and independence of Stokes (S) emission.

$$I^S(\lambda, \lambda_{Exc}, T) \propto I^{Exc} f_{PL}(\lambda, \lambda_{Exc}) \tag{3.2}$$

$$I^{AS}(\lambda, \lambda_{Exc}, T) \propto I^{Exc} f_{PL}(\lambda, \lambda_{Exc}) n_{BE}(\lambda, \lambda_{Exc}, T) \tag{3.3}$$

$$n_{BE}(\lambda, \lambda_{Exc}, T) = \left[e^{(E^{\lambda} - E^{\lambda_{Exc}})/k_B T} - 1 \right]^{-1} \tag{3.4}$$

Parameters in equations 3.2 and 3.3 are the AntiS-Stokes $I^{AS}(\lambda, \lambda_{Exc}, T)$ and Stokes $I^S(\lambda, \lambda_{Exc}, T)$ PL emisison at a wavelength λ, under excitaiton with a laser of wavelength λ_{Exc} and irradiance I_{Exc}. The instrinsic PL emission spectrum is represented by f_{PL}, while $n_{BE}(\lambda, \lambda_{Exc}, T)$ is the temperature-dependent distribution of states responsible for the anti-stokes emission, described by a Bose-Einstein distribution.

As can be realized, an increase in the intensity of the PL (both, AS and S) is expected with an increase in the irradiance. However, the AS signal should have an additional increase due to the heat delivered by the PNPs upon resonant illumination. Therefore, if one do the ratio between the intensity of AS signal at two different irradiances, the following equation is obtained

$$Q^{AS}_{i,j} = \frac{I^{AS}_i}{I^{AS}_j} = \frac{I^{Exc}_i}{I^{Exc}_j} \frac{e^{(E^{\lambda} - E^{\lambda^{Exc}})/k_B T_j} - 1}{e^{(E^{\lambda} - E^{\lambda^{Exc}})/k_B T_i} - 1} \tag{3.5}$$

Assuming that the temperature scales linearly with the irradiance due to absorption of PNPs ($T_i = T_0 + \beta I^{Exc}_i$), where β represents the photothermal coefficient, then the expression in Equation 3.5 is re-written as:

$$Q_{i,j}^{AS} = \frac{I_i^{AS}}{I_j^{AS}} = \frac{I_i^{Exc}}{I_j^{Exc}} \frac{e^{(E^{\lambda} - E^{\lambda^{Exc}})/k_B(T_0 + \beta I_i^{Exc})} - 1}{e^{(E^{\lambda} - E^{\lambda^{Exc}})/k_B(T_0 + \beta I_i^{Exc})} - 1} \tag{3.6}$$

Which is an equation with two free parameters, T_0 and β, and if one is known, the other can be calculated. Experimentally, the PNPs are illuminated at different irradiances by changing the relative position between the beam and the nanoparticles, which are typically fixed on a support, enabling to create a hyperspectral image for every individual NP. The experimental $Q_{i,j}^{AS}$ are fitted with equation 3.6 and β extracted from the fit (Figure 3.9).

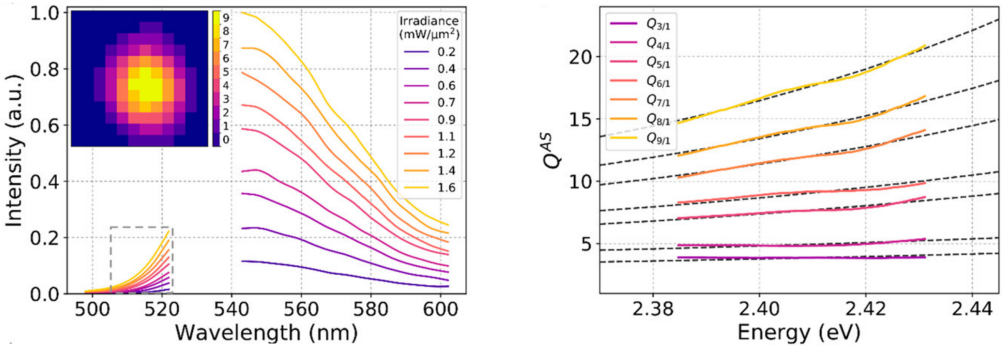

Figure 3.9: **Anti-stokes Thermometry.**The PL emission spectrum of a PNP depends on the incident irradiance, as shown for a single AuNP illuminated on-resonance with a green laser (left panel). The PL can occur at higher (Anti-stokes) or lower energy (Stokes). As anti-stokes PL also depends on the temperature, it is possible to determine the photothermal coefficient (β), accounting for how much a AuNS heats up upon illumination, by fitting the ratio between the anti-stokes intensity at two different irradiances with equation 3.6. Right panel shows how experimental data is fitted to obtain β for a single NP.

This procedure was employed to determine the photothermal coefficient and study the photothermal properties of plasmonic bimetallic NPs. The sample preparation consisted on optically printing the nanoparticles creating grids of single-particles. A continuous wave λ=532 nm laser focused near its diffraction limit was used to acquire their PL spectra in H_2O. The measured range was from 500 nm to 600 nm, employing two 532 nm notch filters to filter the laser line. Hyperspectral confocal images of samples named as 67 nm AuNS, Au67@Pd2 CS-NPs and Au67@Pd4 CS-NPs were acquired using a maximum irradiance of 2.1, 2.8, and 2.7 mW μm^{-2}, respectively. For 60 nm AuNS, Au60-Pd-Sat, and Au60@Pd2 CS-NPs, the irradiances were 2.0, 2.4, and 4.9 mW/μm^{-2}, respectively. The data treatment was conducted as follows: β for each particle was obtained by averaging the values of each i,j combination. The averaged β was averaged by the total number of measured nanoparticles (N).

3.6 Time-resolved Spectroscopy

Time-resolved spectroscopy -also known as transient-absorption spectroscopy (TA)-, allows to investigate the temporal evolution of an excited system in timescales corresponding to the femtosecond regime (or slower) [110, 111]. Generally, in this type of pump and probe spectroscopies, one compares the sample's absorption before (t<0) and after (t>0) it has been excited with the pump (t=0), connecting the spectral differences with internal electronic transitions taking place in the sample. An scheme of this process pumping with a single-wavelength source and probing with a broadband source is presented in Figure 3.10. The differential absorption (dA) can either be plotted as a function of the wavelength, accounting or as a function of the time, indicating the lifetime of the excited state.

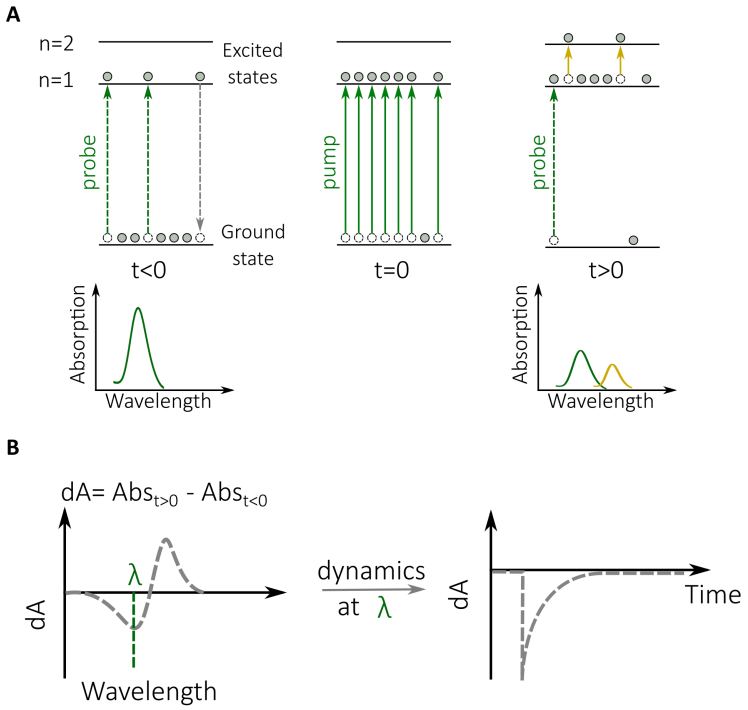

Figure 3.10: **Time-resolved spectroscopy.** **(A)** Scheme representing the phenomena occurring in time-resolved spectroscopy. **(B)** The contrast when measuring differential absorption (dA) of the sample before and after being pumped allows to identify the lifetimes of excited states. The differential absorption can be expressed as a function of the wavelength at a time after the pump, or as a function of time for a particular wavelength.

We utilized TA spectroscopy to understand the dynamics of LSPR in plasmonic and catalytic NPs when photoexcited with visible light. The data was obtained using an Ultrafast Systems Helios Transient Absorption Spectrometer. Pulses of 35 fs were generated by a mode-locked Ti:sapphire oscillator (SpectraPhysics MaiTai) and amplified by chirped pulse

amplification (SpectraPhysics Spitfire Ace) operating at 1 kHz. Spectra were recorded for varying delay times in transmission with an averaging time of 1 s.

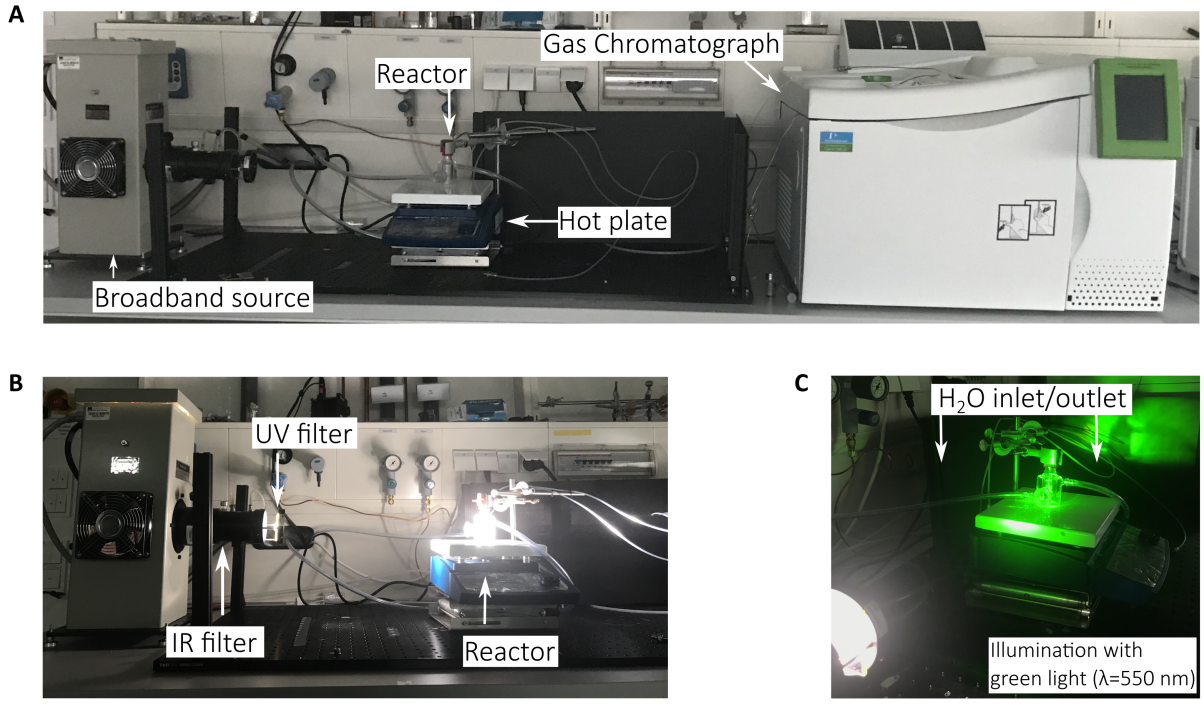

Figure 3.11: **Photocatalysis setup.(A)** Image of the homemade setup to evaluate the influence of light on catalytic reactions emplying PNPs as catalysts. It consists on a broadband source, a hot plate to homogenize the solution, a reactor plugged to a cryostat allowing to control the overall temperature and finally a Gas cromatograph to detect and quantify the produced H_2 in a characteristic reaction time. **(B)** Imaging when operating in illumination conditions. To ensure the sole visible light regime reaching the reactor, IR and UV filters were coupled to the lamp. **(C)** It was also possible to use bandpass filters to elucidate the influence of the different regions within the visible range. As an example, the lamp filtered in the green is shown.

3.7 Photocatalysis setup

In order to properly assess the influence of light on the performance of the fabricated entities when assisting chemical reactions, it was necessary to build-up a setup accordingly. Essentially, the setup contained a reactor, a source of light and detecting setup. The final configuration is shown in Figure 3.11A. The glassware reactor was a 15 mL container surrounded by a water jacket, which allowed to pump water in and out and thus, control the temperature across the course of the experiment (normally, t= 1h) using an external cryostat. When carrying out experiments under illumination, a solar simulator from Newport, VeraSol-2 LED Class AAA, operated in AM1.5G, was employed as a source of light. The

benefits of using the solar simulator relies on the opportunity to test the catalysts in more realistic conditions.

When conducting power and wavelength dependent, the Xe Arc lamp (broadband lamp (*Newport, model 66921*) was equipped with a longpass and an IR liquid filter (6123NS), thus enabling us to work only with the spectral regime corresponding to the visible. The IR filter consisted in a H_2O tank of 10 cm of optical path, avoiding the solvent absorption (heat accumulation) in the reactor (Figure 3.11B). Different spectral regions within the visible were filtered using bandpass filters, as shown in Figure 3.11C. In that particular case, a bandpass filter centered at λ=550 nm and a bandwitdth of 20 nm was used enabling only letting green light to go through.

In every experiment, the reactor was stirred with a hotplate to promote the homogeneity in reaction conditions. Also, the employed solvent was always bubbled with N_2 for 30 min before the beginning of the reaction, eliminating any spurious gas affecting the H_2 detection (e.g O_2).

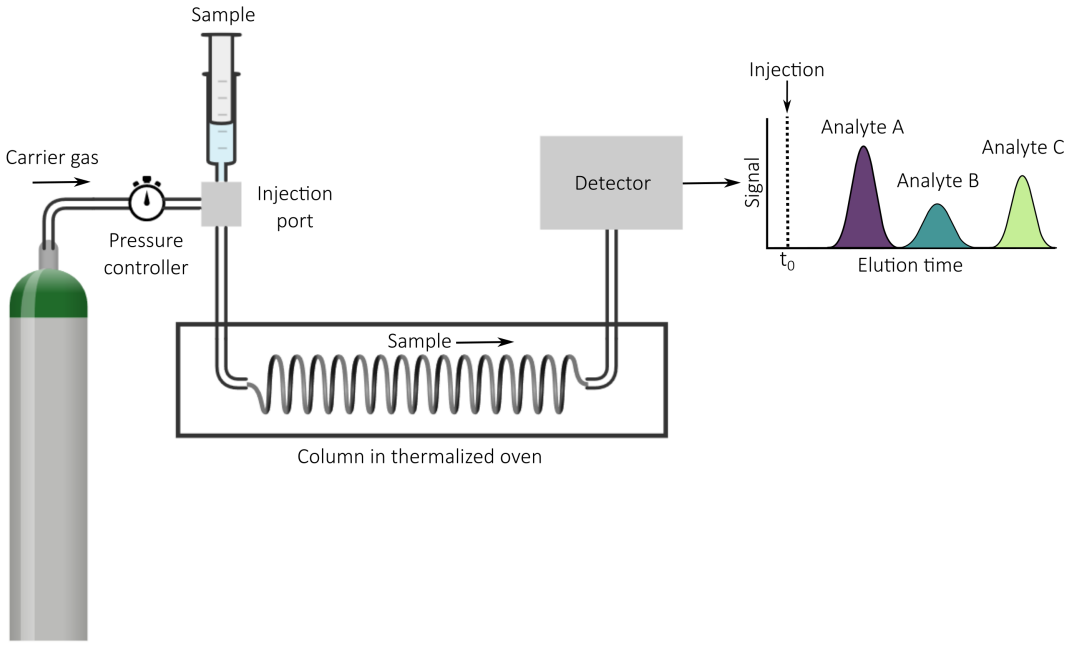

Figure 3.12: **Gas Chromatography.** Scheme of a gas chromatograph. The sample is injected and carried to the thermalized column. The compounds experiencing the strongest interactions will be delayed with respect to those that experience the weakest. As a result, the components of a complex sample are now separated and can be detected at the time that they leave the column. When characterizing the elusion time, quantification can be carried out by comparing to external standards.

3.7.1 Gas Chromatography

Chromatographies are in general techniques employed to separate components of a complex sample. In particular, Gas Chromatography is an analytical tool useful to separate con-

stituents of a gas mix. The operating principles rely on the interaction of all constituents with a column in which the gas phase is forced to circulate. This way, those molecules experiencing a strong attraction to the column are diffusing at a slower rate in comparison to those that experience a weak interaction. The interaction strength is what determines the time of the compound in the column, and thus, the *elusion time*. The scheme of the technique is shown in Figure 3.12. Gas chromatography was chosen as a detection technique because most of Formic Acid dehydrogenation products are transfer to gas phase during the reaction course.

For gas detection, a gas cromatograph from Perkin–Elmer was utilized (Clarus 590 GC), equipped with both a flame ionization detector (FID), to detect organic traces, and a TCD for H_2 detection. In addition, the FID detector was coupled to a H2 generator from Perkin Elmer (NM plus H_2 100). Argon (Ar) was used as a carrier gas.

For the quantification, a calibration curve was performed using external H_2 standards with different concentrations (100, 500 and 1000 ppm in Ar, Linde). The external standards allowed us to correlate the H_2 moles with the peak area of the signal at the chromatograms. The obtained calibration curve is shown in Figure 3.13. In every experiment, 400 μL were always sampled from the head space and analyzed. The corresponding area was introduced in the calibration curve (Supplementary Figure 3.13), and the moles were later referred to the head space's total volume (5 mL) to estimate the total production.

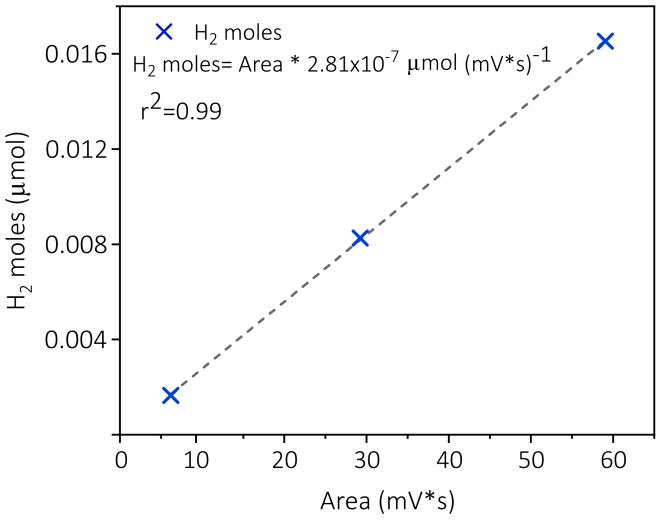

Figure 3.13: **Calibration curve for H_2 Detection in Photocalysis Experiments.** Linear fit of H_2 moles in standard samples. This calibration curve was used to estimate the H_2 moles in photocatalysis experiments.

Combining the determined H_2 with the metallic load estimated by ICP-AES, the photocatalytic rates were always expressed as always expressed as presented in Equation 3.7. The reaction rates established a parameter to compare the performance of the synthesized catalysts when operating with and without illumination,

$$\text{Reaction rate} = \frac{\text{H}_2 \text{ moles}}{\text{g catalyst} \times \text{time}} \tag{3.7}$$

3.8 Optical Simulations

Computational electrodynamics are a valuable tool to understand the interaction of the incoming light with plasmonic nanoparticles from a classical perspective. One of the most common approaches to simulate electromagnetic dynamics is the finite-difference time-domain method (FDTD) [112]. These type of methodology operates by solving how an electromagnetic wave propagates through a structure in a medium, which translates as solving Maxwell's equations on a user-defined region. It can be applied to calculate reflectance, transmission, absorption profiles, polarization-dependent and wavelength-dependent response of the investigated body [113].

In this thesis, we used FDTD simulations to achieve a deep comprehension of the underlying physical phenomena governing the photocatalytic response of the synthesized plasmonic bimetallic nanostructures. These results were complemented with the experiments to accomplish an integrated understanding on how the incoming light was converted into reaction products. These type of optical simulations were carried out by our collaborators Dr. Baptiste Auguié and Sabrina Jürgensen.

Chapter 4

Geometry-dependent reactivity of plasmonic bimetallic nanocatalysts

In Chapter 2 the reader was provided with a robust description of the most relevant bimetallic systems reported in the literature, as well as, the physical phenomena associated to every single way to spatially arrange materials comprising the hybrid catalyst. There is no such of a perfect system and all of them present advantages and disadvantages. For example, some of them (e.g. core@shell) offer an entire reactive surface and the possibility to transport charges across the interface between the materials, although this feature is also detrimental for their ability to interact with incoming light. Others, such as alloys, preserve the optical properties and even modulate activation barriers, but they also deal with phase separation and the lack of control in their massive preparation [77, 87]. It is very clear that the architectonic aspect of the catalyst plays a major role in the energy flow in the plasmonic-catalytic combination. This establishes that it is not sufficient to simply combine good energy harvesters —a plasmonic particle—, and good charge injectors —a catalytic metal—, and certainly one must also consider the structure-performance correlation [114]. In spite of considerable progress on both experimental and theoretical fronts [15, 62, 115], the little clarity on which of these designs leads to the most efficient light-to-chemical conversion efficiency was a central question of the field. To this end, we dedicated our efforts to fill this gap in the literature, presenting approach and findings are described along this chapter.

By way of introduction, we carefully designed experiments to compare different combinations of Au and Pd components, addressing all possible combinations describe throughout Chapter 2. The catalysts were tested for H_2 generation under simulated sunlight illumination conditions. Formic Acid (FA) dehydrogrenation was chosen as a model reaction. The remarkable control on the catalysts architecture, the experiments conducted in identical conditions and their complement with electromagnetic simulations enabled us to conclude that antenna-reactor structures are the ones maximizing the correlation of sunlight absorption and catalytic performance. The aim of this investigation is to provide insight in the design of the next generation of light harvesting materials for photocatalysis based on PNPs.

4.1 Fabrication and characterization of nanocatalysts

The preparation of catalysts is a crucial task to accomplish a realistic comparison and understanding of the phenomena governing their performance in reaction conditions. In this regard, a mindful elaboration on the composition and morphological aspects of the catalysts is one the foremost tasks to conduct the proper assessment of the strucutural-dependent reactivity. The proposed systems to carry out the analysis, corresponding to each of the possible combination, are illustrated in Figure 4.1. As can be appreciated, Au nanospheres (AuNS) utilized were present across all systems, serving as both template and antenna in the related bimetallic system. The utilization of the same component in all structures enabled to work with a plasmonic behavior baseline. Specifically, it was proposed to coat the AuNS with either a thin layer of Pd (Figure 4.1A) or a AuPd bimetallic shell (Figure 4.1B) . Analogously, the same structures were aimed to be built-up in a antenna-reactor/core-satellite configuration (Figure 4.1C,D). The section will start describing the experimental approach used to synthesize the core and will continue with the description of the binary entities.

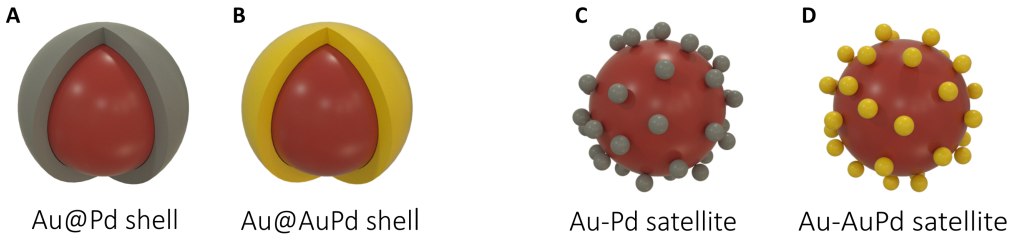

Figure 4.1: **Illustration of view of the four bimetallic catalyst. Chemical and optical characterization**. **(A)** core-shell type in which a AuNS is coated with a thin Pd shell. **(B)** core-shell type in which a AuNS is coated with a thin AuPd shell. **(C)** core-satellite type in which a AuNS is surrounded by small Pd satellites. **(D)** core-satellite type in which a AuNS is surrounded by small Pd satellites.

4.1.1 Au cores (AuNS)

The initial AuNS were fabricated following a well-known and reproducible method based on the employment of Au clusters as seeds for the growth of nanospheres to the targeted size [99]. The method enables to obtain AuNS with a very smooth surface employing Cetyl Trimethyl Ammonium Bromide (CTAB) and chloride (CTAC) as surfactants (see Appendix B for details). Through a microscopic characterization (TEM), it was determined that spherical particles with averaged diameter of 61±1 nm were prepared. Figure 4.2 shows a representative TEM image of the sample and the corresponding size distribution. The homogeneity throughout the sample was confirmed by SEM, also shown on the right panel of Figure 4.2.

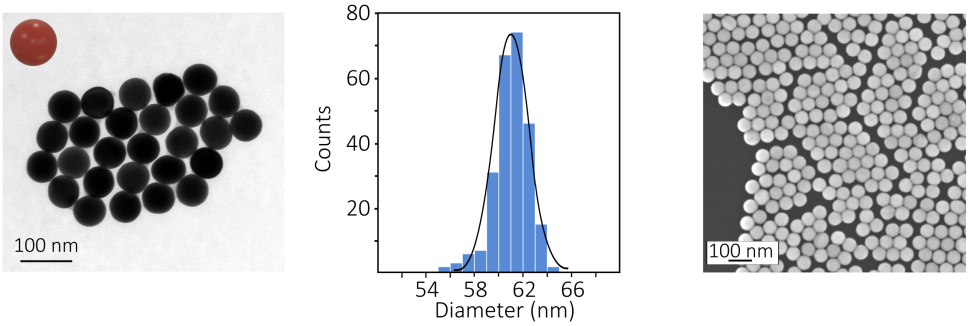

Figure 4.2: **Characterization of AuNS**. The AuNS employed as plasmonic component across all samples were determined to be 61±1 nm in size. Representative TEM and SEM images of the samples are provided to verify the very narrow size dsitribution and homogeneity of the particles among themselves.

It is possible to determine with high accuracy the resulted number of particles by means of their optical response [116], tool that facilitated the approximation on the calculation of number of nanoparticles employed in the synthesis of further structures, as well as, in photocatalytic experiments. While the LSPR of the AuNS depend on many variables (e.g. amount of surfactant, shape and size of the particle, etc.), the extinction at 400 nm mainly corresponds to the inherent Au interband transitions, and in this spectral regime the absorption is relatively unaffected by the LSPR. Hence, the number of AuNS was used the synthesis (N $\sim 2 \times 10^{11}$ NPs) of bimetallic nanocatalysts was estimated as follows.

On the one hand, the Au^0 concentration ($[Au^0]$) is estimated by taking the extinction of Au NS at 400 nm, a wavelength dominated by Au's interband transitions and is therefore largely insensitive to the morphology or environment of the particles.

$$[Au^0] = \frac{(Extinction_{400} \times 0.5mM)}{1.2} \tag{4.1}$$

The experimental *Extinction* at 400 nm is obtained from UV-Vis spectra once the solvent contribution has been substracted. In order to calculate the mass of Au^0 (m_{Au^0}), the sample volume (V_{sample}) and Au atomic mass (M_{Au}) are considered.

$$m_{Au^0} = [Au^0] \times V_{sample} \times M_{Au} \tag{4.2}$$

On the other hand, a 60 nm Au NS should have a corresponding mass of

$$m_{Au-sphere} = V_{Au-sphere} \times \rho_{Au} = \frac{4\pi {r_{Au-sphere}}^3}{3} \times \rho_{Au} \tag{4.3}$$

The ratio between the experimental Au mass (m_{Au^0}) and the mass of a 60 nm Au sphere $m_{Au-sphere}$ yields the number of NS, and therefore, the concentration (Au NS/L).

$$N_{Au-NS} = \frac{m_{Au^0}}{m_{Au-sphere}} \tag{4.4}$$

$$[AuNS] = \frac{N_{AuNS}}{V} \tag{4.5}$$

Note that taking into account the obtained size distribution does not affect substantially this estimate.

4.1.2 Core@Shell

The individual bimetallic nanostructures possess different nature and as such, different synthetic routes were developed for their accomplishment. Core@shell nanoparticles demand the deposition of one material on top of the other, therefore they were obtained by reducing Pd for the monometallic (Au@Pd), and Au and Pd precursors for the bimetallic shell (Au@AuPd) at high temperatures in the presence of CTAB/CTAC mixture.

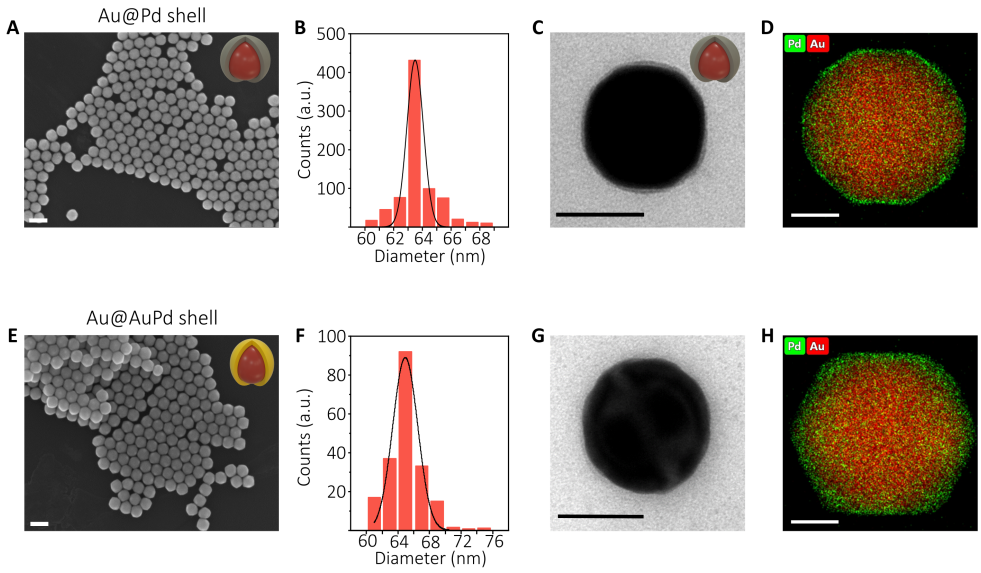

Figure 4.3: **Chemical characterization on Core@Shell NPs**. **(A)** SEM image of Au@Pd core@shell nanoparticles, indicating homogeneity throughout the components of the sample. **(B)** Size distribution of Au@Pd, revealing that the Pd shell was ≈1 nm (63±1).**(C)** TEM image of a representative nanoparticle, the metal can be tell due to their different contrast. **(D)** Elemental map of a single particle, confirming the presence of Pd only at the surface.**(E)** SEM image of Au@AuPd core@shell nanoparticles, indicating homogeneity throughout the components of the sample. **(F)** Size distribution of Au@Pd, revealing that the AuPd shell was ≈1.5 nm. (64±2) **(G)** TEM image of a representative nanoparticle. **(D)** Elemental map of a single particle, in which both Au Pd were observed at the surface. Scale bar in SEM images: 100 nm. Scale bar in TEM: 50 nm. Scale bar in EDS: 20 nm.

It must be noted that due to their different reduction potential ($E^{\circ}_{AuCl_4^-/Au} > E^{\circ}_{PdCl_4^{-2}/Pd}$) and therefore, stability, an adjustment on the halide's ratio was conducted prior to the reduction step in the bimetallic shell [102]. This way, the reduction potential were more alike, diminishing the reduction rate of Au salts and thus promoting the alloy formation by

reducing Pd and Au precursors simultaneously, instead the one-by-one reduction. Details on the synthesis can be found in Appendix B.

Concerning the Au@Pd core-shell structure, the homogeneity on the sphericity of the nanoparticles was proven to be preserved by imaging the sample using SEM (Figure 4.3A). The thickness was estimated to be 1 nm by comparing Au@Pd mean sizes from their respective size distributions (Figure 4.3B) with the one obtained for the initial Au NS. Figure 4.3C is a TEM image with high magnification which confirms the presence of Pd on the AuNS, due to the different contrast of the metals. The material composition of Au@Pd was studied by Energy-Dispersive X-Ray spectroscopy (EDS). As expected, the obtained map confirmed the presence of Pd only at the surface of the nanocatalyst (Figure 4.3D).

A similar analysis was carried out to determine the properties of Au@AuPd core-bimetallic shell. The size distribution of the revealed an increase on the mean diameter upon reduction of both precursors, although the homogeneity was still preserved (Figure 4.3E,F). A representative particle of the sample is shown in Figure 4.3G, which in comparison, evidences the larger size. EDS elemental mapping (Figure 4.3H) confirmed the presence of both metals at the surface, however to obtain a larger statistic on the composition, electrochemical characterization was conducted. The convenience of this approach over the microscopic one relies no the capability to sense more particles simultaneously, which otherwise would lead to an extremely long time with microscopies.

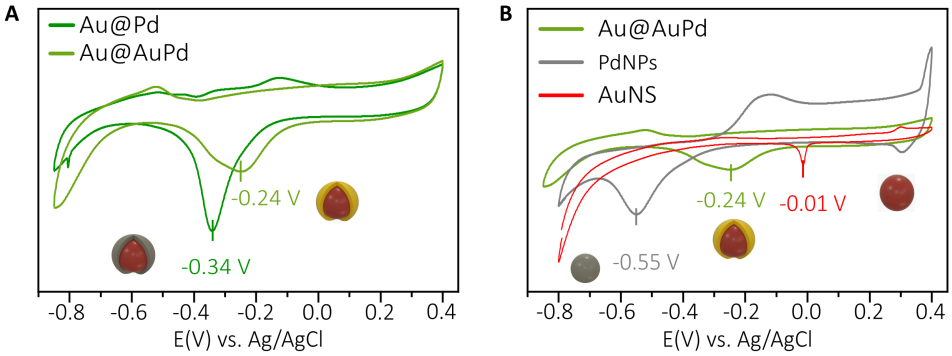

Figure 4.4: **Electrochemical characterization of Core@Shell NPs**. **(A)** CV of FTO-supported Au@Pd and Au@AuPd core-shell catalysts. The bimetallic shell is shifted to more positive reduction potentials in comparison with pure Pd shell. **(B)** CV of pure Pd NPs, pure Au NPs and Au@AuPd core-shell NPs. The alloy reduction curve falls between both Pd and Au reduction peaks, confirming an alloy with 1:1 Au-to-Pd ratio.

As described in Chapter 2, the electronic properties of the bimetallic shell can differ from its monometallic counterpart, and we expected to track those differences by running cyclic voltametries in alkaline media [86, 117]. To investigate the surface chemical composition electrochemically, the catalysts were dropcasted on a fluorine-doped tin oxide glass (FTO), followed by the addition of commercial Nafion solution upon solvent evaporation, which helped to keep the catalysts supported during the analysis. The FTO supported catalysts

played the role of Working electrode (WE), whereas the Ag/AgCl and Pt electrodes were used as reference (RE) and counter electrode (CE), respectively. The voltammograms were obtained in KOH (0.5 M) at a scan rate of 0.05 V/s in solutions previously bubbled with N_2 for 30 min. A total number of 30 cycles were recorded and the last one is plotted in for each catalyst.

The voltammograms are shown in Supplementary Figure 4.4. In effect, the bimetallic shell displayed a peak shifted 0.1 V to more positive reduction potentials when compared against the monometallic shell (panel A). The shift of the AuPd alloy shell reduction curve to a lower potential is typical for AuPd alloy [118,119]. Additionally, the shift is expected to be linear with the changes in the composition, and cathodic peak of the alloyed shell falls in the middle of the cathodic peaks for both pure Pd NPs ($PdO_X \rightarrow Pd^0$), later used as satellites, and Au NS ($AuO_Y \rightarrow Au^0$), suggesting that synthetic method yielded a 1:1 Au-to-Pd ratio [118,119,120]. Last, Inductive Coupled Plasma Atomic Emission Spectroscopy (ICP-AES) analysis confirmed a Au-to-Pd ratio of 1:1 for the shell, as presented in Table 4.1. An alloy with this chemical composition (Au:Pd 1:1) is determined to be the most reactive surface among the possible alloy compositions [121,122].

Catalyst	Au total (mM)	Pd Total (mM)	Au in shell (mM)	% Au	%Pd
Au NS	1.14	-	-	100	-
Au@AuPd	1.34	0.19	0.20	51.29	48.71

Table 4.1: ICP-AES analysis used to determine Au to Pd ratio for the alloyed shell in Au@AuPd core-shell nanocatalyst.

4.1.3 Core-satellites

As an alternative configuration to the continuous shells of Au@Pd and Au@AuPd, we also considered core-satellites (or antenna-reactor) structures, in which there is a physical gap in between the core and the satellites. Prior to the fabrication of the two-bodies structures, a synthesis a full characterization of the composition of satellites were conducted. Scanning Transmission Electron Microscopy in High-Angle Annular Dark-Field (STEM-HAADF), Energy Dispersive X-Ray Spectroscopy (EDS), UV-Vis spectroscopy and Cyclic voltammetry (CV) were employed to investigate the composition, optical and electronic properties of the satellites, respectively. The results of the set of techniques is presented in Figure 4.5.

Figure 4.5A,B show the STEM-HAADF and an EDS elemental map of a representative Pd NP used as satellite (Pd sat). As expected, only Pd was seen in the map. As for the Au-Pd satellites (AuPd sat), the STEM-HAADF image revealed that the chosen synthetic method (see Appendix B) yielded Au nanoparticles encapsulated by a Pd shell, confirmed by the EDS elemental map, as indicated in Figure 4.5E,F. The synthesis resulted in small Au NPs coated with a thin Pd shell due to the difference in their reduction potential. The size distributions of Pd sat and AuPd sat mean diameters were determined to be 5 nm ±

1 nm and 6 ± 1 nm, respectively, where the Pd shell represented approximately 1 nm of the AuPd sat. The size distributions are shown in Figure 4.5C,D.

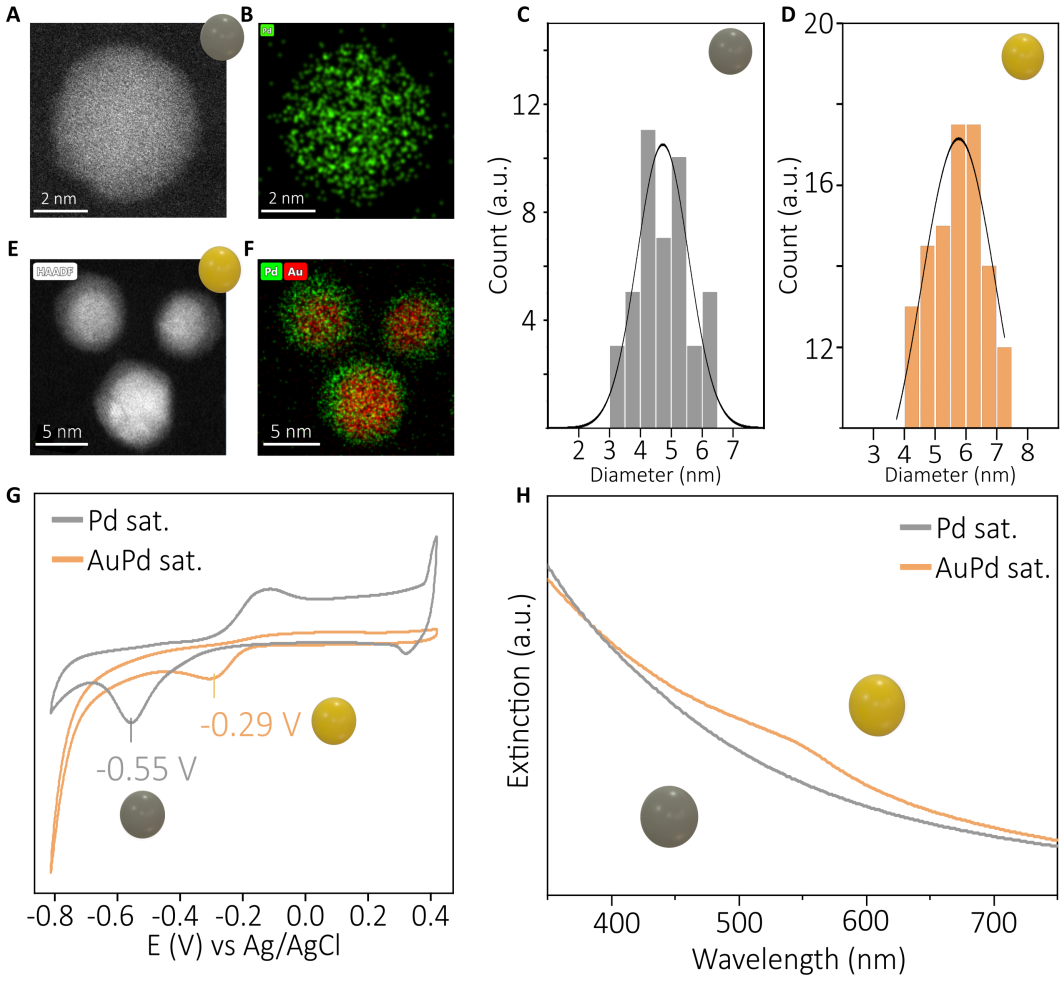

Figure 4.5: **Characterization of satellites NPs**. **(A,B)** STEM-HAADF images and EDS elemental map of a Pd NP used a satellite. **(C,D)** Size histograms of Pd indicating a size of ∼5 nm. The AuPd satellites were confirmed by HAADF-STEM ((**E**)) and EDX elemental maps **(F)** to be small Au nanoparticles encapsulated with a Pd shell, slightly larger (∼6 nm) in comparison with Pd satellites ((**D**)). CV of FTO-supported Pd and AuPd satellites in panel **(G)**. A shift is also observed for the AuPd satellite, as expected for core@shell nanoparticles. **(H)** While an increasing extinction with shorter wavelengths is observed for Pd satellites, AuPd satellites presented a shoulder, signature of sustaining LSPR.

As in an antenna-reactor system, the satellites form the reacting site, we also investigated them electrochemically. For the analysis, the satellites were dialized for 9 h, replacing the water every 3 h and were also supported on FTO and fixed with Nafion. Similarly, 30 cycles were recorded and the last ones are shown. The representative CV are plotted in Figure 4.5G. The pure Pd reduction curve displayed a clear peak at E=-0.55 V,

whereas the AuPd NPs displayed a peak at more positive reduction potentials E=-0.29 V, as expected for Au-Pd core-shell like nanoparticles [123]. This shift of Pd reduction peak ($PdO \rightarrow Pd^0$) is caused by changes in Pd electronic properties [86]. Finally, we used UV Vis spectroscopy to investigate their optical properties within the visible range. The Pd nanoparticles showed a typical Rayleigh scattering profile, where the scattered and absorbed light increase as the wavelength decreases. Likewise, the Au-Pd satellites presented a shoulder around 520 nm, which we identify as a the LSPR for the small Au NP, damped by the presence of the Pd shell. These results are shown in shown in Figure 4.5H.

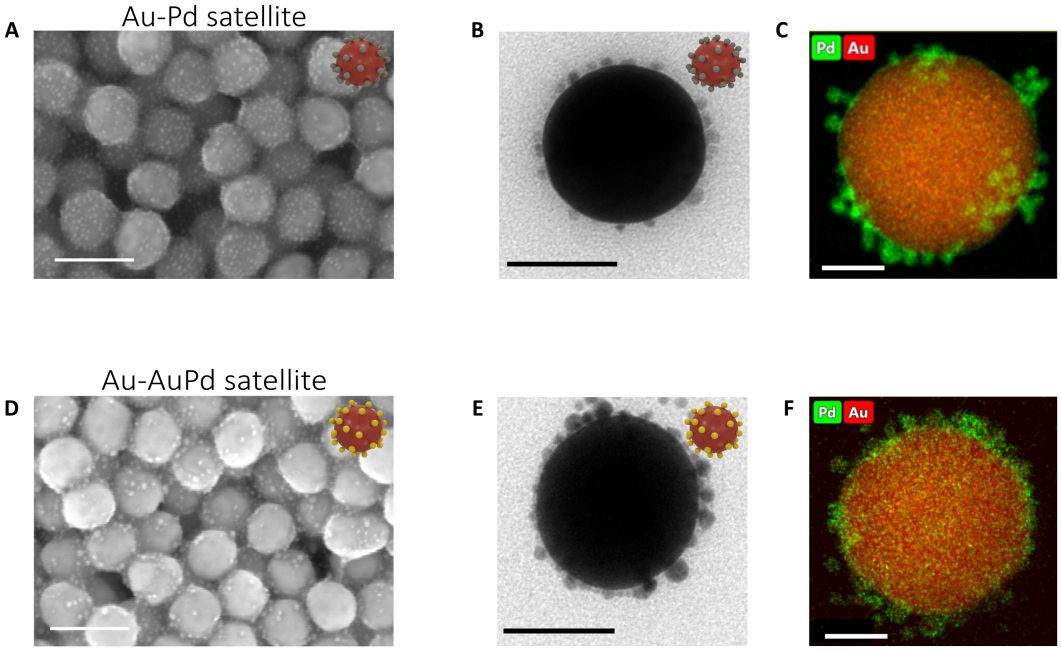

Figure 4.6: **Core-satellites characterization**. **(A)** SEM of Au-Pd core-satellites, confirming the distribution of satellites around the main core. Scale bar: 100 nm. **(B)** Representative Au-Pd core-satellite nanoparticle. **(C)** EDX elemental map in which Pd was only observed where the satellites are. **(D)** SEM of Au-AuPd core-satellites, confirming that AuPd where also around the main core. Scale bar: 100 nm. **(E)** Representative Au-AuPd core-satellite nanoparticle. The satellites appear darker due to the larger Au contrast. **(F)** EDX elemental map in which both Au and Pd were observed at the satellites position.

The assembly of satellites to the main core was conducted by manipulating the surface chemistry of the constituents. The fabricated AuNS were protected with the quaternary amine CTAB ($-NR_4^+$), which in order to provide stability locate at the Au surface in a double layer way. Likewise, the Pd satellites were synthesized with PVP as surfactant, which brings negative charges to the particles. Thus, the self-assembly of oppositely charged nanoparticles was achieved employing EtOH as a stimulus [95,108]. The EtOH would partially dissolve the CTAB bilayer and the remaining charges will strongly interact with the negatively charge Pd NPs, pulling constituents together and hence, yielding a core-satellites

nanostructure.

Figure 4.6A,D confirmed the presence of smaller particles (satellites) for each of the structures was confirmed via SEM, however this is not sufficient proof of the assembly, as it could be a mix of particles without any attachment. Electron microscopy confirmed the successful attachment of small Pd NPs to Au NS (Figure 4.6B. This structure was named as Au-Pd core-satellite. As expected, EDS analysis reveals the presence of Pd satellites (green spots, Figure 4.6C). Following the same methodology, AuPd satellites were also confirmed to be successfully assembled onto the surface of Au NS. Analogously, we named it Au-AuPd core-satellite. TEM images show darker satellites due to the larger contrast of Au (Figure 4.6E). Correspondingly, elemental mapping confirmed the presence of Au in both the core and the satellites, the latter coated by the thin Pd shell (Figure 4.6F. From in High-angle Annular Dark Field (STEM-HAADF) images and EDS maps, the satellite density was estimated to be approximately 50 Pd satellites per Au NS in both cases.

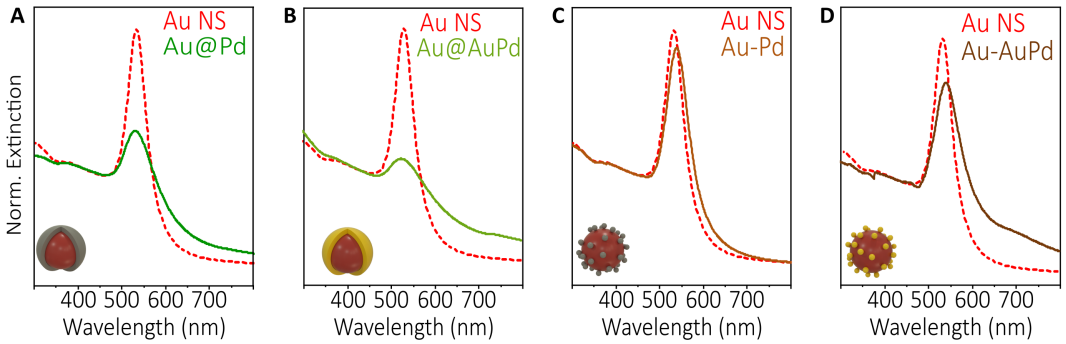

Figure 4.7: **Optical characterization of bimetallic nanocatalysts with different configurations**. **(A,B)** Extinction spectra of both Au@Pd and Au@AuPd core@shells, indicating the dampening of the LSPR upon intimate contact between the materials. Even small amounts of Pd leads to a strong dampening of the signal. **(C,D)** Extinction spectra of both Au-Pd and Au-AuPd core-satellites configurations. Both are red-shifted in comparison with AuNS LSPR. Au-AuPd appear to induce a larger damping of the LSPR, which can be attributed to the coupling between the AuNS and the AuNPs in the satellite. The bare AuNS spectra is represented by the red dashed line. Extinction spectra are normalized at 400 nm.

The four catalysts were also characterized optically with UV-Vis extinction spectroscopy (Figure 4.6)A-D). Both core-shell structures (Au@Pd and Au@AuPd) showed a typical broader and blue-shifted peak compared to bare Au NS (red dashed line) due to the presence of Pd in the shell, which is more lossy material than Au [79, 124]. The alloyed shell also showed a damped plasmon, as a very low amount of the catalytic metal strongly affects the decay pathway [79]. Concerning the Au-Pd core-satellite nanostructure, the plasmon resonance was red-shifted and broadened compared to signal of AuNS, as previously reported for this type of systems [125]. The red shift happens due to changes in the dielectric function in the near-environment of the plasmonic antenna. Finally, the same behavior was observed for the Au-AuPd core-satellite catalyst, although with a larger broadening than Au-Pd, which could be attributed to a broader size distribution. The well-defined reso-

nances of the hybrid structures evidenced the stability of the colloids in solution. A key requirement for our comparisons of photocatalytic activity is that the plasmon resonance fall within the same spectral range, 520-540 nm. This ensures that each catalyts shows a strong interaction with photons of the same energy range, but simultaneously points out that the geometry alters completely the decay pathways for captured light, and results in very different photocatalytic activity. Their optical behavior will be further discussed in the following sections.

4.1.4 Catalyst preparation

Ligand replacement Concerning the interface, as satellites are coated with polyvinylpyrrolidone (PVP), the capping of core-shell structures (CTAB) was replaced post-synthesis by dispersing them in a PVP ethanolic solution (See Section 3.1.2) [126]. It allowed us to control the interaction between the Pd surface and FA and diminish differences in our systems. The successful exchange was confirmed by ζ-potential measurements (Supplementary Figure 8). The stability in solution of all nanoparticles, as well as, their surface charge were monitored using Dynamic Light Scattering (DLS) measurements, via size and Zeta potential (ζ) determinations. The ligand exchange was confirmed by ζ-potential measurements (Figure 4.8). The bare Au NS presented a positive value due to the CTAB used as stabilizer. Moreover, the successful CTAB-to-PVP ligand exchange was evidenced by the negative value of both the Au@Pd and Au@AuPd core-shell structures. In addition, the values for the core-satellite configurations catalysts are shown.

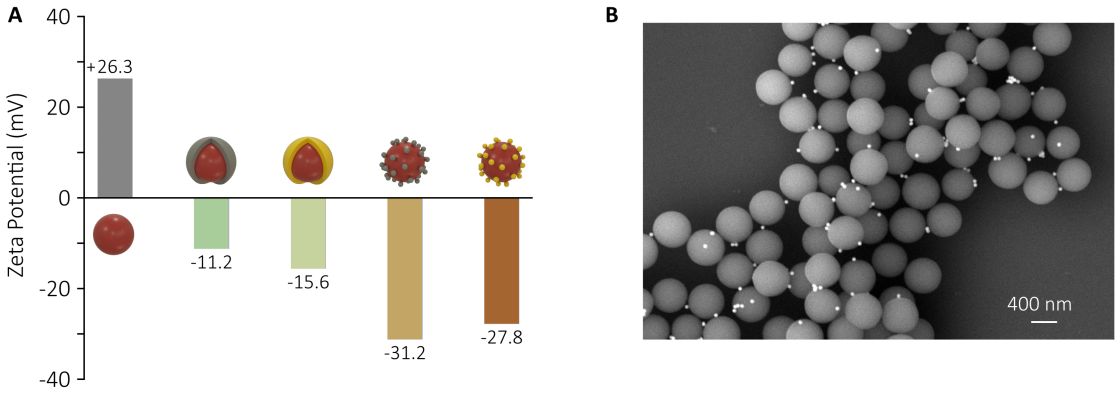

Figure 4.8: **Catalysts' preparation for photocatalytic tests**. **(A)** Surface charges adjustment in all catalysts. ζ-potential measurements confirmed the successful ligand exchange (CTAB to PVP). Additional values for PVP capped core satellites structures. **(B)** SEM image of SiO_2 supported nanocatalysts. The support was introduced to avoid uncontrolled aggregation and thus, changes in optical and thermal properties.

SiO_2 support It has been recently reported that hot spots formation, which can occur upon aggregation of the particles, has a remarkable influence in plasmonic photocatalysis [48]. Therefore, all the catalysts were supported on 600 nm SiO_2 spheres to avoid the

uncontrolled formation of clusters. Thus, the surface of SiO_2 templates, initially charged positively, were modified with PAH, a positively charged polymer. Upon mixing under sonication, the negatively charged catalysts were supported on the templates by electrostatic attraction (see Figure 4.8). The SiO_2-to-catalyst ratio was controlled to work with individual catalysts.

4.2 Plasmon-driven Formic Acid decomposition

To investigate which bimetallic configuration is the most efficient in converting light into chemical energy, we tested the bimetallic catalysts in FA decomposition after the thorough characterization. For the analysis, we will focus on the improved performance upon illumination, as opposed to the absolute catalytic performance of each configuration.

$$HCOOH \longleftrightarrow CO_2 + H_2 \ (\Delta G = \text{-}48.4 \text{ kJ mol}^{-1}) \tag{4.6}$$

$$HCOOH \longleftrightarrow H_2O + CO (\Delta G = \text{-}28.5 \text{ kJ mol}^{-1}) \tag{4.7}$$

It is well known that FA decomposition can follow two possible reaction pathways: dehydrogenation, yielding H_2 and carbon dioxide (CO_2), or dehydration forming carbon monoxide (CO) and water (H_2O) [81, 127]. The former is the most favored thermodynamically (Equation 4.6 and 4.7). Note that a little amount of CO can poison the catalyst due to it strong adsorption on Pd surfaces, inactivating the whole catalyst [128].

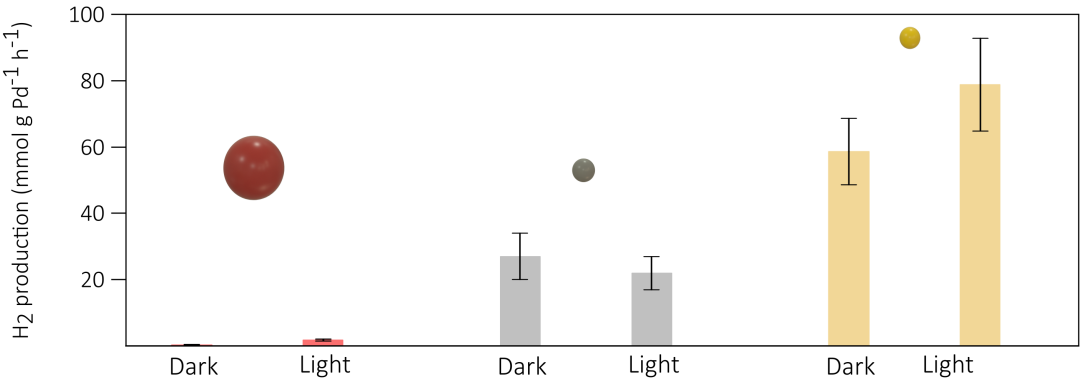

Figure 4.9: **Control experiments on plasmon-driven FA decomposition.** Production rate for Au NS (red), Pd (grey) and AuPd satellites (yellow), used as controls.

Herein, we performed the experiments in a closed reactor with a fine control of the temperature (T= 40.0 ± 0.5 °C) and equal FA concentration (0.5 M) in the absence of any additives. We aimed to work with both a similar number of Au NS (Section 4.1.1) and a similar interface (i.e. capping agents of the colloidal catalysts). As most of the FA

decomposition products are gases, a gas chromatograph (GC) equipped with a thermal conductivity detector (TCD) was employed to quantify the generated H_2 moles. The reaction rate were obtained by normalizing the produced H_2 moles by the amount of Pd present in each sample. Details of these calculations are provided in Section 3.7. To test the performance of these catalysts in a regime approaching practical applications, we used as light source a commercial solar simulator operated in AM1.5G mode as source of light (P=125 mW accross the visible range). To ensure reproducibility, the catalysis experiments were repeated at least 4 times each (each of 1 h duration). All these experimental conditions were taken into account to properly address the differences in light-into-chemical conversion efficiency.

Control experiments conducted employing Au NS as catalyst in both dark and light conditions showed a significantly lower H_2 generation rate (0.31 and 1.73 mmol g Au^{-1} h^{-1}, respectively), revealing the Au NS poor catalytic activity in FA decomposition (Figure 4.9). It should be clarified that uniquely for Au NS, the rate was normalized by the mass of Au present in the sample. Similar controls were also carried out for the particles employed as satellites. The monometallic Pd satellites produced 27 and 22 mmol g Pd^{-1} h^{-1}, whereas the bimetallic AuPd satellites produced 58 and 78 mmol g Pd^{-1} h^{-1} for dark and light tests, respectively. It is worth mentioning that CO was not detected throughout all the performed experiments. These results support the bimetallic synergy for energy conversion, where Au plays the light confining role and Pd acts as the active catalytic element.

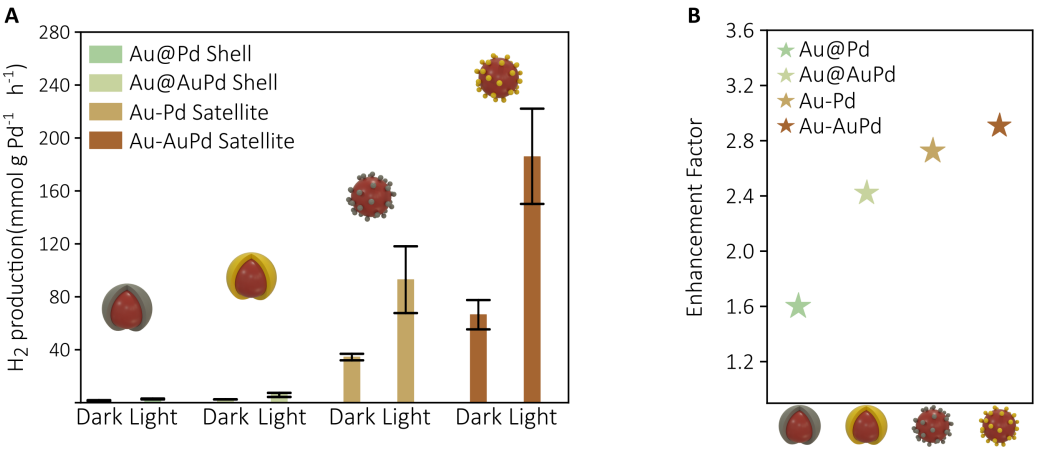

Figure 4.10: **Catalytic performances of bimetallic nanocatalysts in FA decomposition. (A)** Comparison of H_2 production in dark conditions and upon illumination with solar-simulator (power=125 mW). The number of Au NS antennas was estimated to be similar in all the experiments and the experiments were repeated at least 4 times. The FA concentration was 0.5 M in all cases. **(B)** Enhancement factors calculated in all cases as the ratio between light and dark performances.

The H_2 production rates in both dark and light conditions for each bimetallic nanocrystal are shown in Figure 4.10A. The influence of light on the catalytic activity is summarized

in the enhancement factor, that is the ratio between illuminated and dark performances. Core-shell systems showed considerably lower reaction rates in dark and upon illumination compared to the core-satellites structures. Nonetheless, the AuPd alloy shell showed a larger production than the monometallic Pd shell, as expected from the literature on the reactivity of Pd vs the AuPd alloy for this reaction [121]. Likewise, Au@AuPd core-shell also showed a larger enhancement of the light/dark performance (2.4-fold) in comparison with the Au@Pd (1.6-fold) (Figure 4.10B).

Core-satellites presented a larger production in both dark and light conditions than the core-shell catalysts. The influence of light was slightly higher for these structures, yielding larger enhancement factors when comparing the dark and illuminated cases, and raising the reaction rates 2.7-fold and 2.9-fold for Au-Pd and Au-AuPd systems, respectively. Among all the catalysts, both the largest production and enhancement were displayed by Au-AuPd core-satellites (191 mmol g Pd^{-1} h^{-1}). These results suggest that the two-body architectures are, in principle, the configuration that leads to a larger efficiency for light driven photocatalysis when employing hybrid plasmonic systems.

4.3 Enhancement mechanism

FA dehydrogenation is a redox reaction where charge transfers are involved [129]. Briefly, formate ($HCOO^-$, FA^-) adsorbs on Pd in a bridging mode, gets oxidized to CO_2 after C-H bond cleavage and releases one H atom, which is later combined with a second H to yield H_2 [81]. As in any chemical reaction, the temperature at the surface of the catalyst plays a major role in the reaction rate due to exponential temperature-dependence of the reaction rate, given by the Arrhenius equation. Besides an increase in temperature, the enhanced absorption of light enabled by the resonant plasmonic antenna can also benefit the catalytic reaction through the generation of hot carriers [66, 130]. There has been considerable debate in the recent literature trying to disentangle the two contributions, of heat and of hot carriers, and we therefore took additional steps to try and evaluate heating contributions. The photocatalysis tests were conducted with a precise control of the temperature, as mentioned above. Likewise, we took care of variables that could potentially mislead to a wrong interpretation. Among the experimental parameters, it is worth stressing that the hybrid catalysts were supported on SiO_2, which enabled us to work with well-separated catalysts avoiding heat accumulation [30] and the experiments were conducted in stirring conditions (400 rpm) that enabled to decrease any temperature gradient [131]. Further details of the experiments can be found in Section 3.7.

4.3.1 Evaluating thermal contribution

The reaction rates depend exponentially on the temperature ($k \propto \exp^{-E_a/k_B T}$, Equation 2.16), therefore we sought to quantify how much heat is delivered to the surroundings. First, we estimated how much the temperature increases due to the illumination for bare Au NS. Equation 2.17 assumes a linear dependence of the surface temperature with the

irradiance and has been utilized to successfully estimate the temperature of bare Au NS at a single wavelength. Barella et al. conducted a systematic study on temperature increase as a function of the irradiance for AuNPs with different sizes. Therefore, we can take advantage of their data and hypothetically estimate an upper-bound for the heat delivered by a single AuNS. This is quantification is possible because at 532 nm (green laser used in their study) our particles would be illuminated resonantly, meaning at their maximum of the LSPR, wavelength at which they present a larger interaction with the incoming light and in principle, larger absorption. Note that we took the precaution to work with individual particles by supporting them on SiO_2 sphere, ruling out collective heating effects. Thus, the temperature increase was estimated as follows:

$$T = T_0 + \beta \times I^{Exc} \tag{4.8}$$

where T_0 [K] refers to the temperature of the particle in the absence of light, I^{Exc} (mW cm^{-2}) is the irradiance and β is the photothermal coefficient [K μm^2 mW $^{-1}$]. Our photocatalytic experiments were performed with a fine control of the temperature using an external cryostat (313.15 K) and the irradiance was approximately 106 mW cm^{-2}. It is worth mentioning at this step that the irradiance was measured using a thermal detector, which is a perfect absorber within the utilized wavelength range. Thus, the reported irradiance corresponded to the total spectrum, implying that the power at the resonance was lower compared to the measured one. The photothermal coefficient of a 60 nm AuNS in H_2O is estimated to be 50 K μm^2 mW^{-1} from their size dependent photothermal coefficient plot [35]. Plugging the numbers in, the calculations retrieves that for a 60 nm Au NS in water and an irradiance of 106 mW cm^{-2}, the temperature is expected to increase only by 5.3×10^{-5} °C. As the second term in Equation 4.10 is five orders of magnitude smaller than the first for the used irradiance, it suggests that the enhancement on the reaction rate is not driven by thermal effects upon LSPR relaxation.

$$T = 313.15 \text{ K} + 50 \text{ K } \mu\text{m}^2 \text{ mW}^{-1} \times 106 \text{ mW cm}^{-2} \times \frac{1 \text{ cm}^2}{(10^4)^2 \mu m^2} \tag{4.9}$$

$$T = 313.15 \text{ K} + 5.3 \times 10^{-5} \text{ K} \approx 313.15 \text{ K} \tag{4.10}$$

The correct prediction on the order of magnitude for temperature contributions at such low irradiances are discussed with detail in Chapter 5, where a deep study of the ability to convert light into heat is presented for the structures used in these photocatalytic tests.

In a second step, we estimated how much the temperature should be raised to mimic the enhancement for each configuration considering only thermal effects (no light) and the activation barrier of FA dehydrogenation on Pd, Au and AuPd (46.6 kJ mol^{-1}, 53 kJ mol^{-1} and 28 kJ mol^{-1}, respectively). These calculations are presented from Equation 4.11 to Equation 4.14 and the results summarized in Table 4.2. While for Pd-FA interfaces, the temperature should increase 10 K, 21 K and 22 K if the enhancement factors are 1.6, 2.7 and 2.9 for Au@Pd core-shell and Au-Pd and Au-AuPd core-satellites, respectively, for Au-FA and AuPd alloy-FA interfaces the temperature should be increased by 34 K and 32

K to mimic the enhancement factors (5.6 and 2.4). There is no report of E_a on Au_1Pd_1 alloy. However, to roughly estimate the temperature increase, we take the value reported by Metin et al. for FA dehydrogenation on $Au_{0.41}Pd_{0.59}$ (28.25 kJ mol^{-1}), which is the example that resembles the most [132]. These crude estimations suggest that the heating coming from the excitation of individual optical antennas (Au NS) is negligible and cannot explain the observed speed up in the reaction rate when the structures are illuminated. Based on all the analysis detailed above, we interpreted the local heat generated upon illumination is not sufficient to explain the observed enhancement and consequently we focused our analysis on the generation of hot carriers.

$$k_1 = A \times \exp^{-E_a/k_B T_1} \tag{4.11}$$

$$k_2 = A \times \exp^{-E_a/k_B T_2} \tag{4.12}$$

If k_2=2.9 $\times$ k_1, is possible to derive a relationship between the two temperatures.

$$\ln \frac{k_1}{2.8 \times k_1} = \frac{-E_a}{k_B}(\frac{1}{T_1} - \frac{1}{T_2}) \tag{4.13}$$

$$\frac{1}{T_2} = \frac{k_B}{E_a} \times ln\frac{1}{2.9} + \frac{1}{T_1} \tag{4.14}$$

Catalyst	Energy Barrier [E_a, kJ mol^{-1}]	Enhacement Factor	ΔT (°C, K)
Au@Pd core-shell	46.6	1.6	10
Au@AuPd core-shell	28.25	2.4	32.6
Au-Pd core-satellite	46.6	2.7	21.9
Au-AuPd core-satellite	46.6	2.9	22.8
Au NS	53.0	5.59	34.8
Pd satellites	46.6	1.22	3.8
AuPd satellites	46.6	1.33	5.5

Table 4.2: Calculations of the temperature increase to mimic enhancements induced by light in catalysts and respective precursors utilized as controls

4.3.2 Hot carriers evaluation

The absorption of light in a metal such as Pd can lead to a rapid dissipation in the form of direct d-to-s transitions. The presence of a supporting Au antenna can substantially enhance this process through the amplification of the electric field in the Pd region [48, 133, 134]. Crucially, we noted differences observed in the extinction spectra of the hybrid catalysts (Figure 4.7A-D), implying that the absorption in the catalytic active metal can be dependent on the spatial arrangement of the materials. Additionally,

the strong inhomogeneous near-field around the satellite particle is expected to boost the generation of hot carriers at the catalyst surface, where they speed up the reaction rate.

To evaluate these differences, we investigated both the electric field intensity and the absorption profiles for each hybrid nanostructure. The geometrical models used in the optical simulations were built up based on the experimental information obtained in their characterization. Figure 4.11 summarizes our efforts to understand how bimetallic catalysts interact with the incoming light and how this may lead to the generation of highly energetic carriers [135]. For comparison, the spatial distribution of the near-field at their plasmon resonance is shown for both Au@Pd core-shell (Figure 4.11A) and Au-Pd core-satellite configurations (Figure 4.11B). As the satellites consist of either Pd or Au and Pd, Figures 4.11C and 4.11D show the electric field intensity of a single satellite placed 1 nm away of the 60 nm Au NS antenna. As expected, the electric field at the interparticle gap of a Au-Pd core-satellite structure is approximately 30 times larger than the electric field at the surface of Au@Pd core-shell. This is attributed to the small interparticle gap between the two metallic entities, which leads to a hotspot. A non-appreciable difference was observed for mono- and bimetallic satellites, suggesting that the electric field enhancement at the hotspot is not strongly modified by composition of the satellites for that particular size (∼5 nm).

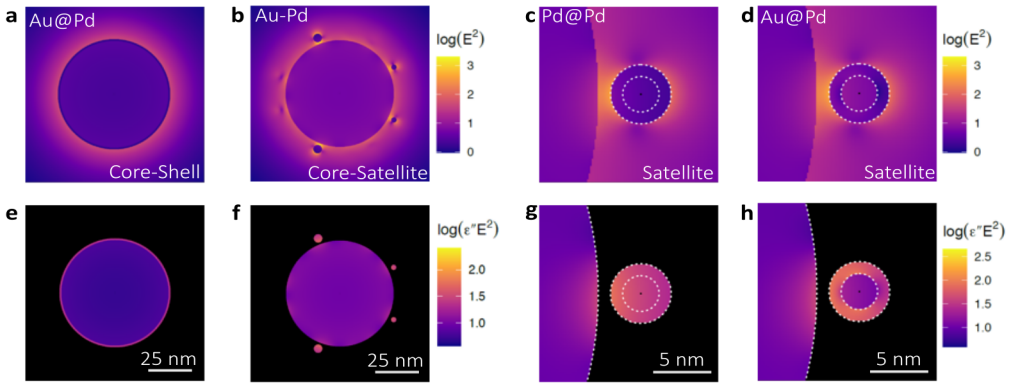

Figure 4.11: **Electric field intensity and absorption maps for bimetallic catalysts.** Local field intensity enhancement factor ($|\mathbf{E}|^2$, with unit incident field)for Au@Pd in both core-shell **(A)** and core-satellites **(B)** configuration. Electric field intensity maps for a Pd satellite **(C)** and AuPd satellite **(D)** placed 1 nm away from a a 60 nm Au core. Complementary absorption maps of Au@Pd core-shell **(E)** and core-satellites **(F)**. Absorption maps for a full Pd satellite **(G)** and AuPd satellite **(H)** placed at 1 nm away from a 60 nm Au core. In each case the electric field intensity is averaged over incident directions and polarisations.

In order to better understand the hot carriers generation within Pd, we also mapped the local rate of absorption, which is proportional to the local field intensity times the imaginary part of the dielectric function in each material region [31, 48], as detailed in Equation 2.18. These maps reveal that light is better confined within the Pd satellites

than in the 1 nm shell of the core-shell structure, leading to at least a five times larger local absorption rate (Figure 4.11e,f). For satellites with different composition there is a striking difference. Interestingly, the strongly localized local absorption in the thin Pd shell of the AuPd satellite is higher than in the monometallic Pd satellite (Figure 4.11g,h). This greater absorption is attributed to the fact that the catalytic metal is placed in between two coupled Au optical antennas. In line with what has already been reported, placing a nonplasmonic metal at the hotspot between two optical antennas, leads to highly confined enhanced absorptions [48]. Indeed, this intense electric field region can account for up to 50% of the hot carriers generation rate [29], what is beneficial for redox processes as a high carriers density is concentrated in such small spatial region.

Our simulations suggest that core-satellites are more efficient than core-shell structures in funneling the energy from the plasmonic to the catalytic metal. The highly confined and inhomogeneous electric field in the interparticle gap between the core and the satellites, leads to a larger local absorption rate at the surface and therefore a larger local hot carriers generation rate within Pd. Thus, we hypothesize that at the resonance, the hot electrons and the hot holes created in Pd are energetic enough, and present at the surface where the chemical reaction takes place, assisting both the reduction of adsorbed H atoms and the C-H cleavage bond of the FA^-, which is thought to be the rate limiting step of the oxidation reaction [129].

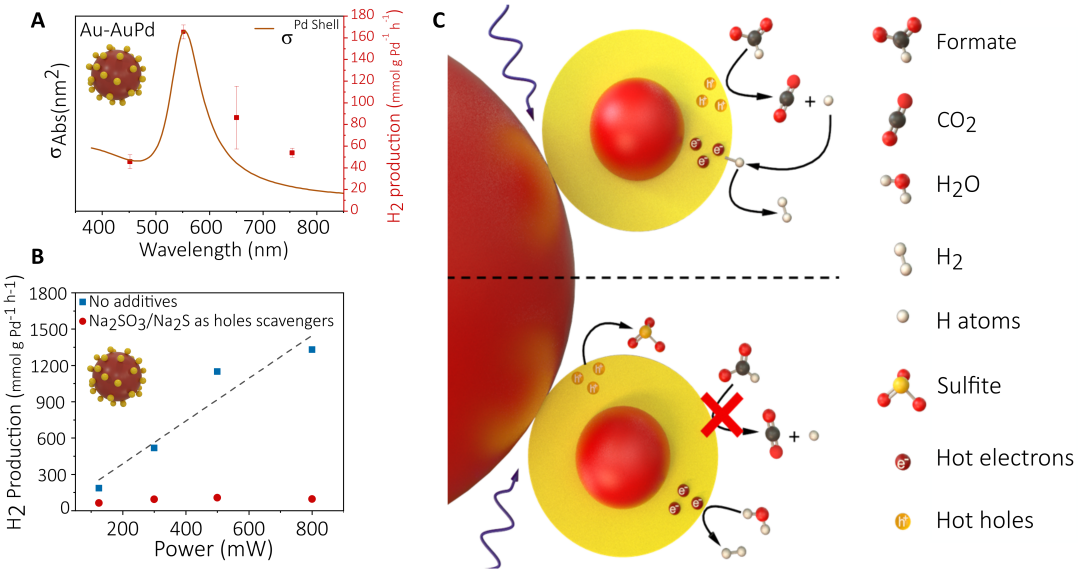

Figure 4.12: **Study of the reaction mechanism. (A)** Wavelength dependent H_2 production simultaneously plotted with Pd absorption cross-section of Au-AuPd core-satellite nanocatalyst. **(B)** Power dependent experiments for Au-AuPd core-satellites in the presence and absence of hole scavengers in the reaction mixture. **(C)** Proposed mechanism of the reaction in the presence and absence of holes scavenger.

To test this hypothesis, we conducted wavelength and power dependent FA decomposition experiments on Au-AuPd core-satellite, which turned out to be the more sensitive to

light exposure (larger enhancement factor). For the wavelength dependence, a broadband lamp equipped with bandpass filters of 20 nm width centered at 450, 550, 650 and 750 nm were used. The lamp was additionally equipped with an IR liquid filter to eliminate alternative sources of heat such as water absorption, and with a 400 nm longpass filter to eliminate the UV contribution. The measured power for the aforementioned ranges was 20 mW. We present in Figure 4a the wavelength dependent H_2 production rate. Additionally, as a proxy for the concentration of hot carriers, which remains challenging to calculate in such non-trivial geometries, we also plot in Figure 4.12A the theoretical spectrum of light absorption in the Pd region of the AuPd satellite. We note a good correlation in the two spectral profiles, especially with the sharp drop of the H_2 production rate obtained when illuminating with blue light (450±10 nm). The long-wavelength tail shows poorer agreement, but this could be explained by the sample inhomogeneity (particle size and gaps); the model considers a single perfectly spherical pair of antenna-satellite, and the sample's UV-Vis characterization already shows a long-wavelength tail (Figure 4.7). Based on the optical simulations, without the highly confined electric fields, energetic carriers would not be generated within the Pd shell and the reaction could not be sped up, as also shown when the sample is illuminated off-resonance [136,137]. The obtained production using the lamp is comparable to what has been obtained using a solar simulator, as described next.

Another critical measurement to assess the contribution of the absorbed light on the reaction rate is to vary the illumination power (Figure 4.12C). For this, we used a broadband source equipped with the same IR and UV filters. The experiments were conducted without and with hole scavengers ([$NaSO_3$]= 1 mM,[Na_2S]= 1 mM) [75,138]. The nature of the additives enables to solely quantify the H_2 generated out of FA. While no additives were added, a linear trend was observed with the increasing power, reaching up to 1331 H_2 mmoles g Pd^{-1} h^{-1} when illuminating at 800 mW. However, a remarkable decrease in the activity of the catalyst was observed at all powers in the presence of hole scavengers. This experiment confirms the crucial role of both electrons and holes in the reaction, supporting the minor heat contribution. If FA dehydrogenation would have been activated by thermal energy, the reaction rate should have increased with the increasing power when the experiment is performed in the presence of both $NaSO_3$ and Na_2S.

This combination of results leads us to the propose that Pd partial absorption is enhanced when placed in a hotspot between two Au coupled antennas, yielding electrons and holes with sufficient energy to assist the FA dehydrogenation (Figure 4.12B, upper part). In the presence of a hole scavenger, the holes are partially consumed and, consequently, FA^- is not oxidized to CO_2 (Figure 4.12c, bottom part). As a result, a second H atom is not released and H_2 production is reduced [139,140]. To restore neutrality in the catalyst, we hypothesize that the excited electron can either reduce the adsorbed H atoms coming from FA acidic dissociation or H_2O molecules [141].

4.3.3 Apparent Quantum Efficiency

An important parameter in photocatalysis is the Apparent Quantum Efficiency (AQE), what accounts for how many photoexcited electrons were converted into molecules per

incident photon [69, 83, 142]. The estimated values for our catalysts are shown in Figure 4.13A , as well as the energy absorbed by Pd in all the structures. To estimate this captured power (absorption) over the visible range, we integrated the product of the solar simulator spectrum and the Pd partial absorption from 400 nm to 800 nm . This total absorbed energy was then normalized by Pd mass.

Both the AQE and Pd partial absorption show a dependence on the configuration of the nanoparticle. While the values estimated for Au@Pd, Au@AuPd and Au-Pd were similar (ranging between 0.08-0.15%), the AQE of Au-AuPd core-satellite was estimated to be 0.28%. This improved AQE was a result of the maximized absorption on the catalytic active metal, as the Au-AuPd structure showed the largest absorption in Pd among all the configurations. These results reinforces the relevance of the geometry on photocatalytic processes. Specifically, the creation of optical hotspots can be converted into chemical hotspots when the active material is placed in such regions of intense and inhomogeneous electric field intensity, maximizing the solar-to-chemical energy conversion capabilities of bimetallic hybrid nanocatalysts. Although these reported values are a lower bound, as we are neglecting optical losses such as scattering, our results demonstrate at least a 3.5 times improvement in AQE when comparing with past reports for similar systems [143].

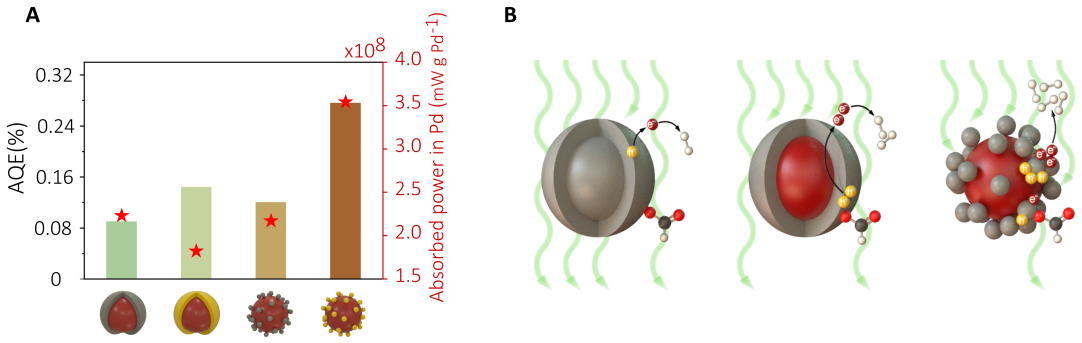

Figure 4.13: **Apparent Quantum Efficiency and power absorbed by Pd (A)** Comparison between the apparent quantum efficiency (AQE) and energy stored on Pd for each structure. The captured power was estimated from electromagnetic simulations, while AQE was esimated at the maximum of the extinction spectra. **(B)** Scheme of Pd partial absorption for different geometries. The presence of hotspots in core-satellite structures leads to a greater local Pd absorption.

We summarize the interpretation of our interpretation of the results in the scheme presented in Figure 4.13B. A pure Pd NP of ∼5 nm has a very small optical cross-section within the visible range and its catalytic activity relies on its inherent electronic properties. However, when a thin Pd layer (∼1-2 nm) is deposited on an optical antenna, the absorption at the shell is enhanced due to the higher intensity of the electric field. As a result, high energy carriers are created in the active metal, thus speeding up chemical reactions. This phenomenon can be further enhanced by engineering the metals in a two-body structure such as core-satellites. The interaction between two metallic nanoparticles leads to the creation of highly confined electric field regions (optical hotspots) and, consequently, a

larger local absorption within the Pd. This results in a larger number of excited carriers and therefore better photocatalytic performances.

Finally, we propose further hybrid nanostructures that can be promising for photocatalysis applications. In such structures a thin shell of either Pd or Au_1Pd_1 (1 nm in thickness) is placed between a 60 nm Au NS and 50 Au satellites of 5 nm in radius. Details of the structures and the calculations is provided in Supplementary Section 10. Through optical simulations, we observed that the absorption cross-section does not get significantly boosted with the presence of Au satellites. Nevertheless, the presence of smaller antennas determines the formation of numerous hotpots, what we have shown that is crucial for hot carriers generation. The optical phenomena dictating the behavior of such hybrid catalysts can be transferred to earth abundant metals such as Cu or Al, preserving the benefits of both the hotspots formation and the catalytic active centers and thus, lowering the overall price of photocatalyst.

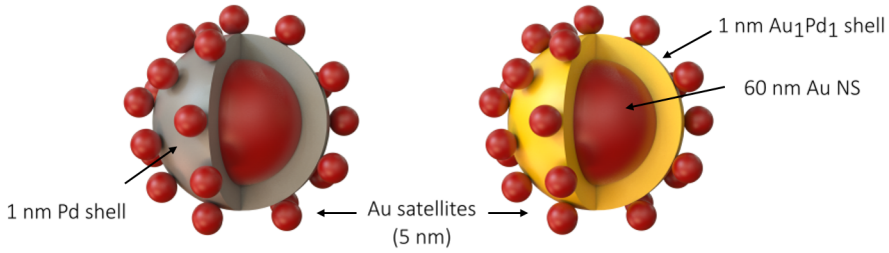

Figure 4.14: **Scheme of the proposed hybrid structures.** Hybrid structures in sandwich configuration in which either a Pd or a AuPd alloyed shell is placed between a 60 nm Au NS and 50 Au satellites with 5 nm in diameter.

4.4 Conclusions

The structure-dependent reactivity of bimetallic nanocatalyst was a central missing piece of the field to be clarified. Our results can now be employed a design rules for the next generation of catalysts, which will undoubtedly lead to a better exploitation of the constituents. We demonstrate that Core-satellite (Antenna-Reactor) systems present larger enhancements on the reaction rate compared to core-shell and alloys ones under illumination. The ability to create hotspots strongly influences the energy flow. Our optical simulations indicate that the strongly confined electric field at the interparticle gap between core and satellites leads at least a five-fold higher local absorption within Pd -catalytic active metal-. This enhanced local absorption was manifested as a 30% improvement in the apparent quantum efficiency. Engineering the photocatalyst in a way that the catalytic active metal is placed in the hotspot formed by two optical antennas, further improves its performance. Indeed, this system presented both the largest enhancement factor and apparent quantum efficiency (0.28%).

Energising the catalytic component of these hybrid materials by increasing local absorption can promote the generation of excited carriers in these typically weakly absorbing materials. Remarkable, the enhanced absorption can be achieved at solar conditions with the help of the plasmonic counterpart. We envision that plasmonic architectures that maximize the confinement of the nanoscale electric field in the catalytic material will further benefit sunlight into chemical energy conversion processes. Based on our results, colloids with internal hot spots, as well as large-scale metasurfaces and hybrid oligomers, among others, could become key players in the development of the field. Thus, these hybrid plasmonic materials fill the gap of a fundamental prerequisite in the efficient transduction of energy from sunlight to chemistry, which is dealing with solar spectra and irradiances. Towards more sustainable photocatalysis, we strongly believe that the enhanced local absorption on catalytic metals can be driven by earth abundant metals, such as Al or Cu. Similarly, these materials present resonances within the visible and can achieve a comparable electric field confinement [144, 145].

Chapter 5

Photothermal properties of bimetallic nanocatalysts

A systematic comparison of binary structures, which exhibit varying reactivity depending on the spatial distribution and interaction of the components, was presented in Chapter 4. In such study, the an estimation of the heat contribution was conducted by how much would be the temperature rise in an isolated AuNS when illuminated on resonance at the experiments' irradiance and compare it with the temperature needed to obtain the same light-enhancement only by pure thermal contribution. This comparison allowed us to conclude that heat appears not to be the main factor enhancing the reaction rate on H_2 generation. Nevertheless, there are two aspects to consider which play an important role on light-to-heat conversion in these structures. The first is related to the changes in the overall optical properties in the presence of the plasmonic component [80], while the second is the conduction of the harvested energy towards the catalytic surfaces, which can be strongly affected, for instance, by a large interfacial thermal resistance [146, 147, 148]. As the temperature at the catalytic surfaces is what a molecule would experience when undergoing chemical reactions, it is therefore necessary to determine it accurately. A reliable assessment of the temperature will help to disentangle the underlying mechanisms of reaction rate enhancements [63, 64, 149, 150]. Here, we used hyperspectral Anti-Stokes (AS) thermometry to determine the opto-thermal properties of bimetallic structures [35, 151]. AS thermometry exploits the fact that, upon illumination with a CW laser, the AS part of the photoluminescence (PL) spectrum of plasmonic NPs shows a temperature dependence. First, we assessed the role of the Pd shell at different thicknesses in Au@Pd CS-NPs, designed to investigate changes in their on-resonance photothermal response using AuNS as benchmark. The experimental studies are complemented with an analytical model for the photothermal response of CS-NPs. Last, the effect of the geometric configuration of bimetallic plasmonic NPs is assessed.

5.1 Characterization of Au@Pd Core@Shell Nanoparticles

Bare AuNS and Au@Pd CS-NPs with two different thicknesses were synthesized to evaluate how the presence of a Pd shell and its thickness affects the optothermal properties of the binary sample. Figure 5.1A illustrates the samples used in this first part of the study, which were prepared following the synthetic route employed in the past project. They consist of bare AuNS, and Au@Pd CS-NPs with two different thicknesses, which obtained by varying the ratio of Au core and Pd salt. The three colloids are again stabilized in water by means of cetyltrimethylammonium bromide/chloride (CTAB/CTAC) capping, facilitating the comparison among themselves.

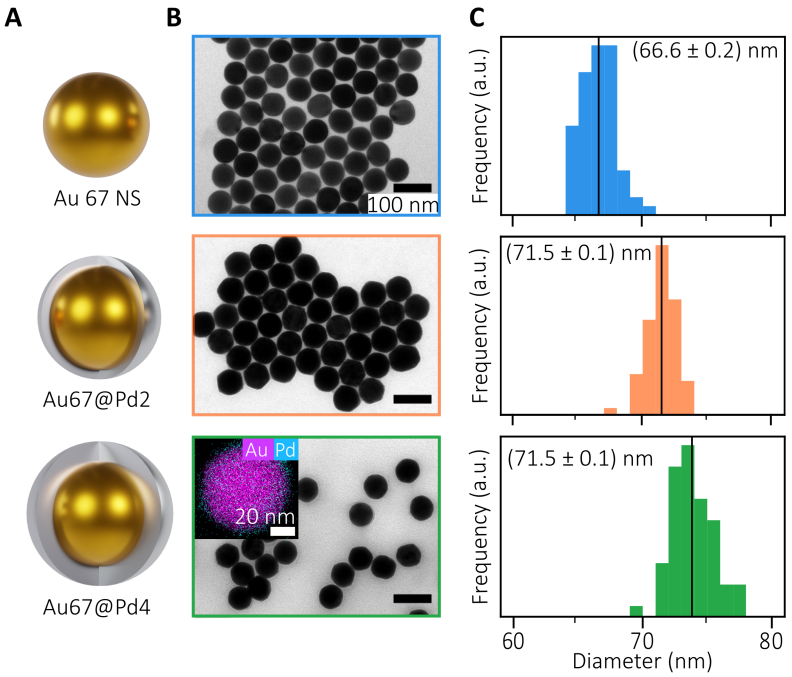

Figure 5.1: **Chemical and optical characterization of Au@Pd CS-NPs for photothermal response**. **(A)** Sketches of NPs used to conduct the study **(B)** TEM images of the three different studied NPs. Scale bars: 100 nm. The inset shows an EDX with the spatial distribution of the two metals. Au is shown in magenta and Pd in cyan. **(C)** Size distributions. Mean sizes are indicated with a black line and displayed in the labels.

To gain structural information of them, all samples were imaged using TEM (5.1B). Au NSs are confirmed to be spherical, while both Au@Pd appeared to be slightly more faceted. We again took advantage of Energy Dispersive X-Ray Spectroscopy (EDX) to confirm the spatial distribution of the materials, confirming the absence of Pd in the monometallic AuNS and its presence at the very edge of the Au@Pd configuration. The

presence of uniform Pd all around the core is an indication of an homogeneous coverage. A representative nanoparticle is shown as inset at the bottom of 5.1B, in which Au is depicted in magenta, while Pd in cyan. A size distribution analysis was conducted from the TEM images and the resulting particle size histograms were are shown in Figure 5.1C. This enabled us to gain insight on the thicknesses of the deposited Pd shells. The mean diameter of the Au NS turned out to be 66.6 ± 1.3 nm, while the two CS-NPs colloids have mean sizes of 71.5 ± 1.2 nm and 73.8 ± 1.7 nm. These values correspond to Pd thicknesses of approximately 2.5 and 3.6 nm, calculated by substracting the mean AuNS diameter to the mean diameter of the core@shells. For simplicity, from now on the samples will be named Au67, Au67@Pd2 and Au67@Pd4.

The synthesized samples were also studied using ICP-AES, technique that allowed to determine the metallic loads in each sample and thus, confirm the deposition of Pd shells with different thicknesses by estimating the Pd-to-Au ratio in each bimetallic sample. Table 5.1 shows the quantified Au and Pd loads in each structure. These experimental results were complemented with a theoretical approximation of the expected Pd-to-Au ratio for CS-NPs with dimensions according to what was obtained ones via TEM imaging. Equations 5.1 and 5.2 show the formulae employed for the calculation.

Catalyst	Au total (ppm)	Pd total (ppm)	Pd-to-Au ratio	Calculated Pd-to-Au ratio
Au67@Pd2	2.31	0.24	0.10	0.13
Au67@Pd4	2.92	0.61	0.20	0.21

Table 5.1: ICP-AES analysis used to determine Pd-to-Au ratio for Au@Pd CS-NPs with different shell thicknesses.

$$\text{Mass of Au sphere} = V_{Sphere} \times \rho^{Au} = \frac{4\pi}{3} r^3 \times \rho^{Au} \tag{5.1}$$

$$\text{Mass of Pd shell} = V_{\text{Pd shell}} \times \rho^{Pd} = \frac{4\pi}{3} (r^3_{\text{Au@Pd}} - r^3_{\text{67nm AuNS}}) \times \rho^{Pd} \tag{5.2}$$

The values used to estimate the Pd-to-Au ratio were ρ^{Au}= 1.93×10^{-20} g nm^{-3}, ρ^{Pd}= 1.2×10^{-20} g nm^{-3}, r$_{Aucore}$=33.3 nm, and r$_{Au@Pd}$= 35.75 and 36.9 for Au67@Pd2 and Au67@Pd4, respectively. The obtained ratios are also presented in Table 5.1, showing the similarities between the experimental and calculated values.

The interaction between the three systems and electromagnetic fields was simulated utilizing the obtained structural information to model individual NPs. As the sole source of heat originates from the absorption of the NPs, Figure 5.2A shows the numerically calculated absorption cross section spectra. As expected, the deposition of a thin Pd shell leads to significant damping of the LSPR of the Au core, reducing its amplitude and broadening its bandwidth. In addition, a small blue shift of the resonant frequency is predicted. Nevertheless, when acquiring the extinction spectra of the samples, a red-shift was observed instead. Figure 5.2B shows the normalized experimental extinction spectra

of the three synthesized colloids. The predicted broadening of the resonances due to the Pd shell is clearly observed, however, instead of a blue shift, the spectra exhibit slightly red-shifted resonances. The LSPR not only depend on the damping constants, but also on the near-environment (Equation 2.14). Due to the re-suspension of the NPs in an excessive amount of CTAC (20 mM), we believe that the slight blue-shift caused by the increased damping, was neutralized by the red-shift introduced by changed in the near environment [152]. We will account for this effect when assessing the thermal properties.

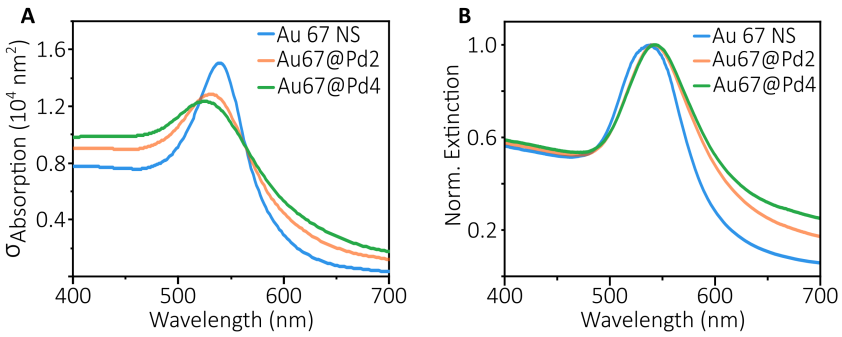

Figure 5.2: **Optical characterization of Au@Pd CS-NPs for photothermal response. (A)** Calculated absorption cross sections in water. **(B)** Experimental extinction spectra of the colloids. Each spectrum is normalized using its own maximum. In all figures, blue, orange and green correspond to Au67 NS, Au67@Pd2, and Au67@Pd4, respectively.

5.1.1 Single-particle analysis

Assuring that the analysis is carried out at the single-particle level is crucial in order to properly assess the photothermal response of bimetallic NPs and thus, rule out the coupling among NPs or collective heating effects that can mislead to wrong conclusions in this evaluation. Therefore, we took advantage of the charged ligand to achieve such single-particle regime. Arrays of well-separated individual NPs were thereby fabricated by transferring the colloidal NPs on glass substrates using optical printing, as schematically shown in Figure 5.3A. Dark-field images of representative examples of the optically printed grids are also displayed in Figure 5.3A. The optical printing, is a process where particles diffusing randomly (brownian motion) in solution are pulled towards a substrate due to the optical force applied by a laser [153, 154]. In this approach, the laser is tuned to match the LSPR of the particle ensuring a large interaction between light and particle. Also, the power of the laser should be in a range in which a threshold to drive the printing is overcome, but should not be large enough to trigger morphological changes due to elevated temperatures [153]. The power to print 67 nm AuNS was set to 8 mW μm^{-2}, whilst for the Au67@Pd CS-NPs, the irradiance was set to 6 mW μm^{-2}. Further details are provided in Chapter 3.

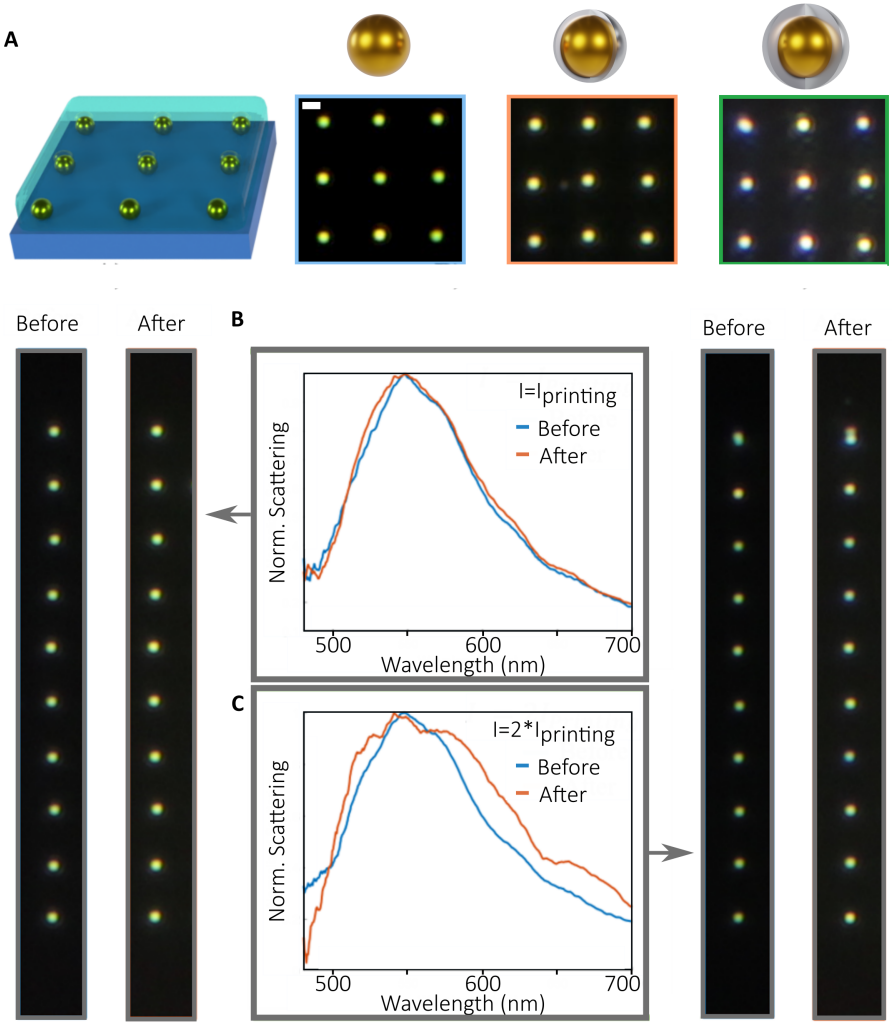

Figure 5.3: **Optically printed grids**. **(A)** Sketch of the samples used for photothermal characterization. It shows optically printed NPs on glass, surrounded by H_2O. Additionally, a 3×3 portion of the obtained grids are shown for each of the samples used in this study. **(B)** Normalized single-particle scattering spectra of Au67@Pd2 used for photothermal characterization. The spectra were obtained before illuminating the particles on resonance with the printing irradiance (6 mW μm^{-2}) for 2 minutes. No changes are observed in the profile, as also indicated in the DF image. **(C)** Normalized single-particle scattering spectra of Au67@Pd2 obtained before and after exposing the particles to an on-resonance illumination with twice the printing irradiance for 2 min. Visible changes are observed in the shape of the signal, suggesting morphological changes.

The stability of the NPs through the printing process was tested by illuminating a set of NPs at I =$I_{Printing}$ and I = 2 ×$I_{Printing}$ for 2 minutes. It is worth mentioning that the exposure time was far exceeding the printing time, which is typically below 1 s. In addition, the used irradiances were also larger than the ones employed later for photothermal characterizations, therefore, the chosen parameter would enable to gain insight on the morphological stability of the printed particles. As a metric to this end, we compared the

scattering spectra of a set of 10 NP before and after irradiation at two different powers. Figure 5.3B shows the obtained averaged scattering spectrum (N=10) of Au67@Pd2 before and after illumination for 2 minutes at printing irradiances (I =$I_{Printing}$). There are no signatures or indication on the average response, scattering spectra is mostly unchanged, indicating that the CS-NPs are stable under this irradiance. This can also be infere from the DF images on the left of Figure 5.3. Similarly, Figure 5.3C displays the averaged scattering spectrum of another set of 10 CS-NPs, but this time irradiated with an irradiance corresponding to twice the printing one. It is possible to observe that at this conditions, the scattering spectra already shows notable changes, as also evidenced by both dark field images. So, due to the reduced time in optical printing and the lower irradiances used in future photothermal studies, it is possible to conclude that the NPs under study survived the printing process and are representative of their initial colloidal suspension.

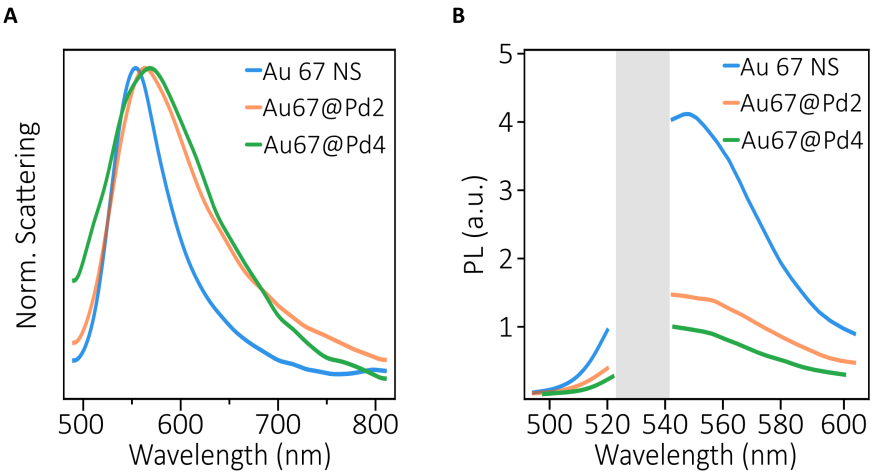

Figure 5.4: **Single-particle optical characetrization**. **(A)** Normalized scattering spectra of Au67, Au67@Pd2 and Au67@Pd4. The scattering of the bimetallic structures is red-shifted with respect to the Au67 signal. **(B)** Photoluminescence of the three samples. A pronounced drop is observed with the deposition of a Pd shell onto the Au67 cores, which is even more pronounced with thicker shells.

Once transferred to the substrates, the next step involved the study of the emission properties of all systems. This step was necessary because the detection of photoluminescence (PL) and the posterior data treatment is what enables to quantify the temperature raise as a function of the irradiance using on-resonance illumination, as described in Chapter 3. Figure 5.4A shows representative averaged and normalized scattering spectra for each type of NP. Both CS-NPs present a red-shift and a broadening of their resonance with respect to the Au67 cores, spectral feature that was also observed with the extinction (Figure 5.1). When evaluating the PL of the samples, a systematic decrease was observed with the increasing thickness of the Pd shell. Figure 5.4B presents PL spectra of the all-types of NPs, excited with CW laser excitation at 532 nm (Irradiance of 2.8 mW μm^{-2}). This wavelength was suitably chosen because it suits to excite the plasmon resonance of the

set. The PL profile of Au67, Au67@Pd2 and Au@Pd4 are shown in blue, orange and green, respectively. The grey area correspond to the PL which was filtered out from the acquisition. There are clearly two regions in the profile. The first one includes photons emitted at longer wavelengths (less energetic photons), which is referred to as Stokes section, while the second involves the emission of more energetic photons (shorter wavelengths), known as Anti-Stokes spectral region. The latter is the ones used to determine the photothermal response. It is clear that the sole inclusion of a thin layer of Pd (∼2 nm) leads to a significant drop in the amplitude of overall PL intensity, which could be attributed to both, the plasmon damping and the fact that now there is a new dissipation chanel that involves the injection of charges into the Pd shell [79]. The drop is even larger when the thickness of the Pd shell is enlarged from 2 to 4 nm.

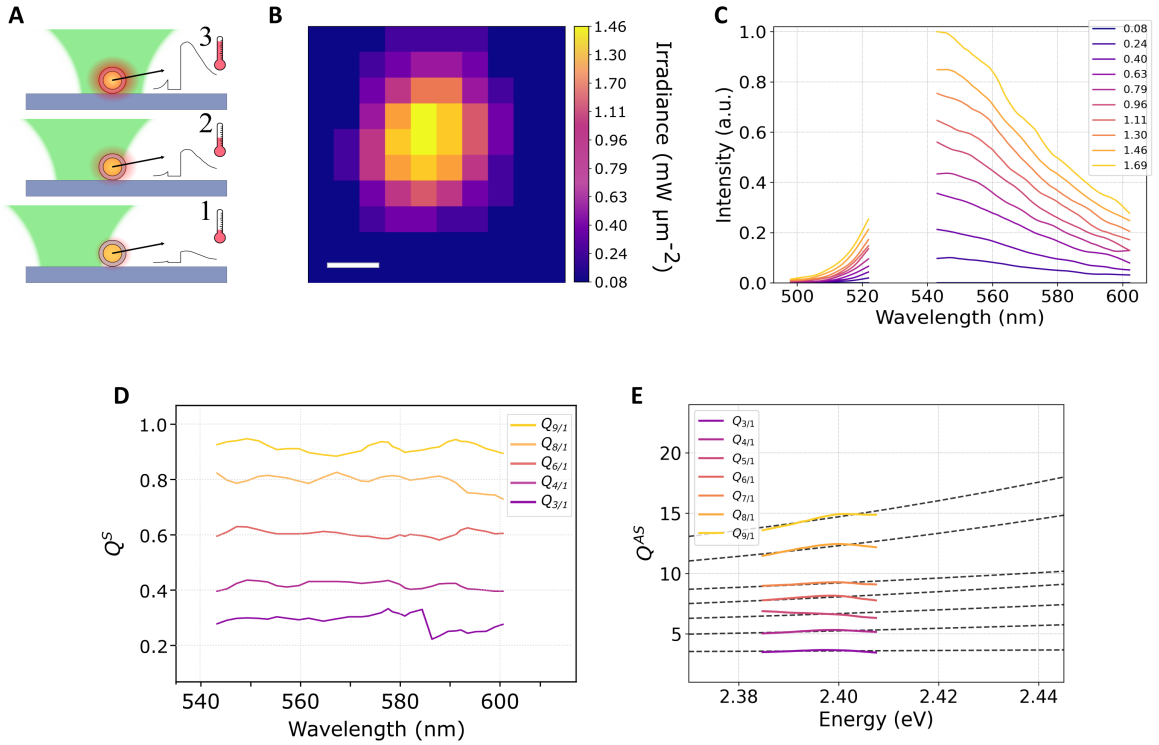

Figure 5.5: **Anti-Stokes thermometry**. **(A,B)** Extinction spectra of both Au@Pd and Au@AuPd core@shells, indicating the dampening of the LSPR upon intimate contact between the materials. Even small amounts of Pd leads to a strong dampening of the signal. **(C,D)** Extinction spectra of both Au-Pd and Au-AuPd core-satellites configurations. Both are red-shifted in comparison with AuNS LSPR. Au-AuPd appear to induce a larger damping of the LSPR, which can be attributed to the coupling between the AuNS and the AuNPs in the satellite. The bare AuNS spectra is represented by the red dashed line. Extinction spectra are normalized at 400 nm.

5.2 Photothermal response of Au@Pd Core@Shell NPs

Once confirmed that the NPs survived the printing process without alteration of its constitution, and that there is still remaining PL from the NPs after being coated with Pd, we proceeded to determine the photothermal response by employing Anti-Stokes thermometry. The technique allows single particle photothermal characterization by raster scanning a laser over the NP, as schematized in Figure 5.5A, thus heating and PL excitation are simultaneously performed with a single beam. Throughout the scanning, the relative position between the beam and the NP changes, leading to different excitation irradiances and hence, different steady state temperatures. The edge-to-edge navigation of the laser over a Au67@Pd2 Core@Shell NP is illustrated as a bin map in Figure 5.5B, where each of the bins corresponds to different irradiances and therefore, temperature. The PL spectra collected by illuminating with a green laser (λ= 532 nm) at different irradiances is presented in Figure 5.5C, color coded following panel B. The ratio of Stokes (Q^S) and Anti-stokes (Q^{AS}) intensities as a function of the wavelength are shown in Figures 5.5D and 5.5E. As expected, the ratio between the PL Stokes intensity at different irradiances is constant through the wavelength range. However, due to its temperature-dependence, Q^{AS} linearly increases with the irradiance. The dashed lines correspond to the fitting of Q^{AS} according to Equation 3.6, from which it is possible to extract the photothermal parameter β, defined as:

$$T^{NP} = \beta \times I_{Exc} + T_0 \tag{5.3}$$

where T^{NP} and T_0 are the temperature of the nanoparticle in the presence and absence of light (room teperature), respectively.

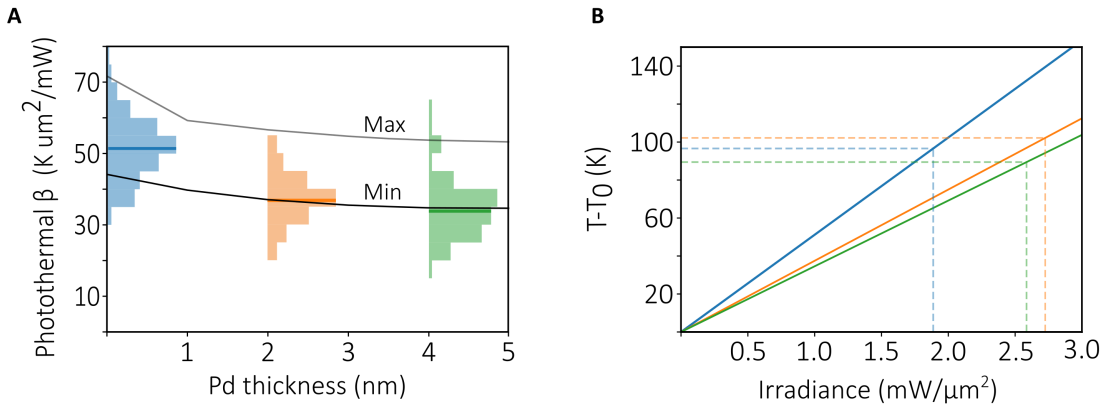

Figure 5.6: **Photothermal coefficient of Au@Pd CS-NPs**. **(A,B)** Extinction spectra of both Au@Pd and Au@AuPd core@shells, indicating the dampening of the LSPR upon intimate contact between the materials. Even small amounts of Pd leads to a strong dampening of the signal. **(C,D)** Extinction spectra of both Au-Pd and Au-AuPd core-satellites configurations. Both are red-shifted in comparison with AuNS LSPR. Au-AuPd appear to induce a larger damping of the LSPR, which can be attributed to the coupling between the AuNS and the AuNPs in the satellite. The bare AuNS spectra is represented by the red dashed line. Extinction spectra are normalized at 400 nm.

Figure 5.6 shows histograms of the measured photothermal coefficients for the three systems under study. The mean value obtained for the Au NS is $\beta_{Au67} = 51 \pm 8$ K μm^2 mW^{-1}, in line with what has been reported for 64 nm Au NS [35]. Interestingly, a significant reduction of β is observed for the CS-NPs. The obtained mean values of the Au67@Pd2 and Au67@Pd4 were $\beta_{Au67@Pd2}= 38 \pm 8$ K μm^2 mW^{-1} and $\beta_{Au67@Pd4}= 35 \pm 8$ K μm^2 mW^{-1}, respectively. The black solid curves represent the theoretical minimum and maximum value for the photothermal coefficient of each structure, derived from a thermal model described in Appendix C. Figure 5.6B (solid lines) shows the temperature increase versus excitation irradiance following Equation 5.3, according to the mean β of each type of NP. In dashed lines, the maximum irradiances used in each experiment are shown. The maximum temperature reached by the NPs was around 100 °C.

It must be noted that this method assumes that the PL emitting object has a homogeneous temperature T^{NP}. This condition is typically fulfilled by Au NS under CW illumination [31] and it must be proven satisfied as well in CS-NPs to use β for a proper surface temperature determination. Calculations on the heat flow in a radial direciton were conducted in a CS-NPs with dimensions according to Au67@Pd2 nm. The parameter employed for the model are shown in Figure 5.7A, and details of the model are presented Appendix C. Figure 5.7B shows the calculated temperature increase T(r)-T_0 as a function of the radial coordinate r for a Au67@Pd2 NP immersed in water under illumination at 532 nm with an irradiance of I_{Exc}=1 mW/μm^2. The proposed model led us to assume that the temperature is practically constant inside the CS-NP, since it only predicts a small drop $\nabla T_{(Au-Pd)}$ at the Au/Pd interface, shown in Figure 5.7C. The temperature variations inside the CS-NP are 10^{-3} times smaller than the temperature increase of the NP surface. Hence, the NP can be described by a single, uniform temperature T^{NP}. This is a consequence of the high thermal conductivities of Au and Pd with respect to water and the high electronic thermal conductance of the Au/Pd interface that allows efficient heat transfer through electron-electron scattering [155,156]. Therefore it is possible to conclude that AS thermometry retrieves the photothermal coefficient and allows to estimate the surface temperature of the entire CS-NPs as a function of the irradiance. Through the model it is possible to derive an analytical expression to estimate the photothermal coefficient of CS-NPs β^{CS}. Equation 5.4 dictates that β^{CS} depends on the radius of the nanoparticle (a), the interfacial thermal resistances between the shell and the surrounding media (Kapitza, $R^{th}_{Pd-H_2O}$) and the conductivity of the surrounding media (κ_{H_2O}). There is an additional factor that accounts for the role of the substrates in dissipating the accumulated heat (Appendix C) [156].

$$T^{NP} = f\left(\frac{1}{4\pi\kappa_3 a} + \frac{R^{th}_{Pd-H_2O}}{4\pi a^2}\right)\sigma_{Abs} I_{Exc} + T_0 \tag{5.4}$$

$$\beta^{CS} = \left(\frac{1}{4\pi\kappa_3 a} + \frac{R^{th}_{Pd-H_2O}}{4\pi a^2}\right)\sigma_{Abs} \tag{5.5}$$

$$f = 1 - \frac{(\kappa_{Glass} - \kappa_{H_2O})}{(\kappa_{Glass} + \kappa_{H_2O})} \tag{5.6}$$

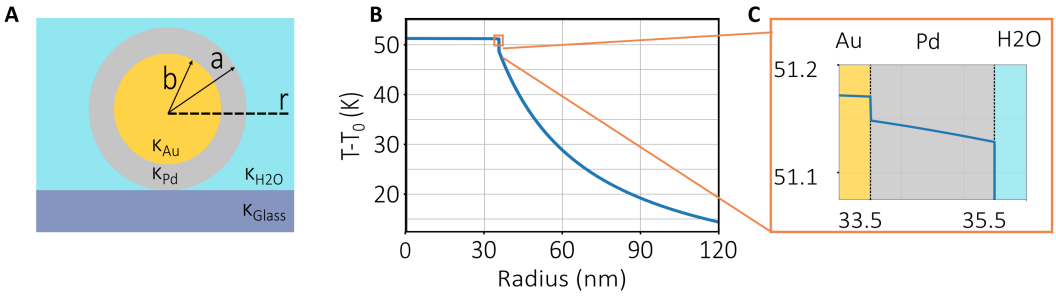

Figure 5.7: **Single-particle optical characterization**. **(A,B)** Extinction spectra of both Au@Pd and Au@AuPd core@shells, indicating the dampening of the LSPR upon intimate contact between the materials. Even small amounts of Pd leads to a strong dampening of the signal. **(C,D)** Extinction spectra of both Au-Pd and Au-AuPd core-satellites configurations. Both are red-shifted in comparison with AuNS LSPR. Au-AuPd appear to induce a larger damping of the LSPR, which can be attributed to the coupling between the AuNS and the AuNPs in the satellite. The bare AuNS spectra is represented by the red dashed line. Extinction spectra are normalized at 400 nm.

The analytical expression for β^{CS} requires several thermodynamical constants for which accurate experimental values are scarce. This is the case for example for the Kapitza resistance between Pd and water $R^{th}_{Pd-H_2O}$. For this reason, we have included a maximum and a minimum calculated value (black solid curves in 5.6), to represent the large dispersions of available data in the literature. A list of used parameters is shown in Table 5.2.

Parameter	Min value	Max value
$R^{th}_{Au-H_2O}$	4×10^{-9} m^2 K W^{-1} [157, 158]	15×10^{-9} m^2 K W^{-1} [159]
$R^{th}_{Pd-H_2O}$	1.8×10^{-9} m^2 K W^{-1} [160]	2.4×10^{-9} m^2 K W^{-1} [161]
κ_{H_2O}	0.6 W m^{-1} K^{-1} [31]	0.68 W m^{-1} K^{-1} [31]
κ_{Glass}	1 W m^{-1} K^{-1}	1.2 W m^{-1} K^{-1} [31]
σ_{Abs}		
a (r_{Pd})	b+Pd shell thickness	
b (r_{Au})	63.6 nm (size distribution)	71 nm (size distribution)

Table 5.2: Parameters for photothermal coefficient estimation in Au@Pd CS-NPs

The calculations reasonably predict the experimental trends. However, it must be noted that for Au@Pd, half of the measured CS-NPs had a value below the predicted range. This could be due to several factors:

- An overestimation of the absorption cross sections: The simulations predict a 10 nm blue shift in the resonant frequency of CS-NPs, which is not observed experimentally [156]. However, considering that the resonances are broad, a 10 nm detuning of the spectrum versus the excitation wavelength only modifies the absorption cross sections by less than 2%

- The influence of the surfactant CTAC in the thermal resistance of the Pd-water interface [157].
- An overestimation of the factor f accounting for the effect of the substrate in heat dissipation. For a spherical NP immersed in water on a glass substrate, f takes a value of 0.875. However, Au@Pd CS-NPs are faceted, as shown in Figure 1B, and can present a larger contact area with the substrate, enhancing heat dissipation. Thermal simulations estimate a value of f= 0.843 for faceted NPs, which is 4% smaller than its spherical counterpart. [156]

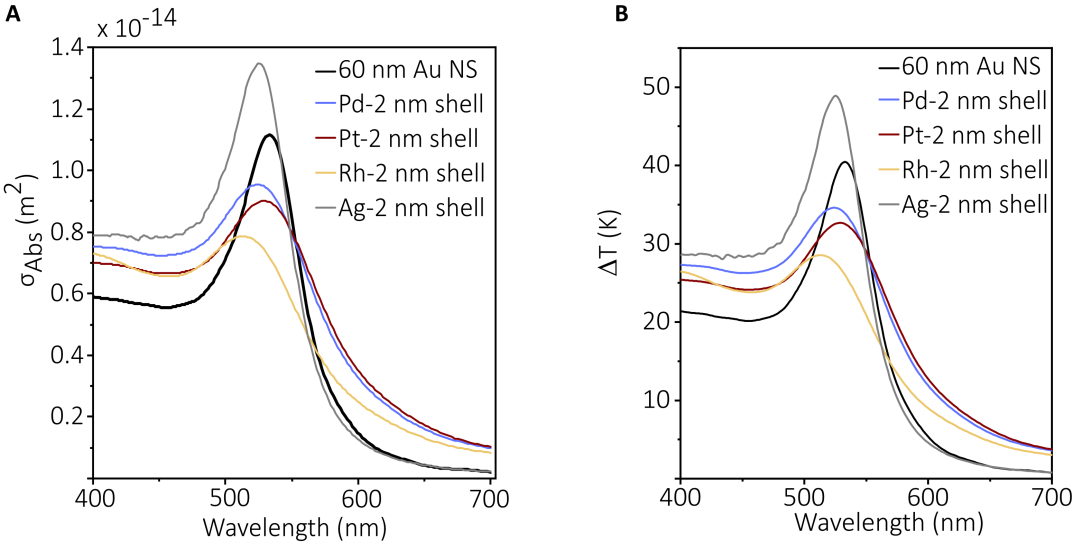

Figure 5.8: **Predicting temperature increase in Au@M CS-NPs. (A)** Absorption cross-sections for Au@M where M= Pd, Pt, Ag and Rh. The absorption cross-sections were obtained from electromagnetic simulations conducted with Lumerical. **(B)** Temperature increase in Au@M CS-NPs.

The expression found through the thermal model can in principle be used to predict which would be the photothermal response of Au@M CS-NPs of identical dimensions in which Au always serves as a core, while M= Ag, Rh, Pt and Pd play the shells. When evaluating Equation 5.4, we can realize that the main parameters to determine are the metal-solvent resistance (Kapitza), the size of the shell, the role of the substrate and the absorption cross-section ($\sigma^{Au@M}_{Absorption}$). If we assume that the thickness is the same, and the substrate and interfacial resistances cause a similar effect in the heat dissipation, is the absorption cross section $\sigma_{Absorption}$ what determines the temperature increase in such structures. The absorption cross sections ($\sigma^{Au@M}_{Absorption}$) are shown in Figure 5.8A, while the temperature increase in panel 5.8B. It is worth mentioning that this is a rough model and the heat flow across the metal-metal interface should be deeply evaluated, since a large resistance would definitely impact on the temperature at the surface of the outermost

layer. Therefore, the validation of the technique to quantify the surface temperature should receive the proper attention.

5.3 Role of morphology in β of Au-Pd Nanosystems

The functionalities of bimetallic nanostructures are not only determined by the material composition, but also by the spatial distribution of the constituents. We demonstrated that the arrangement of materials strongly influences the optical response, and thus the photoreactivity of the catalysts. In the following, the effect of morphology on light-to-heat conversion for different Au-Pd bimetallic structures is investigated.

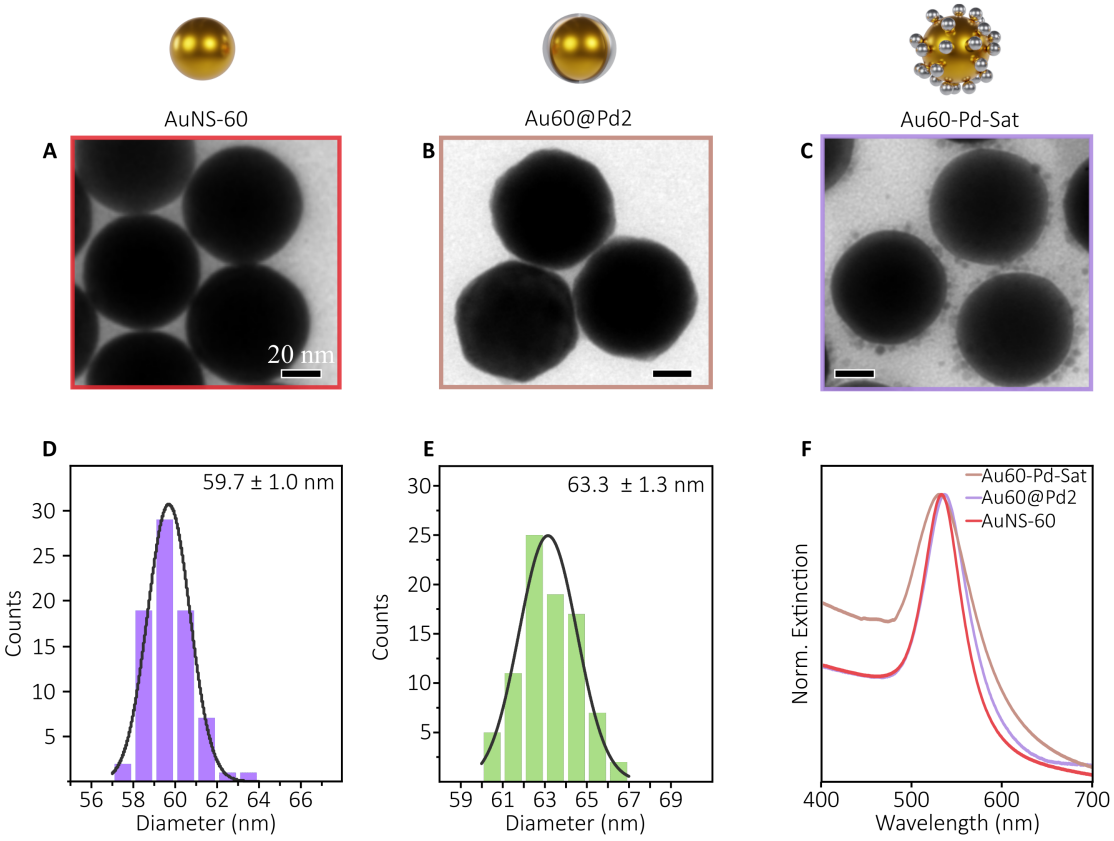

Figure 5.9: **Single-particle optical characetrization**. **(A,B,C)** TEM images of bare Au60 nanospheres, and bimetallic sampels with core@shell (Au60@Pd2) and core-satellites (Au60-Pd-sat) configurations. **(D,E)** Size histogram of Au60 utilized as cores, and Au60@Pd2. The difference between the mean sizes suggest that Pd shell is 20 nm. **(F)** Normalized extinction spectra of three kind. While Au60@Pd2 presented the characteristic damping of the LSPR and blue-shift, the extinction of Au60-Pd-sat was red-shifted in comparison with Au60 and slightly damped.

Similar to the samples utilized in Chapter 4, a set of samples composed of AuNS serving as core, and Au-Pd core@shell and core-satellites were fabricated using the AuNS

as building block. Illustration of the samples employed in this samples are shown in Figure 5.9. The core sample, from now on named as Au60, resulted in spherical NPs, as shown in the TEM image in 5.9A. The size distribution analysis revealed that the sample was very uniform and presented dimesions of 59.7 ±1.0 nm.

Figure 5.9B confirmed the successful deposition of Pd precursor on the Au60. The resulting Au@Pd CS-NPs presented a mean diameter of 63.3 nm and a standard deviation of 1.3 nm (size histogram in Figure 5.9E). Therefore, it is possible to roughly estimate that the thickness of the shell was ∼2 nm from the comparison of the mean diameters. The sample was named as Au60@Pd2. Alternatively, ∼5 nm assembled with 5 nm spherical Pd satellites NPs were assembled around the Au60 cores (Au60-Pd-sat). The homogeneous distribution of Pd satellites was confirmed by TEM images (5.9C).

The optical properties of the three samples were investigated through UV-Vis spectroscopy and the results were very much alike as the ones presented before. Figure 5.9F displays the extinction spectra of the Au60, Au60@Pd2 and Au60-Pd-sat all normalized to their respective maximums. While the core@shell nanoparticle presented the distinctive damping and the blue-shift with the respect to the Au60 LSPR, the core-satellite configuration showed a very similar optical response with a slight red-shift of the maximum. The reason of such behaviours were vastly discussed in Chapter 2.

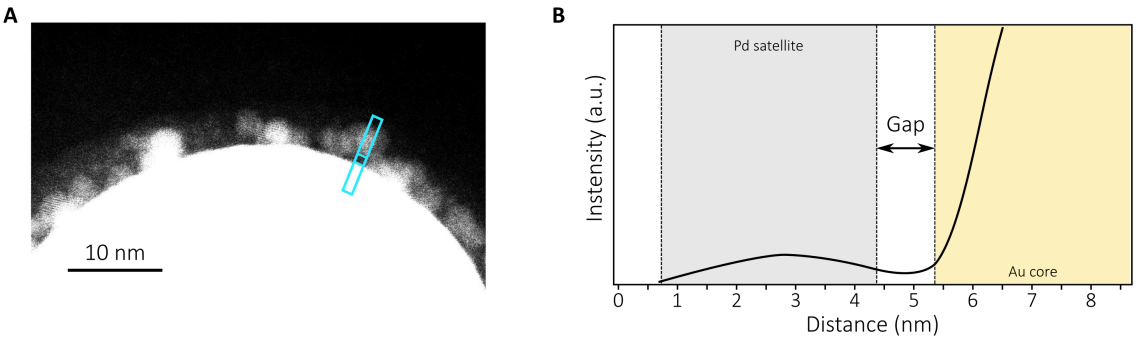

Figure 5.10: **Interparticle gap characterization in Antenna-Reactor system**. **(A)** DF-TEM images of bare Au60-Pd-Sat. The light blue box points out the scanning area when determining the gap size. **(B)** Scanning profile of scattered electron starting in a Pd satellite and moving towards the Au core. The valley in scattered electrons suggest the absence of metallic material and thus, it is used as a proxy for the gap size. The determined size is approximately 1 nm.

Additional characterization was required for the core-satellite (antenna-reactor) system, due to its more complex constitution. Dark-Field TEM operated in scanning mode was employed to determine the interparticle distance (gap) between the core and the satellites. As mentioned previously, the electrostatic assembly relies on the electrostatic attraction between oppositely charged ligands stabilizing the constituents. Therefore, no intimate contact between the NPs is expected. Figure 5.10 shows a DF TEM image of a core-satellite nanoparticle, where many satellites can be observed close to the main core. To avoid the overlap between the two particles, well separated particles were chosen for the

analysis (light-blue box in panel A). The valley in the intensity of scattered electrons (Figure 5.10B) was used as a proxy of the interparticle gap, which was estimated to be approximately 1 nm. The presence of this gap of this dimensions correlates with the absence of damping when determining the extinction spectrum of Au60-Pd-Sat with respect to the naked core (5.9F).

To study the photothermal response of the samples composing the set, optical printing was conducted for Au60 and Au60@Pd2, while a controlled deposition on amine functionalized glass was conducted for Au60-Pd-sat. The approach to reach a single-particle regime had to be modified for the core-satellites because the sample was not stable enough to survive the optical printing and to avoid potential Pd satellites detachment during the printing process.

Again, to determine the photothermal response of the three kind, the PL of each system was studied. Figure 5.11A shows representative single particle PL emissions when excited with laser light at 532 nm in a water environment. A similar trend was observed for the Au60@Pd2, which presented a significant drop in the single particle PL emission in comparison with the Au60 reference. Interestingly, Au60-Pd-sat also presented a drop in the single-particle PL profile, even though the optical properties seemed not to be strongly affected by the presence of satellites around the core. It must be noted that the Pd satellites interact weakly with light and absorb only a minor fraction of the incoming light, as investigated in Chapter 4 (altogether less than 10%, when placed around the core). Hence, the PL emission obtained for that sample is the one mostly emitted by the Au core. The reason for such a behaviour is not clear yet and suitable experiments targeting the physical phenomena must be designed and conducted.

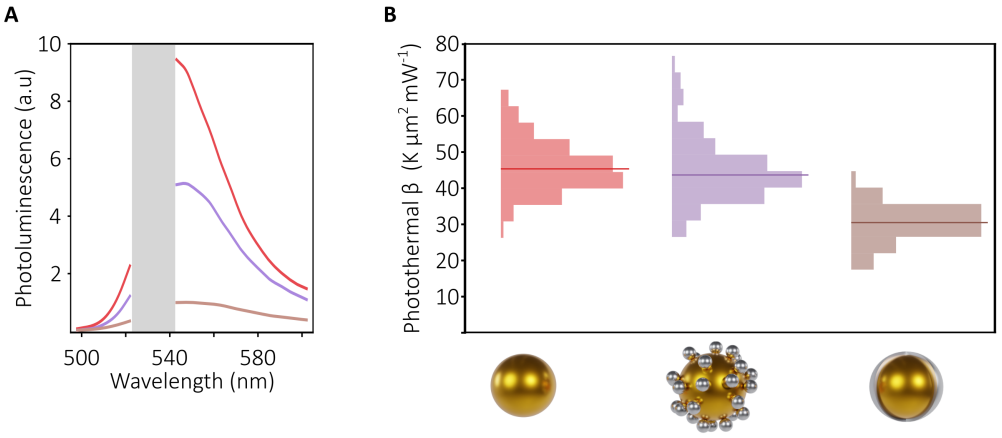

Figure 5.11: **Photothermal coefficient of AuPd nanocatalysts with different configurations**. **(A)** Photoluminescense of the three system. While the core-satellite presented a slightly decreased PL with respect to Au60, the core@shell nanoparticle presented a dramatic decrease in PL. **(B)** Photothermal coefficient (β) for the three systems. The presence of satellites seem not to affect β, while in core@shell structures it gets reduced by a 40% with respect to bare AuNS.

Next, the photothermal coefficient of each system was determined using hyperspectral AS thermometry. The resulting histograms are presented in Figure 5.11B. The median photothermal coefficient for the Au60 cores was $\beta_{Au60} = 47$ K μm^2 mW^{-1} with a standard deviation of 8 K μm^2 mW^{-1}. The obtained value was in agreement with what has been reported [35]. Again, a significant reduction of the photothermal coefficient was observed for the CS-NPs, with a median of $\beta_{Au60@Pd2} = 29 \pm 5$ K μm^2 mW^{-1} and a standard deviation of 5 K μm^2 mW^{-1}, in line with the results presented in the previous section of this work. This implies that there is almost a 40% reduction of the photothermal coefficient when coating a 60 nm AuNS with a 2 nm Pd shell. Remarkably, there's no significant difference with the mean value presented by Au60-Pd-sat, $\beta_{Au60-Pd-sat}2= 46 \pm 13$ K μm^2 mW^{-1}, although the latter presented a larger dispersion. It is worth mentioning that as PL is mostly emitted by the Au, meaning that the measured β can in principle be assigned to the core. As the reactive surface is the Pd, it is important to estimate which temperature would a molecule experience at the surface of a Pd satellite once assembled with the core. In this regard, we conducted optical simulations to investigate the partial absorption modelling the antenna-reactor system based on the experimental data. The geometry of the model consisted in a AuNS of 60 nm serving as core, and 50 satellites (N=50) of 5 nm homogeneously distributed around the core. The simulations were conducted taking 1 nm as the interparticle distance.

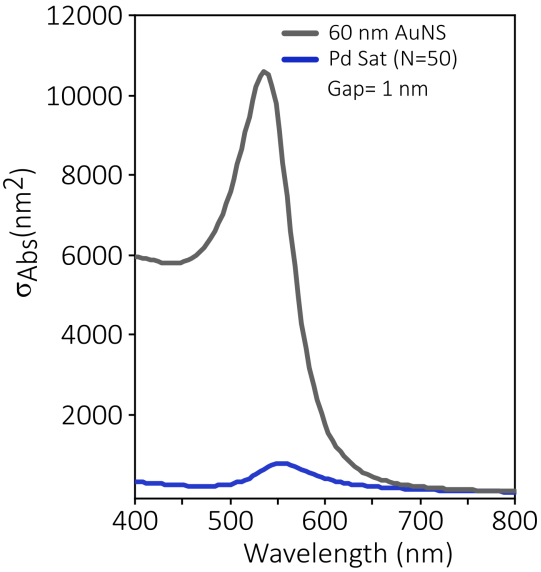

Figure 5.12: **Partial absorption cross-sections in Antenna-Reactor**. Partial absorption cross-section for a 60 nm Au core and 50 Pd satellites (∼5 nm in diameter) placed at 1 nm from the core. The 60 nm AuNS absorption represents almost 90% of the total.

As expected, the 60 nm AuNS is the component contributing the most to the total

absorption, absorbing almost 90% of the incoming light, while 50 satellites of the above-mentioned dimensions, only represent 10% (Figure 5.12B). Due to this very low partial absorption cross-section per satellite, and the fact that temperature drops proportional to $1/r$ from the surface of AuNS [162], a large difference for the surface temperature of Pd satellites is not expected.

Before concluding the section it is important to highlight that the thermal evaluations conducted when evaluating the structure-performance correlation in photocatalytic activity of plasmonic bimetallic photocatalysts were in the correct order of magnitude for the used irradiance. This reaffirms the major role of the optical hotspots for the enhancement of reaction rates.

Sample	Dimensions (nm)	LSPR maximum (nm)	β (K μm^2 mW^{-1}); λ=532 nm.
Au60	59	532	47±8
Au60@Pd2	63	530	29±5
Au60-Pd-sat	59;∼ 5 nm (sat)	535	46±13

Table 5.3: Geometry-dependent photothermal coefficient.

Overall, the experiments presented in this section point out that the presence of an interface between the two metals is crucial and dictates the photothermal response of the bimetallic nanostructures. The direct contact between Au and Pd is what modulates the surface damping of the Au plasmon, and has been proven that a large contact area modulates the interaction between the materials, worsening the quality of the resonator and diminishing the overall absorption in bimetallic systems. Conversely, a configuration in which the reactor is placed a few nanometers away from the plasmonic component leads to the preservation of the optothermal properties. Anti-stokes thermometry is mainly sensing the temperature of the emitter, which in this configuration is the Au core. Nevertheless, due to the small partial absorption per satellite, we hypothesize that the temperature at the surface of the Pd satellite should not differ dramatically and molecules reacting at their surface should experience similar temperatures that the one at the Au surface. This suggests that the surface of Pd NPs can be thermally activated when placed in the proximity a plasmonic antenna and elevated irradiances. This results have positive impact in photocatalysis, since the efficiency of a transition metal based catalyst can be boosted due to the heat delivered by a plasmonic component.

5.4 Conclusion

Upon the fruitful combination of plasmonic and catalytic metals for light-driven chemical transformations, quantifying the heat contribution to reaction rate enhancements was the natural next step to understand which phenomenon determines the boost. Here, samples carefully designed to address this central question enabling us to gain insight on this regard. Our findings are shortly summarized below.

First, we evaluated the changes on the photothermal properties induced by the presence of a thin Pd shell coating the Au core. We also varied the thickness of the shell to understand this effect further. We found that the inclusion of a Pd shell in the order of ∼2 nm is detrimental for the ability to convert light into heat, as evidenced by the reduction by a 26% of the photothermal coefficient (β) for Au67@Pd2 core@shell structures with respect to the bare Au67. Nevertheless, the thickness of the Pd shell does not seem to have a strong influence. Only a 6% decrease in the photothermal coefficient was observed when the Pd thickness was increased from roughly 2 to 4 nm. In addition, it was found that as the heat flow towards the outermost surface is not restricted by the Au-Pd interface, the absorption cross section of the Au@Pd CS-NPs is the main parameter influencing its photothermal coefficient.

We also evaluated the role of the geometry, which is strongly correlated to the reactivity of the bimetallic nanocatalyst. Our observations highlight that whereas coating the Au 60 nm cores with a thin homogeneous shell of Pd reduces the photothermal coefficient dramatically by almost a 40%, the assembly of small spheres around the core does not seem to have a similar effect. Indeed, we obtained very similar photothermal coefficients for naked core (47 μm^2 mW^{-1}) and core-satellites structures (46 μm^2 mW^{-1}). This study strongly highlights the importance of the interface between the materials, since the interaction among them and consequently, the photothermal response, seem to be strongly modulated by the intimate contact between the plasmonic and the catalytic constituents.

Chapter 6

From single-particle to metasurfaces

The constructive combination of plasmonic-catalytic pairs place them as promising materials for future technologies. Yet, the field still facing experimental limitations that hamper their scalability to industrial levels. This is reflected in the still very low apparent quantum efficiency (less than 1% in the best example) [69], a metric for the conversion of photons into molecules. Several reasons are holding back the full exploitation of these materials. For instance, when a concentrated colloidal suspension is used in photocatalytic tests, multiple scattering and absorption events prevent the simultaneous activation of all nanostructures, and thus their performance is averaged between those operating under illumination and those in the absence of light (pure thermal catalysis) [163]. This brings up the challenge of manufacturing suitably engineered reactors, often a non-trivial task. In addition, ligands providing stability to colloidal nanoparticles can undergo photochemical desorption [164, 165], inducing the uncontrolled aggregation of individual NPs. Moving from colloidal suspensions to a planar configuration is an appealing strategy to circumvent the light penetration and aggregation limitations [166, 167, 168]. In this regard, plasmonic two-dimensional (2D) metasurface, devices with artificial photoresponse governed by the periodic organization of individual components [43], promote the transition from three-dimensional to two-dimensional, seeking for better exploitation of the cooperative effects observed in bimetallic photocatalysts.

In this project we developed a methodology that enabled us to accomplish a 2D bimetallic metasurface, in which AuNSs were assembled into a periodic hexagonal array with Pt-NPs placed at the interparticle gaps of the AuNSs. Thus, extending the preferred antenna-reactor configuration throughout the structure. The large surface hotspot density offered by the metasurface is expected to capitalize the use of active metals for catalytic applications.

6.1 Metasurfaces: background

Metamaterials is the name that has been given to artificially structured materials whose optical properties are dictated by the arrangement of individual resonators, which are posi-

tioned to each other at distances smaller than the wavelength of the incident light [43]. Similar to what occurs in solids, the building blocks are often referred to as *meta-atoms* (Figure 6.1). Analogously, when the meta-atoms are arranged in a 2D array, they are denominated as *Metasurfaces*. The motivation to fabricate these type of repetitive structures relies on the new arising optical behaviour. Particularly for plasmonic metasurfaces, the collective response yields the formation of highly intense electric field regions (hotspots), and the possibility to excite surface lattice resonances with significantly reduced losses [169, 170].

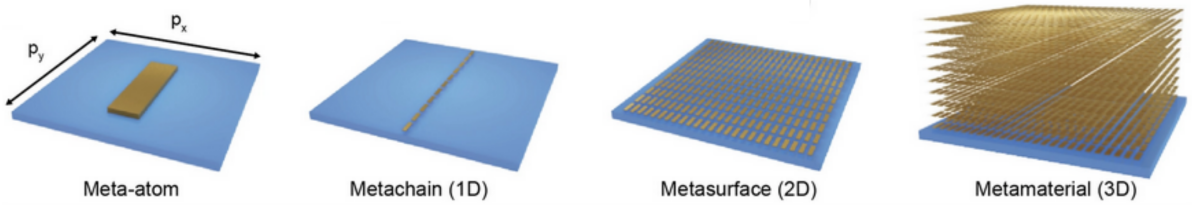

Figure 6.1: **Meta-atoms and meta-arrays.** Sketch representing the repetitive arrays of different dimensions (1D, 2D and 3D) that can be obtained by engineering single-resonators (meta-atoms) keeping the distance between them smaller than the incident wavelength. Extracted from [43]

Recently, a new appealing direction for metasurfaces fabrication emerged (Figure 6.2). Instead a normal top-down approach, this colloidal method consists on tailoring the interaction between the AuNS in order to direct the 2D deposition [93, 109, 171]. In these structures, the the distance between the resonators is constrained to the size of the molecules binding them [93, 109, 171]. As their preparation was briefly mentioned in Chapter 3, now the most relevant optical properties will be discuss, which will be helpful to understand later how those were exploited for photocatalytic purposes.

As a result of PSS-directed growth, an hexagonal array of AuNS is formed extending across the plane. Figure 6.2A illustrates the procedure and shows an example of the resulting metasurface. The concentration of AuNS employed in the assembly step allows the tunability of the number of cumulative layers, controlling the thickness of the metasurface. The repetitive structure leads to a collective optical behaviour within the visible-Near IR region. For monolayers, while at longer wavelengths most of the light is reflected off as in a mirror, at shorter wavelengths the *d-to-s* interband transition are activated. However for bi-, tri- or multilayers, the metasurface present an overall coupling manifested as polaritonic modes, accompanied by unprecedented light-matter coupling [171]. These polaritonic modes are typically red-shifted with respect to the dipolar LSPR of individual AuNS, falling in the NIR region (Figure 6.2B) and the number of modes scales with (N-1), where N represents the number of layers (Figure 6.2C). The spectral position of these modes can be tuned by changing the size of the nanoparticles, as well as the interparticle gap [93,109]. Also, a spectral region defined as stopband (eV, nm) appears for metasurfaces

with N>2, in which the structures almost reflects off the totality ($\sim$ 90%) of the incoming light and no modes can be excited [171,172]. These region extends roughly between 400-700 nm.

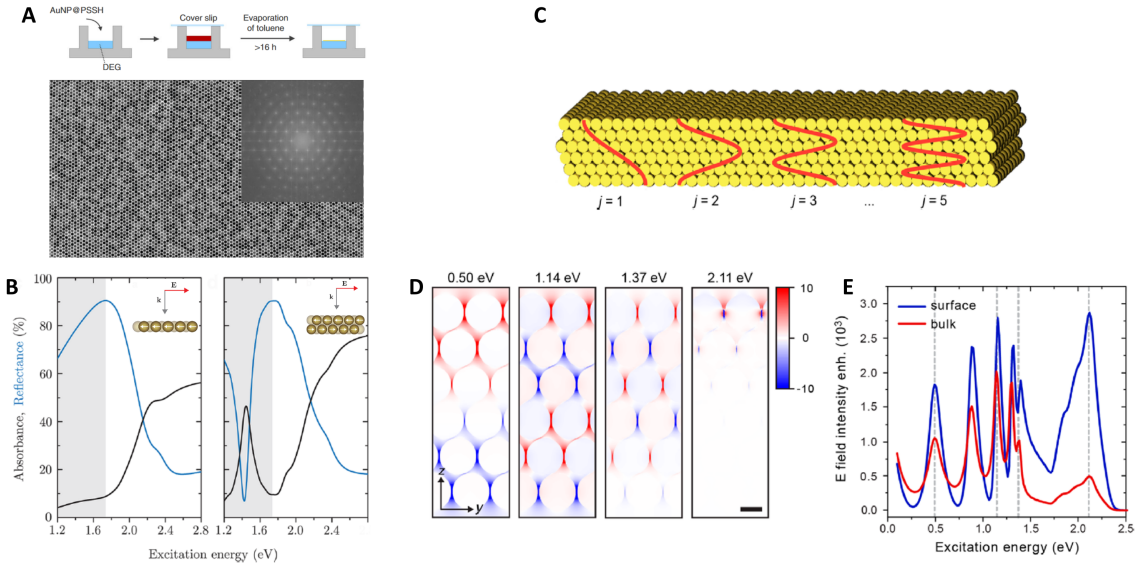

Figure 6.2: **Optical properties of metasurfaces**. **(A,B)** Transmission Electron Microscopy (TEM) image of Au metasurface made of 22 nm AuNS at to different magnifications. Interparticle gap of nanoparticles is $\sim$2 nm. **(C)** Representative transmission microscope image of the metasurface. The different blue hues indicate different number of particle layers (1L, 2L, 3L and 3L+ stand for mono-, bi-, tri and multilayers). **(A, B, C) Adapted from [93, 172, 173]**

The close proximity of the individual NPs in the periodic array results in the formation of plasmonic hotspots at the interparticle gaps, spatial regions characterized by intensified electric fields [173, 174]. The presence of hotspots in plasmonic structures has been demonstrated to play an important role in surface processes [46, 175]. While the electric field outside of the nanoparticles can enhance the absorption and emission of molecules for vibrational spectroscopy, such as surfaced-enhanced Raman scattering (SERS) and infrared absorption spectroscopy (SEIRA) [173], the intensity of the electric field inside the nanoparticle dictates the excited carriers generation and local temperature rise [29,30,31]. Figure 6.2D maps the hotspots of a 6 layers metasurface at different energies. The striking feature is that volume hotspots (in deeper layers) are formed when only exciting polaritonic modes. However, the surface hotspots (at the topmost layer) can also be excited within the stopband spectral region, corresponding to visible light. Throughout our investigations, we proved the relevance of hotspots in bimetallic structures, since the confined electric field boosts the otherwise weak absorption of the catalytic center within the visible range [48]. Thus, the large surface hotspots density offered by the metasurface can be useful for photocatalysis, if the interaction of the highly intense electric field regions and the catalytic metals is optimized.

6.2 Synthesis and Characterization of 2D metasurfaces

Fig. 6.3 presents the microscopical characterization of the synthesised plasmonic metasurface. The monometallic 2D metasurface (*Au metasurface*) that serves as reference/control. The precise control of the synthesis of AuNSs, their surface chemistry, and the self-assembly step resulted in a well-packed hexagonal array of 22 nm AuNSs with an edge-to-edge distance of ∼2 nm (cf. Fig. 6.3A). The homogeneity of the structure over a large area is shown in the transmission electron microscopy (TEM) image in Fig. 6.3B, extending up to a few square millimeters. Besides monolayers also areas with multilayer emerged during the crystallization process (cf. 6.3C), leading to different optical properties. Optical microscopy in transmission mode was the tool that allowed us to identify the different layer numbers due to contrast difference, indicating different sample thicknesses. One example of the Au metasurface in transmittance is depicted in Fig. 6.3C. The lighter the blue, the thinner the metasurface. Hence, the unambiguous color contrast was utilized to determine the area sizes of the different layer numbers.

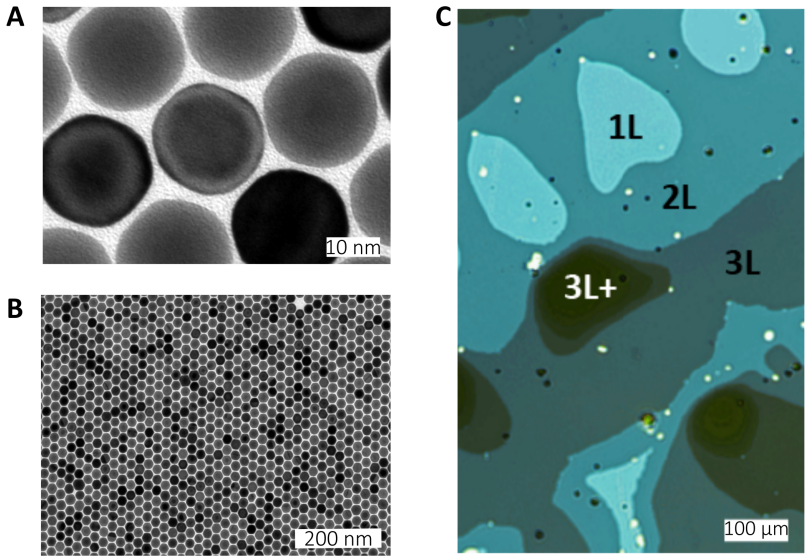

Figure 6.3: **Microscopic characterization of Au metasurface**. **(A,B)** Transmission Electron Microscopy (TEM) image of Au metasurface made of 22 nm AuNS at to different magnifications. Interparticle gap of nanoparticles is ∼2 nm. **(C)** Representative transmission microscope image of the metasurface. The different blue hues indicate different number of particle layers (1L, 2L, 3L and 3L+ stand for mono-, bi-, tri and multi-layers).

The colloidal approach for metasurface fabrication was extended to bimetallic structures comprised of AuNS and Pt nanoparticles (PtNPs). A TEM image and size histogram of PtNPs used for the accomplishment of the hybrid structure are shown in Figure 6.4A and

B, respectively. The mean diameter of the PtNPs was estimated to be 2.7 nm and the corresponding standard deviation 0.6 nm.

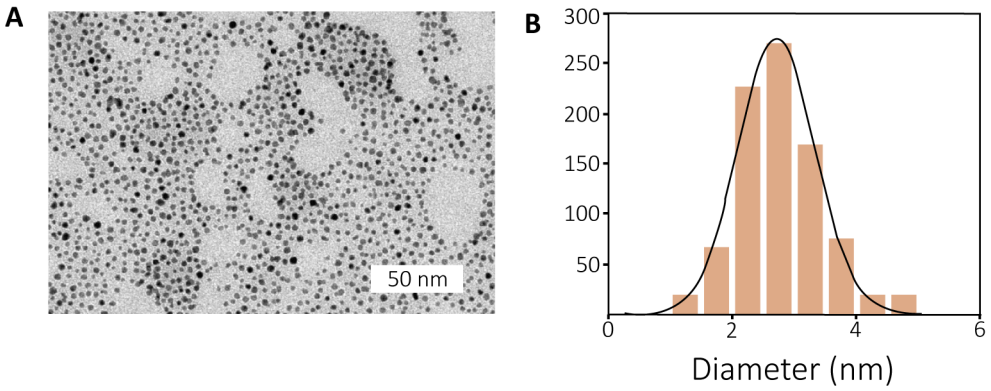

Figure 6.4: **Pt nanoparticles characterization**. **(A)** TEM image of PtNPs used as reactive center in bimetallic metasurfaces. **(B)** Histogram showing the size distribution of Pt nanoparticles. The obtained size was 2.7 ± 0.6 nm.

Through PSS functionalization, we managed to assemble both, the 22 nm AuNSs and ∼ 3 nm PtNPs simultaneously, yielding a bimetallic metasurface (*AuPt metasurface*). The integration of the highly active metal, realized a metasurface with combined optical and catalytic properties. In this composition the AuNSs dominate the optical behaviour, whereas the PtNPs act as the active site for chemical reactions. Notably, the homogeneity and spatial periodicity of the metasurface was not affected by the presence of PtNPs (Fig. 6.5A). During the assembly step the PtNPs were placed at the interparticle gaps between the AuNSs, which increased the gap size to 3.5 nm. The crystalline phase of each material was confirmed via HR-TEM (Fig. 6.5B). The location of Pt NPs was not affected with the increasing number of layers and multilayer domaind were also obtained (Figure 6.5C). Therefore the sample was constituted by PtNPs located in the interstices (gaps) of the 2D-hexagonal array of AuNSs, with no direct contact between the two components of the bimetallic AuPt metasurface. This configuration was acknowledged as antenna-reactor [82, 176], which extends all along the 2D structure. The material composition was also investigated using EDS. As can be seen in Figure 6.5D, while the Au signal is constrained to the location of AuNS in the structure, the Pt signal is more diffuse due to the spectral overlap of Au Bremsstrahlung radiation and Pt X-ray emission. Nevertheless, as the particles were synthesized in different batches and later on, assembled, the presence of Pt in the AuNS location is highly unlikely. Hence, the developed methodology allows to accomplish bimetallic metasurface with desired antenna-reactor configuration. The size of the metasurface extends consistently up to several square millimeters retaining the periodicity. The full description of the fabrication process can be found in the Appendix B.

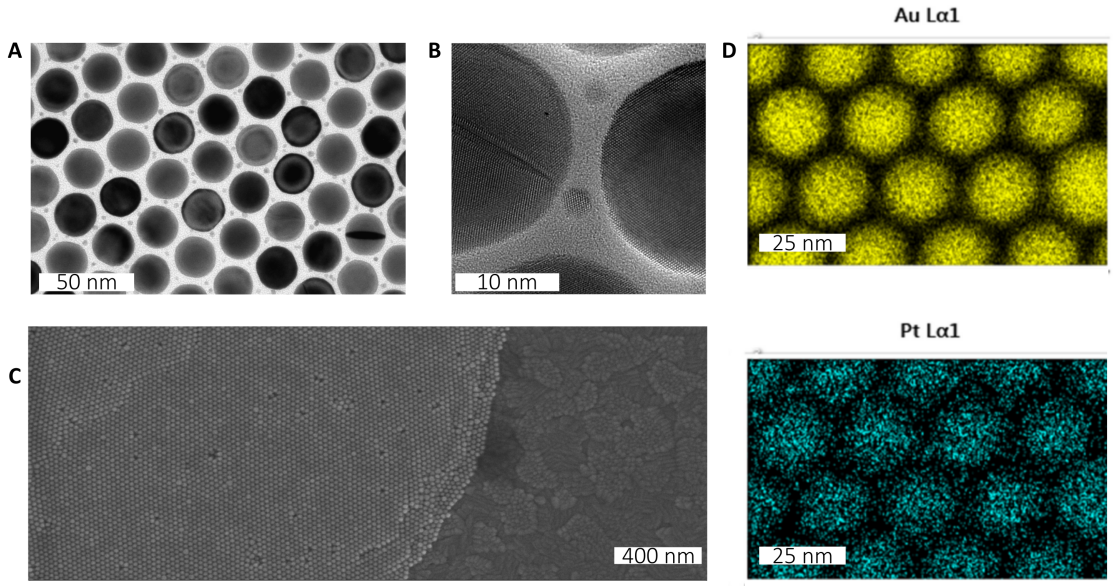

Figure 6.5: **Microscopic Characterization**. **(A)** TEM of a monolayer domain in AuPt metasurface sample. The metasurface was obtained assembling 22 nm AuNSs and $\sim$ 3 nm PtNPs. **(B)** HR-TEM of AuPt metasurface evidencing the crystalline phases of both AuNS and PtNPs. **(C)** SEM image of ITO-supported AuPt metasurface, where the multi-layers domains are observed.**(D)** EDS of AuPt metasurface for materials spatial distribution. While Au is well defined and only present where AuNSs are, the signal from Pt is more diffuse due to the spectral overlap of Au Bremsstrahlung radiation and Pt X-ray emission..

6.2.1 Optical properties of bimetallic metasurfaces

For the following optical and catalytic measurements both *Au and AuPt metasurfaces* were transferred to glass substrates covered with a thin layer of indium tin oxide (ITO), to avoid charging during the scanning electron microscope (SEM) imaging and to facilitate catalysis experiments serving as a support. In the transfer process, domains with different number of layers were deposited on ITO and as mentioned, the optical properties show a strong dependence on the number of layers. Thus, the overall optical properties of the ITO-supported metasurfaces were investigated before their utilisation as photocatalysts.

Micro-transmission and reflection measurements were performed to investigate the optical properties of the ITO-supported Au and AuPt metasurface within the spectral range of 450-850 nm. The spectra were taken in both cases on mono-, bi-, and trilayers (1L, 2L, 3L). The absorbance (A) was calculated afterwards as difference between the transmitted (T) and reflected (R) light. The resulting spectra for the pure Au metasurface are shown in Fig. 6.6A and the spectra for the bimetallic sample in Fig. 6.6B. The obtained experimental spectra are in good agreement with the finite time-domain (FDTD) simulations of both metasurface structures, also shown Figure 6.6. For the *Au metasurface* as well as the AuPt metasurface, the spectrum of monolayers is dominated by interband transitions of the gold, damping the dipole-active bright mode [174]. For bi- and trilayers, the character-

istic polaritonic modes that occur due to deep strong light-matter coupling, start to appear between 650 and 750 nm [171]. Besides the dependence on film thickness and the diameter of the particles, it also depends on the gap size and the dielectric environment [171, 173]. Therefore, the small red-shift of the bimetallic spectra with respect to the resonances presented by the monometallic metasurface can be explained by the larger gap size and the changes in the refractive index of the background due to the presence of PtNPs.

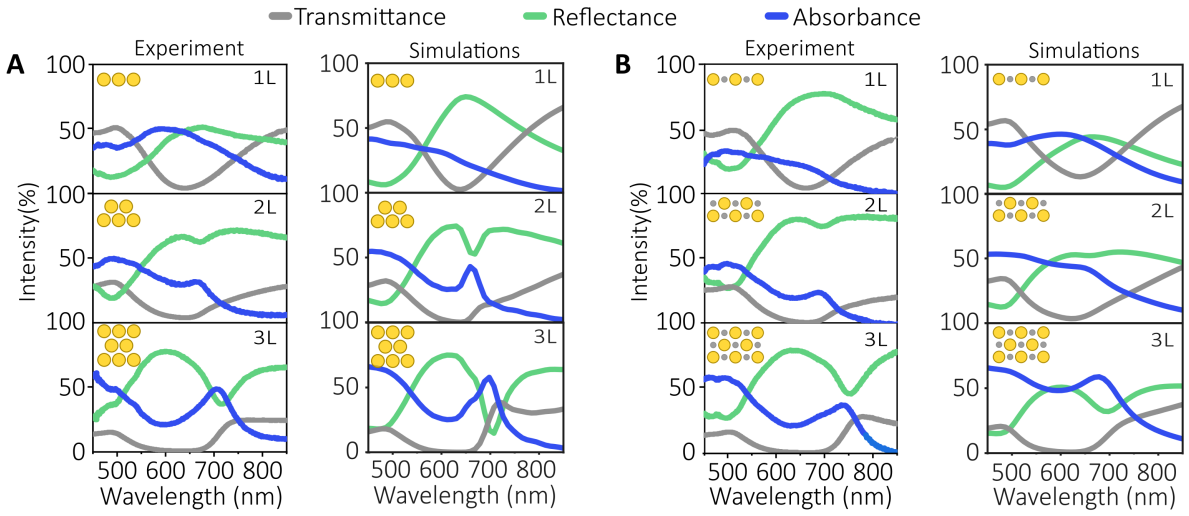

Figure 6.6: **Optical characterization of layers in metasurfaces**. **(A)** Experimental and simulated layer dependent reflectance (green), transmittance (blue) and absorbance (red) spectra of the pure Au metasurface. **(B)** Experimental and simulated layer dependent reflectance (green), transmittance (blue) and absorbance (red) spectra of AuPt metasurface.

Table 6.1: Compositional Aanalysis by Optical Microscopy for Both Au and AuPt metasurfaces

Sample	Monolayer (1L)	Bilayer (2L)	Multilayer (3L+)
Au supercrystal	81%	16%	3%
AuPt supercrystal	61%	9%	30%

As mentioned, the color contrast of the metasurface layers, when imaging with an optical microscope in transmission mode, enabled to estimate the size of the domains. Thus, it was possible to calculate the overall optical response of the samples by weighting the experimental response of the individual layers by the different area sizes. The different layer ratios are important to know, since during the catalysis experiments a large area of the sample will be illuminated that contains different layer numbers. The details on the sample composition are given in Table 6.1. The study revealed that monolayers with ∼80

% coverage for the control sample and ∼60 % for the AuPt metasurface make up the main part of the samples. While the bimetallic sample also has a significant amount of tri- and more layers (∼30 %), the monometallic sample only consists of ∼3 % multilayers.
The weighted optical behaviour of the control and AuPt sample are depicted in Fig. 6.7A and B. As expected, due to the large contribution of monolayers the overall response of the ITO-supported metasurface was dominated by the interband transitions of the gold. In contrast to the pure Au metasurface, the optical response of the AuPt sample shows an influence of the multilayers. Two shoulders are clearly visible in the absorbance spectrum at 671 and 732 nm due to the presence of the polaritonic modes in the bi- and trilayers. Once the optical response of the samples was determined, they were tested as catalysts for FA dehydrogenation.

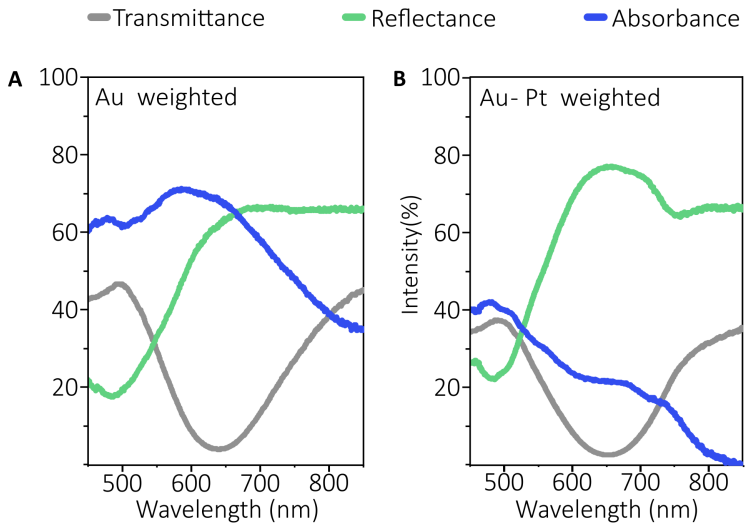

Figure 6.7: **Weighted optical response of ITO-supported metasurfaces**. Weighted reflectance (green), transmittance (grey) and absorbance (blue) spectra of the **(A)** pure Au and **(B)** the bimetallic metasurface, estimated from the percentage of mono-, bi- and trilayer domains.

6.3 Photocatalysis performance of Au and AuPt metasurfaces

The photocatalytic power of the resulting metasurface was investigated by testing their performance on the formic acid (HCOOH, FA) decomposition without any further additives. To recap what was said in Chapter 4, the probe reaction could follow two different pathways, namely dehydrogenation or dehydration. The former produces H_2 and CO_2 and is favoured thermodynamically (ΔG= -48.4 kJ mol^{-1}), whereas the latter produces H_2O and CO (ΔG= -28.5 kJ mol^{-1}) [177]. It has been proven that Au present the lower activity of Au compared to Pt towards FA dehydrogenation [81]. The experiments were conducted

in the absence (dark) and presence of light and repeated at least three times each to ensure reproducibility. It has been shown that the probe redox reaction CO was not detected throughout our experiments, excluding dehydration. For these studies a broadband lamp, equipped with an ultraviolet long-pass ($\lambda > 400$ nm) and an infrared filter, was used as a source of light, to work exclusively in the visible range of the spectrum and rule out heat generated from solvent absorption. An external cryostat set at 25°C was used to control the temperature during the reaction. The experiment was set up for the reactor to be illuminated with ∼110 mW cm^{-2}, which corresponds to sunlight irradiance. Stirring conditions (500 rpm) helped to reduce any temperature gradient [131].

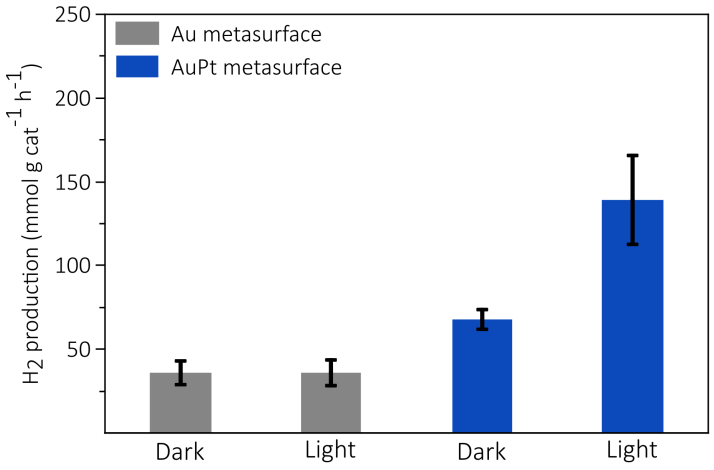

Figure 6.8: **Photocatalytic Performance of Au and AuPt metasurfaces for H_2 generation**. Reaction rate normalized by the total mass of catalyst in both conditions, dark and light for mono and bimetallic metasurface.

Fig. 6.8A shows the H_2 generation (mmol g cat^{-1} t^{-1}) of ITO-supported Au and AuPt metasurface when tested for the FA decomposition. While the H_2 moles were calculated from the GC chromatogram, the mass of the catalysts was obtained by inductively coupled plasma mass spectrometry (ICP-MS), see Appendix D. The Au metasurface presented an activity of 36 mmol g catalyst^{-1} h^{-1} and a negligible enhancement upon illumination. Conversely, the only inclusion of small amounts of PtNPs to the metasurface increased the performance of the binary metasurface up to 67 mmol g catalyst^{-1} h^{-1}. Surprisingly, when illuminated with white light, the performance was further increased by a factor of two, reaching 139 mmol g catalyst^{-1} h^{-1}. The improved performance of Pt in light experiments suggests that the interaction of the incoming light with the Au array results in energized Pt, useful for catalytic purposes. Indeed, to the best of our knowledge, the AuPt metasurface is positioned as the best plasmonic performer when FA is used as H_2 carrier [69].

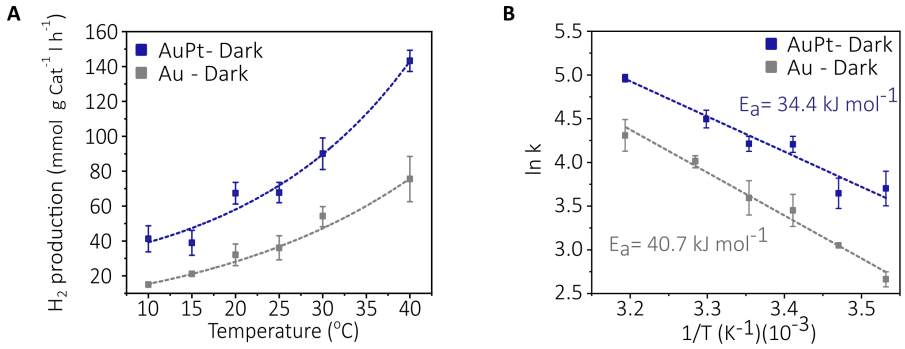

Figure 6.9: **Temperature dependent performance of Au and AuPt metasurface**. **(A)** H_2 generation rate mono and bimetallic metasurface as a function of temperature (absence of light) **(B)** Arrhenius plots. The E_a for Au meta surface was estimated to be 40.7 kJ mol^{-1}, while the sole inclusion of Pt reduced the E_a down to 34.4 kJ mol^{-1}, as expected from the higher Pt activity with respecto to Au.

Temperature-dependent experiments were conducted to evaluate the activation barrier (E_a) [63]. Thus, we first investigated the temperature-dependent activity of the Au metasurface versus the AuPt metasurface across a 10-40°C temperature range, without illumination. The superior activity of the bimetallic sample was always preserved in the chosen temperature range, as indicated in Figure 6.9A. The Arrhenius plot enables to estimate E_a from the slope. This way, we determined that H_2 generation from FA in Au metasurface was characterized by E_a=40.7 kJ mol^{-1}, while the one for the bimetallic was E_a=33.4 kJ mol^{-1} (cf. blue curve in Figure 6.9B). This values denote the larger activation of FA molecules at the Pt surfaces and therefore, the lesser energy to undergo to its dehydrogenation pathway.

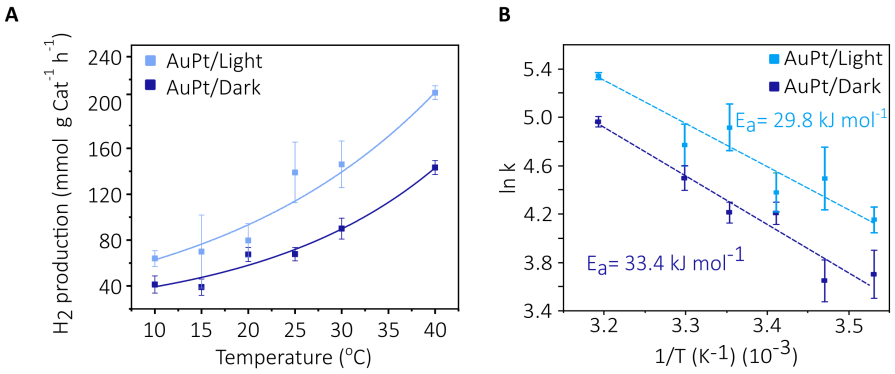

Figure 6.10: **Plasmon-induced E_a decrease in AuPt metasurface**. **(A)** H_2 generation rate of AuPt metasurface in both conditions, dark and light **(B)** A decrease from from 33.4 (dark blue) to 29.8 kJ mol^{-1} (light blue) upon white light illumination was estimated from the Arrhenius plots. Irradiance used in all experiments $\sim$ 110 mW cm^{-2}

The same temperature dependent study was carried out again, but now comparing the activity of AuPt metasurface in dark and light within the same temperature range. Interestingly, we found the H_2 production was always enhanced across the range upon light assistance, although the enhancement factor (ratio light/dark) was not constant (Figure 6.10A). Despite this, the use of white light for photocatalysis resulted in a 10% decrease in the activation barrier for the Pt-FA interface (Figure 6.8B). All these experimental results highlight the synergy between the optical properties of the hexagonal array of 22 nm AuNSs and the interstitial PtNPs for light-driven H_2 production. Having determined the benefit of the bimetallic structure, the next section will be dedicated to disentangle the plasmonic contributions to the improved performance of AuPt metasurface towards the H_2 generation.

6.4 Mechanistic Insight

The superior photocatalytic activity clearly suggests that PtNPs benefit from the optical properties of the metasurface. Several possible contributions are discussed for plasmonic photocatalysis with mono- or bimetallic systems: enhanced near-fields, thermalized hot carriers, non-thermalized hot carriers and local heating [178]. Hence, unravelling the phenomena leading to the improved PtNPs performance at the interparticle gap of the Au array is crucial to fully exploit the advantages of such structures. A set of experiments was conducted to gain insight into the PtNP activation due to the interaction between the incoming light and the metasurface.

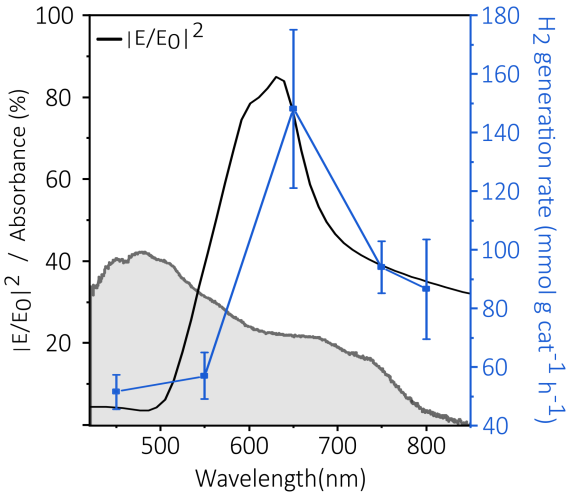

Figure 6.11: **Wavelength dependent, E-field enhancement and absorption in AuPt metasurface (A)** Wavelength dependent H_2 production (blue) plotted simultaneously with the E-field strength (black) in the hotspots of the top most layer within the visible range and the weighted absorbance (red). A clear correlation is seen between the intensity of electric field at the hotspot and the photoactiviy of AuPt metasurface.

First, wavelength-dependent catalytic experiments were performed on the bimetallic metasurface, allowing to discriminate of the photocatalytical response at different spectral regions [179]. For these tests, the broadband lamp was equipped with bandpass filters centered at 450, 550, 650, 750, and 800 nm, having a bandwidth of 20 nm. The power (5 mW) was corrected for each wavelength to conduct the experiments with a constant irradiance and to match the power used previously with unfiltered light.

The resulting wavelength-dependent H_2 generation rates are shown in Fig. 6.11A, simultaneously plotted with the simulation of the enhanced electric field intensity at the hotspot for the topmost Au-layer within the same spectral range (black curve), and the weighted absorbance (shaded area). Only the top layer of each domain was considered in the simulations, as it is where the catalysis mainly occurs. The average electric field enhancement at the hot spots was calculated by FDTD-simulations. Due to the relevance of the hotspots in photocatalytic processes [48, 135], the simulations were evaluated in the center of an interparticle gap between two gold particles, since this is the place where we expect the PtNPs with the highest photocatalytic activity due to the strongest hotspots there. Due to the complexity in averaging in the presence of PtNPs, the E-field was averaged in the gap volume.

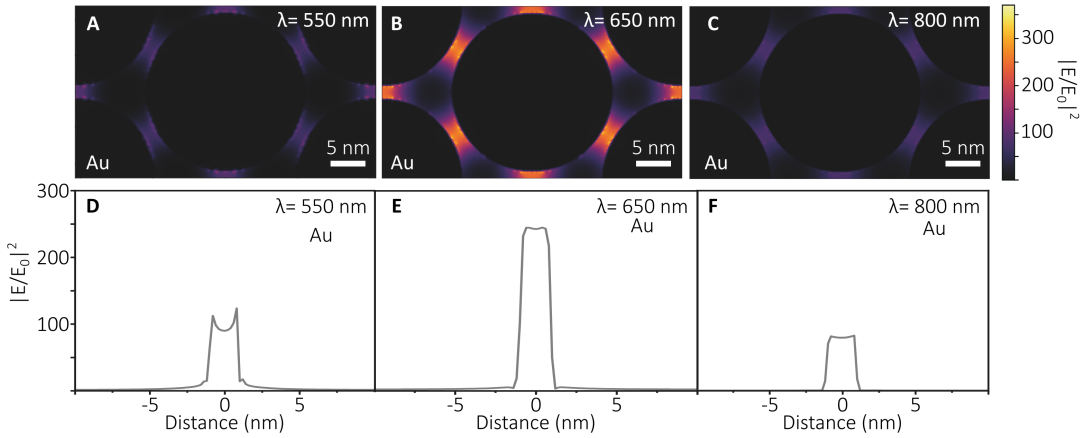

Figure 6.12: **E-field map in Au metasurface (A, B, C)** Electric field enhancement maps of the pure Au metasurface for different excitation wavelengths (550, 650 and 800 nm). Showing the different hotspot intensities. **(D, E, F)** Line scan of the electric field enhancement over the gap of two AuNSs.

As can be observed, the photoactivity of the AuPt metasurface correlates with the electric field enhancement, since the reaction rate peaks at the enhancement maximum. Also, the largest photocatalytic rate was observed at wavelengths where any polaritonic mode is excited, and only interband transitions in Au are promoted. Interestingly, the maximum reaction rate is not presented at the spectral region in which the absorption is maximized (400-500 nm). Based on these results, it can be inferred that around 650 nm, the plasmonic components are funnelling more energy towards the PtNPs, boosting their absorption and thus, increasing the excited carriers generation at the active metal

contributing to the redox reaction [15,48,135]. This manifests as an improved performance in catalysis at that wavelength. Moreover, if heat would have caused the rate boost, a larger enhancement would have been expected at shorter wavelengths, where the absorbance maximizes [83].

Optical simulations were performed to screen the electric field enhancement across the gap when exciting the AuPt metasurface in and out of the field enhancement maximum covering the wavelength range used in photocatalytic experiments (550, 650, and 800 nm were the selected wavelengths). The models were built-up based on the physical features obtained from microscopic characterization. To simulate unpolarized light, X and Y polarizations were averaged. The maps for Au metasurfaces are shown in Figure 6.12A-C. It can be seen that the largest field enhancement ($|E/E_0|^2$) is observed at 650 nm, increasing the intensity of the electic field at the hotspot in almost 250 times. Contrarily, a poorer enhancement is seen for either shorter (550 nm) and longer wavelengths (800 nm), similar among them and in the order of 100-fold increase. Similar experiments were conducted to gain insigth on what occurs in the bimetallic system.

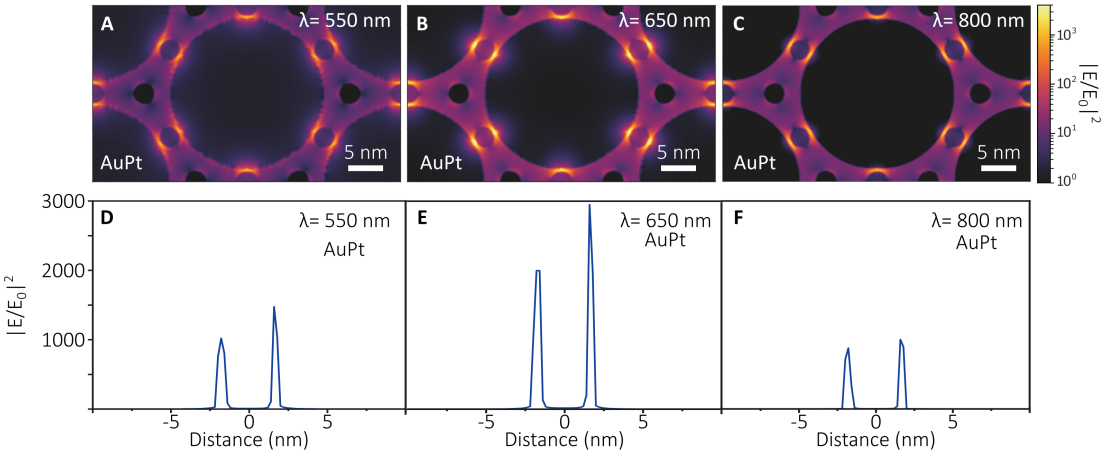

Figure 6.13: **E-field map in AuPt metasurface (A, B, C)** Electric field enhancement maps of the pure AuPt metasurface for different excitation wavelengths (550, 650 and 800 nm). Showing the different hotspot intensities. **(D, E, F)** Line scan of the electric field enhancement over the gap of two AuNSs containing a PtNP. The PtNP is not placed in the center of the AuNSs leading to an asymmetric enhancement profile.

Upon the inclusion of the PtNPs into the simulation, an overall increase on the intensity of the electric field of $\sim 10^3$ was seen at all the investigated wavelengths. Figure 6.13A-C display the lattice unit cell of the FDTD simulations, showing the PtNPs sitting in the strong hotspots of the AuNPs that are responsible for the enhancement and therefore for the high photocatalitic activity. Notably, a superior confinement is achieved at 650 nm (Fig. 6.12E). The intensity of the electric field at 650 nm was almost three times larger compared to the other wavelengths (Fig. 6.13D and F). Therefore, our simulations estimate a larger electric field enhancement at 650 nm for both Au and AuPt metasurface. The

electric field at the interparticle gap is dramatically enhanced by the presence of another metallic entity, such as PtNPs. The reduced gap plus the metallic behavoir of PtNPs, leads to an amplification of the electric field, reaching its largest value at 650 nm, in line with the experimental data. Interestingly, the H_2 generation rate at 800 nm was 1.6 times larger than at 550 nm, even though the absorbance at lower energy was negligible compared to the one at 550 nm (cf. Fig. 6.11). This further supports our interpretation on the fact that heat is not the main plasmonic contribution to the boosted PtNPs performance.

Finally, time-resolved absorption spectroscopy (also known as transient absorption spectroscopy, TA) is a very valuable tool to examine the evolution of an excited system [32]. Based in our interpretations, excited carriers on Pt generated upon the presence of intensified electric fields at the hotspots is the reason of the improved PtNPs performance in H_2 generation. To this end, the electronic dynamics of AuPt and Au metasurface, as well as the Pt control, were investigated employing TA spectroscopy. These results complemented the bulk wavelength-dependent experiments and optical simulations.

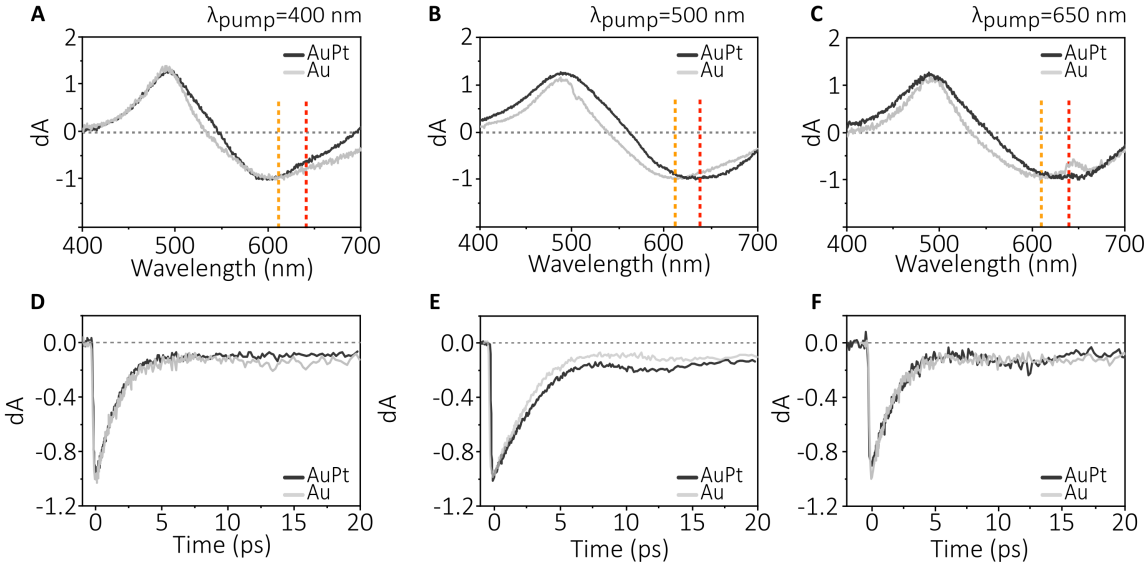

Figure 6.14: **Dynamics in Au (A, B, C)** Differential absorption spectra of Au (grey) and AuPt (black) supercrystals pumped at 400, 500, and 650 nm, respectively. Dashed lines represent probing wavelengths for each system. **(D, E, F)** Kinetics at probing wavelengths for Au and AuPt supercrystal when pumped at 400, 500 and 650 nm. The respective probe wavelengths correspond to the plasmon bleach, which allows tracking of the electron relaxation in AuNS. No difference is observed for the kinetics, implying no significant contribution of charge transfer between Au and Pt.

The resulting normalized TA spectra of both Au and AuPt metasurface, when pumped at λ =400, 500 and 650 nm, are shown in Fig. 6.14A-C. These wavelengths were selected because both samples presented a significant absorbance in that spectral region. The red ($\lambda = 610$ nm) and orange ($\lambda = 640$ nm) dashed lines correspond to the probing wavelengths for the kinetics in the Au and AuPt metasurface, respectively, matching what is known as

plasmon bleach. The plasmon bleach in each system allows to access to information about the relaxation of excited carriers in Au [180]. The normalized kinetics at the plasmon bleach when pumping at different wavelengths are displayed in Fig. 6.14D-F. Notably, if the excited carriers decay in Au and AuPt metasurfaces are compared, no changes are detected. This resemblance is mantained irrespective of the pumping wavelength. These results suggest that the decay of mainly interband transitions in Au is not affected by the presence of PtNPs in the system. Moreover, it also indicates the absence of significant Au-to-Pt charge transfer, even when exciting at 650 nm, wavelength at which the system performs best [79]. The similarities in the kinetics also enable to neglect the charge transfer through the conductive ITO substrate.

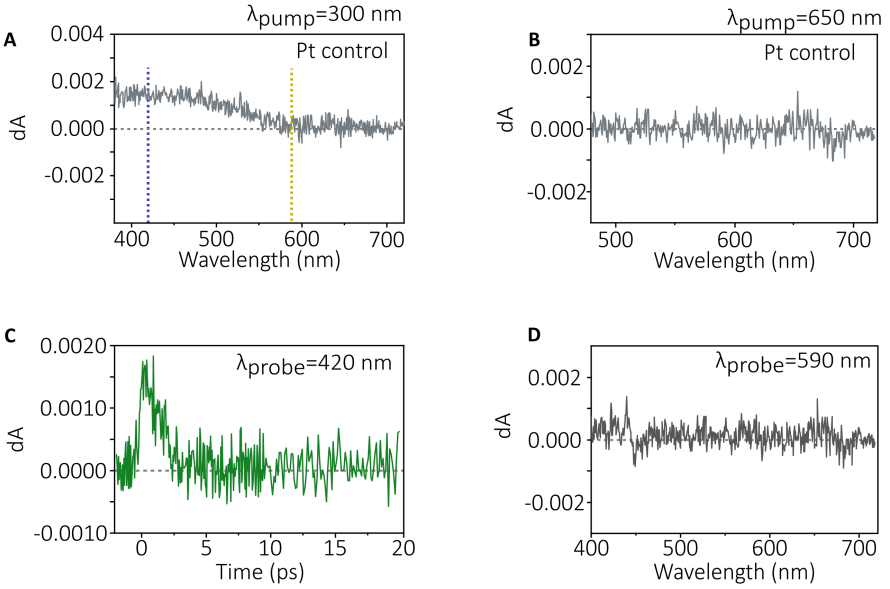

Figure 6.15: **TA control PtNPs (A, B)** Differential absorption for Pt control when pumped at 300 and 650 nm. While the sample absorbs at 300 nm, no excitation is seen at 650 nm. Dashed lines in A represent probing wavelengths when Pt control was pumped at 300 nm. **(C, D)** Kinetics at 420 and 590 nm, respectively upon excitation with 300 nm. Unlike 590 nm, it is possible to track the relaxation of excited charges on Pt at 400 nm.

Similarly, it is possible to assess the dynamics in the Pt and therefore confirm its activation. In this regard, we took an additional step to determine the spectral region in which Pt is active. The Pt control was obtained by drop-casting PSS functionalized PtNPs on a ITO. Figure 6.15A,B shows the differential absorption of the Pt control when pumped at 300 and 650 nm, respectively. It is clear that an activation of the PtNPs was observed when pumped with 300 nm due to the increasing contrast, and a complete lack of signal when Pt was excited at 650 nm. These results highlight that Pt by itself show a very weak interaction with photons of wavelengths in which the enlarged photocatalytic was observed for AuPt metasurface. The kinetics on PtNPs were tracked by pumping at

both 420 nm and 590 nm, blue and yellow dashed line in Figure 6.15A. As expected, only a signature of excited carriers is seen when probing at 400 nm. Therefore, the outcome is that the spectral region in which the decay of Pt nanoparticles can be tracked is in the blue.

After confirming the Pt active region, we proceeded investigating the activation of Pt-NPs, but now when integrated in the AuPt metasurface. Figure 6.16 present the dynamics of the AuPt metasurface when pumped at λ= 400, 500 and 650 nm. The differential absorption spectra are shown in Figure 6.14. The immediate onset of additional contrast in the Pt spectral region of the hybrid material only at 650 nm, when PtNPs experience the maximized electric field enhancement, points towards a direct excitation of Pt when the system (Fig. 6.16C). The fact that this larger contrast is only observed for the AuPt metasurface at wavelengths where more energy is channelled to the Pt is an indication of boosted *d-to-s* absorption processes induced by the strongly confined electric field. [80, 83, 133, 181]. This further supports the hypothesis that the electric fields at the hotspots drive the reaction.

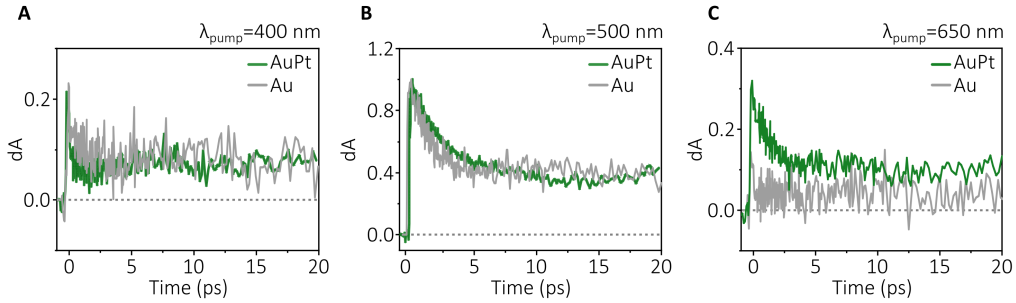

Figure 6.16: **Dynamics in Pt in metasurfaces. (A,B)** Kinetics on both Au and AuPt supercrystal when pumped at 400/500 nm and probed at 420 nm. No differences are observed between the kinetics, suggesting no Pt activation. **(C)** Significant difference was observed on the kinetics when pumping the AuPt supercrystal at 650 nm (wavelength at which larger E-field confinement is achieved) and probed at 420 nm. This suggest that Pt is activated as more energy is funneled to it.

All the evidence provided in this section points that by placing PtNPs at the inter-particle gap of hexagonally arrayed 22 nm AuNSs, it is possible to turn a catalyst with weak visible light absorption into a sunlight-type photocatalyst via boosted absorption, and thus activity [135, 182]. Indeed we find an enhanced catalytic activity with roughly doubled production under illumination and solar irradiances. The improved photoactivity is a consequence of the interaction of strongly confined electromagnetic fields (hotspots) with interstitial PtNPs. Charge injection into the catalytic center does not contribute significantly to the catalytic activity in these systems. This highlights the fact that enhanced near-fields can strongly contribute to improved plasmonic photocatalysis with bimetallic systems. To exploit the strong field enhancements in the hotspots of ordered plasmonic NP arrays, the catalytically active NPs must be placed into the interstices, thus enhancing their *d-to-s* transitions rate [133, 181]. Hence, in the accomplished bimetallic metasurface,

the AuNSs serve as antennas, confining the electromagnetic fields in the nanometer scale, whereas the PtNPs act as the catalytic center.

To prove possible that the extension of the concept to metasurfaces is possible using AuNS of different sized, 39 nm AuNS were assembled to the same PtNPs. A representative TEM image of a monolayer domain is displayed in Figure 6.17A, while its performance in dark and light is shown in Figure 6.17B. A larger enhancement on the reaction rate was obtained by the AuPt metasurface due to the an increase in the size of the plasmonic component. Although a systematic study should be conducted, based on our results it might be due to the larger field enhancements achieved by larger particles in comparison wiht smaller ones. Thus, further boosting the absorption in PtNPs. This result strongly reflects the tunability of these structures and the set of tools that can be tailored towards desired functionalities.

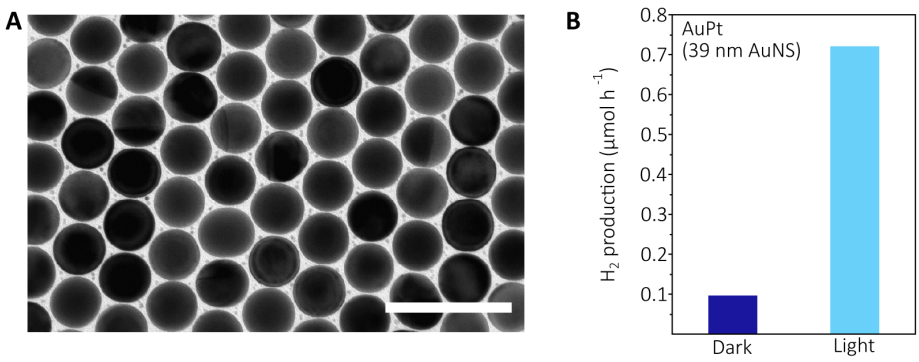

Figure 6.17: **Metasurfaces with tunable sizes (A)** TEM of a AuPt monolayer in which 39 nm AuNS were employed as plasmonic components, while using the same Pt NPs as a reactor. **(B)** Photocatalytic performance of for H_2 generation. A larger enhancement was achieved. showing the potential of these platforms towards photocatalytic processes.

Conclusions

In our study, we introduce plasmonic bimetallic metasurface with desired antenna-reactor configuration attained from colloidal suspension. The size of the metasurface can be extended up to several square millimeters maintaining the configuration and mono-, bi- and multilayers domains can be achieved. This methodology allows the tunability of parameters such as AuNS diameter, gap sizes, and PtNP loading. We prove the synergistic effect of plasmonic-catalytic components in metasurfaces by observing a two-fold increase in H_2 production at solar irradiances, achieving slightly higher H_2 generation rates than the best performers for this H_2 carrier. The well-defined metasurface allowed to discriminate between plasmonic contributions to the catalytic enhancement, revealing that the intensity of the electromagnetic fields at the hotspots dictates the PtNPs performance, whereas thermal contributions or charge injection from AuNS into the catalytic center seem to play a minor role.

We believe that the rational design of two-dimensional bimetallic structures will play an important role in sunlight to chemical energy conversion processes. Our findings suggest that it is possible to energize materials by manufacturing plasmonic-catalytic metasurface, achieving better catalytic performances. Therefore, the large set of variables offer by this particular system allows to fabricate opto-catalytic structures with functionalities which can be tailored according to specific target reaction, showing the potential of these 2D metasurfaces towards solar energy transduction.

Chapter 7

Conclusions and Outlook

The investigations carried out this thesis aim to pave the way for the design of future plasmonic bimetallic photocatalysts. As was mentioned in the introduction, in order to create a photocatalyst capable of efficiently conducting light-to-chemical energy transduction, it was essential to understand how the materials interacted. Our findings indicate that, opposite to what might seem counter-intuitive at first, a catalytic metal benefits more from the excitation of LSPR in plasmonic antennas when it is placed in close proximity, in comparison to when an interface is created among them.

The creation of an interface between the plasmonic and catalytic components is a crucial factor dictating the optical and thermal behaviour of this type of bimetallic photocatalyst. A new plasmon dissipation pathway is made possible by the plasmonic NPs' capacity to inject excited carriers into the catalytic reactive center. This new physical phenomenon is detrimental for the overall optical properties, since it weakens the resonant interaction with light, resulting in a poorer overall absorption and lower heat generation.

Conversely, by positioning the catalytic reactor adjacent to the optical antenna, one may engineer the components to avoid the contact. In this configuration, several distinct effects are observed. If one analyzes the spectral features of the bimetallic NPs with regard to the plasmonic, no major changes are observed, meaning that the resonant behavior is mostly preserved. This translates as a similar light-to-heat conversion efficiency. However, the formation of optical hotspots appears to be the most crucial element. A greater electric field confinement is seen as a result of this sub-nanometer separation between a plasmonic antenna and a catalytic reactor. The interaction of the intense electric field and catalytic reactor yields the generation of excited carriers within the catalytic metal. Hence, we can understand the optical hotspots as a chemical hotspots in which a large excited carriers density can be achieved.

As vastly discussed throughout the past chapters, both excited carriers and temperature can facilitate a chemical transformation. Nevertheless, it is important to highlight that when illuminating the bimetallic photocatalyst with solar irradiances, the temperature does not appear to be the main factor driving the reaction. Instead, the chemical hotspots enable to accomplish a larger enhancement in reaction rates, owing to their ability to boost the absorption of light in the catalytic metal at using sunlight irradiances and frequencies.

We proved the relevance of the hotspots by positioning catalytic NPs in the interstices of a 2D hexagonal array of plasmonic nanoparticles. As a result of the substantial hotspot density offered by the repetitive structure, we obtained a H_2 generation rate comparable to the best performers when using formic acid as a H_2 carriers. This important result was obtained employing very low amounts of catalytic material (typically expensive) and solar irradiances, showing the potential of these hybrid 2D structures.

The results obtained in the course of this thesis provide insight in the fabrication of bimetallic plasmonic nanocatalyst for efficient light to chemical energy conversion. Knowing that chemical hotspots have a significant impact on energy flow, one can envision that the next step will be the development of structures based on earth-abundant plasmonic elements (Al, Cu, Mg) that can supply the necessary large hotpots density so that catalytic metals exploit them to drive chemical reactions. Future developments are expected to establish these photocatalysts to be a key player in the clean and sustainable energy quest, given the consistent growth that Plasmonic Catalysis has demonstrated so far.

Appendix A

7.1 Drude Model

In order to understand the phenomenon of localized plasmon resonances (LSPR), first we need to comprehend how do materials interact with an external periodic force, such as the electromagnetic waves. This analysis resembles to the damped oscillator with a driving force and is known as *Lorentz model* for polarizability [20]. To a broad description we refer the readers to references [20] and [19].

The phenomenon can be described taking into account all forces acting in the system. We consider a molecule at which electrons oscillate with a natural frequency ω_0. When displaced by the electric force, the electrons feel a restoring force exerted by the nuclei, which is proportional to their displacement as though they were held by a spring (Hooke's Law). In addition, the inherent damping force corresponding to resistance to the motion is considered. The damping force is proportional to the velocity of the electrons.

$$\Sigma F = ma = qE - \gamma v - kx \tag{7.1}$$

$$qE = m\frac{d^2x}{dt^2} + \gamma\frac{dx}{dt} + m\omega_0^2 x \tag{7.2}$$

If the electric field ($E(t)$) acting on the electrons varies sinusoidally with the time, it could be written as:

$$E = E_0 \exp^{i\omega t} \tag{7.3}$$

and electron will then be displaced with the same frequency, so we can write the displacement ($x(t)$) and the first and second derivative can be written as:

$$x(t) = x_0 \exp^{i\omega t}; \quad \frac{dx}{dt} = i\omega x_0 \exp^{i\omega t}; \quad \frac{d^2x}{dt^2} = -\omega^2 x_0 \exp^{i\omega t} \tag{7.4}$$

replacing this terms in equation 7.2, it is found that the displacement is proportional to the external electric field

$$x(t) = \frac{q/m}{((\omega_0^2 - \omega^2) - i\gamma\omega)} E(t) \tag{7.5}$$

We can then find the polarizability (α) of the molecule, as it is the proportion between the induced dipole (p) and the electric field (E)

$$p = qx = \frac{q^2/m}{((\omega_0^2 - \omega^2) - i\gamma\omega)}E \tag{7.6}$$

$$\alpha(\omega) = \frac{q^2/m}{((\omega_0^2 - \omega^2) - i\gamma\omega)} \tag{7.7}$$

This expression can be extended to a medium by considering a density of molecules per volume unit (n=N/V)

$$P = np = n\frac{\alpha(\omega)}{\varepsilon_0}E \tag{7.8}$$

So far, we found that the polarizability ($\alpha(\omega)$) depends on the frequency of the driving Electric field. It would be also beneficial to understand how the electromagnetic waves propagates throughout the material. Lets start describing it in a general way for a dielectric and continue for metals and the different regimes.

In order to know how a wave propagates through a media, Maxwells equations must be solved in the material. By taking the ρ =- $\nabla \cdot \vec{P}$ and j= $\partial\vec{P}/\partial t$, the equations then become

$$\nabla \cdot E = -\frac{\nabla \cdot P}{\varepsilon_0} \tag{7.9}$$

$$c^2\nabla \times \vec{B} = \frac{\partial}{\partial t}(\frac{\vec{P}}{\varepsilon_0} + \vec{E}) \tag{7.10}$$

$$\nabla \times \vec{E} = -\frac{\partial \vec{B}}{\partial t} \tag{7.11}$$

$$\nabla \times \vec{B} = 0 \tag{7.12}$$

By using some well-known algebra, we arrive to a combined equation depending only on $\vec{E}$ and $\vec{P}$

$$\nabla^2\vec{E} - \frac{1}{c^2}\frac{\partial^2\vec{E}}{\partial t^2} = -\frac{1}{\varepsilon_0}\nabla(\nabla \cdot \vec{P}) + \frac{1}{\varepsilon_0 c^2}\frac{\partial^2\vec{P}}{\partial t^2} \tag{7.13}$$

The expression in equation 7.13 show that the Dalembertian of $\vec{E}$, is equal to two terms involving the polarization $\vec{P}$, which also depends on $\vec{E}$, as shown in equation 7.8. In isotropic dielectrics, P is always in the same direction than E. Now, if E is a wave travelling in z-direction and polarized in x, then $\vec{E}$ has only an x component

$$E_x = E_0 \exp i(\omega t - kz) \tag{7.14}$$

The exponent can be rewritten as in equation XX, representing a wave travelling in z with a speed v_{phase}= ω/k

$$-ik = (z - \frac{\omega}{k}t) \Rightarrow v_{phase} = \frac{\omega}{k} \tag{7.15}$$

The refractive index is then defined as the ratio between the speed of light in vacuum and the speed of propagating light in a medium

$$\eta = \frac{c}{v_{phase}} \Rightarrow \eta = \frac{kc}{\omega} \tag{7.16}$$

In this particular case, equation 7.13 is reduced to

$$-k^2 E_x + \frac{\omega^2}{c^2} E_x = -\frac{\omega^2}{\varepsilon_0 c^2} P_x \tag{7.17}$$

And by substituting $\mathrm{P}_x = \frac{n\alpha(\omega)}{\varepsilon_0} E_x$, it is found that

$$k^2 = \frac{\omega^2}{c^2}(1 + n\frac{\alpha(\omega)}{\varepsilon_0}) \Rightarrow \eta = 1 + n\frac{\alpha(\omega)}{\varepsilon_0} \tag{7.18}$$

And now, substituting by the expression that we found for the $\alpha(\omega)$, we find an important parameter that dictates how waves propagate within a medium

$$\eta^2 = 1 + \frac{q^2}{m\varepsilon_0((\omega_0^2 - \omega^2) - i\gamma\omega)} \tag{7.19}$$

The expression for the refractive index of a medium presented in 7.19 is valid for many substances. However, metals are understood as a network of positive ions bound by the valence electrons, which are freely moving across the structure. This definition implies that they are no longer bound to their respective atoms and, thus, they do not have any natural frequency (ω_0=0). Therefore, the refractive index of metals is given by

$$\eta^2 = 1 - \frac{\omega_p^2}{(\omega^2 + i\gamma\omega)} \tag{7.20}$$

The quantity $\omega_p = \mathrm{nq}_{el}^2/\mathrm{m}_{el}\varepsilon_0$ is known as the plasma frequency and is a reference value for interaction between the electromagnetic waves and the free electrons of metals. For $\omega < \omega_p$ the index of a metal has an imaginary part and waves are attenuated inside the metal. However, for $\omega >> \omega_p$, the metals becomes transparent. This model predicts reasonably well

Bear in mind that this is a classical approach and some metals lose their transparency within the UV, where photoelectron emission take place.

Now, it is possible to deduce an expression for the dielectric function of metals $\varepsilon(\omega)$.

$$\eta^2(\omega) \approx \varepsilon(\omega) = 1 - \left(\frac{\omega_p}{\omega}\right)^2 \tag{7.21}$$

Appendix B

7.2 Chemicals

Gold (III) chloride trihydrate ($HAuCl_4.3H_2O$, ⩾99.9%), sodium tetrachloropalladate (II) (Na_2PdCl_4, ⩾99.9%), potassium tetrachloropalladate (II), (K_2PdCl_4, ⩾99.9%), ascorbic acid (AA, ⩾99.0%), sodium borohydride ($NaBH_4$, ⩾98%), cetyl-trimethyl ammonium bromide (CTAB, ⩾99.0%), cetyl-trimethyl chloride (CTAC, 25 wt.% in water), tetraethylorthosilicate 98% (TEOS), ammonium hydroxide solution (NH_4OH, 27% in water), poly(allylamine hydrochloride) (PAH, M_W:17,500), sodium chloride (NaCl, 99%), polyvinylpyrrolidone (PVP, M_W:10,000), formic acid (FA) and absolute ethanol (EtOH) were all purchased from Sigma-Aldrich and used without further purification. Chloroplatinic acid solution (8% wt. in H_2O), sodium citrate trihydrate (≥ 99%), and indium tin oxide (ITO) coated glass slides (surface resistivity 8-12 Ω cm^{-2}) were from Sigma-Aldrich (USA). Toluene (≥ 99.5 %), tetrahydrofuran (≥ 99.5 %) was purchased from VWR (USA). Diethylene glycol (DEG, reagent grade) was from Merck (Germany). Thiolated polystyrenes (PSSH, PSSH2k: M_N = 2000 g/mol, M_W = 2300 g mol^{-1}; PSSH5k: M_N = 5300 g mol^{-1}, M_W = 5800 g mol^{-1}; PSSH10k: M_N = 11500 g mol^{-1}, M_W = 12400 g mol^{-1}) were from Polymer Source (Canada). All reagents were used without further treatment. H_2 standards (100, 500 and 1000 ppm) were purchased from Linde Gas. Ultrapure water with resistivity of 18 MΩ cm was used in all experiments.

In all experiments, we used ultrapure water with a resistivity of 18,2 MΩ cm.

Synthesis of 60 nm AuNS The AuNS synthesis was performed modifying the seed-mediated growth method described by Zheng et al. [99]. These modifications were introduced in order to enlarge the production and favor the reproducibility of photocatalysis experiments.

Au clusters preparation The initial Au clusters were formed by reducing 10 mL of an aqueous solution containing $HAuCl_4$ (0.25 mM) and CTAB (0.1 M) with 600 μL of a freshly prepared 10 mM $NaBH_4$ solution. The solution turns brownish within seconds indicating clusters formation. The clusters are kept undisturbed for 3 h at 27 °C.

10 nm AuNS synthesis In a 20 mL glass vial, 4 mL of a 200 mM CTAC solution and 3 mL of a 100 mM Ascorbic Acid (AA) solution were mixed, followed by the addition of 100

μL of previously prepared CTAB capped Au clusters. After the solution was stirred at 300 rpm and left at 27 °C for 10 min, 4 mL of 0.5 mM $HAuCl_4$ were added in a quick one-shot injection. The resulting 10 nm Au spheres were centrifuged twice at 13400 rpm for 30 min and finally redispersed in 1 mL of a 20 mM CTAC solution. These nanoparticles were used as seeds for further growing steps.

Growth of AuNS In order to reach the desired size, 200 mL of a 100 mM CTAC solution were mixed with 1.3 mL of a 100 mM AA solution and seeds of 10 nm AuNS solution (for volumes check Table). The whole solution was kept stirred at 800 rpm at 27 °C for 20 min. Then, 10 mL of 10 mM $HAuCl_4$ were pumped in at a rate of 20 mL h^{-1} and once the pumping completed, is left stirring for 30 min. Even though this rate is 10 times larger than the reference, it still yields 61 nm ± 1.5 nm smooth sphere-like NPs (Supplementary Fig. 1). After undergoing two centrifugation-redispersion cycles the AuNS were finally redispersed in 35 mL of mQ H_2O and used for the synthesis of bimetallic nanoparticles.

Sample	V_{seeds} (μL)	Centriguation (rpm)	Time (min)
22 nm AuNS	550	6000	10
60 nm AuNS	250	4000	10
67 nm AuNS	225	4000	10

Table 7.1: Volumes for precursors solutions in Au@Pd and Au@AuPd core-shell NPs

Synthesis of Au@Pd and Au@AuPd Core-Shell NPs The CS NPs were synthesized by a quick reduction of Pd and Au precursors on top of the previously prepared AuNS. Firstly, as the precursors have different reduction potentials and thus, different reductio rate, a ligand exchange was carried out [102]. The precursors solutions (Table 7.2) were kept at 90 °C for 60 min. Secondly, 1.7 mL of an aqueous solution containing $\sim 7.5\times10^{11}$ AuNS (60 and 67 nm) were added at 90 °C, followed by the quick injection of 1 mL of 100 mM AA solution. The solutions immediately turned purple and were left at 900 °C for another 60 min. Subsequently, two centrifugation-redispersion cycles (3000 rpm for 10 min) were carried out.

Catalyst	H_2O	CTAC (25 wt%)	CTAB (0.2 M)	K_2PdCl_4 (10 mM)	$HAuCl_4$ (10 mM)
Au@Pd	13.96 mL	1.785 mL	2.30 mL	400 μL	-
Au@AuPd	9 mL	-	9 mL	75 μL	75 μL

Table 7.2: Volumes for CS NPs presented in Chapter 4

To obtain a thicker Pd shell deposited on AuNS, the number of 67 nm AuNS was decreased from 7×10^{11} to 6×10^{11}, resulting in a increase from 2 to 4 nm Pd shell.

Synthesis of Pd satellites PVP-stabilized Pd nanoparticles (Pd NPs) were synthesized according to a method described in the literature with slight modifications [183] . Briefly, an aqueous solution (45 mL) containing PVP (1.05 mM) and AA (4.25 mM) was heated up to 100 °C under reflux for 10 min. Subsequently, an aqueous solution (5.0 mL) containing Na_2PdCl_4 (10 mM) was added. The reaction was allowed to continue at 100 °C for 3 h to obtain Pd NPs.

Synthesis of Au-Pd satellites PVP-stabilized Au-Pd Nanoparticles (AuPd NPs) were synthesized in an aqueous solution (40 mL) containing PVP (1.05 mM) and AA (4.25 mM) was placed in a three-neck flask fitted with a condenser and refluxed at 100 °C for 10 min. Subsequently, a mixture containing 5.0 mL Na_2PdCl_4 (10 mM) and 5.0 mL $HAuCl_4$ (10mM) were added in a quick one-shot injection. The reaction was allowed to continue at 100 °C for 3 h to obtain a dark brown solution.

Synthesis of Au-Pd and Au-AuPd core-satellites 1.4 mL of absolute ethanol are added to 2.77 mL of a 2.72×10^{14} AuNS/L aqueous solution, followed by the addition of 350 μL of non-washed PVP-AA capped satellites (Methods). The solution turns purple within seconds indicating the self-assembly occurrence. After stirring the solution at 400 rpm for 30 min, it is washed in low-binding DNA eppendorf tubes four times at 4000, 3500 and 3000 rpm for 20 min, respectively.

Synthesis of PtNPs PtNPs with 2.8 ± 0.5 nm in diameter were synthesized as follows: 500 μL of H_2PtCl_{6a} 0.05 M were added to 8.6 mL of ultra-pure water (stirred at 500 rpm), succeeded by the addition of 500 μL of sodium citrate 0.1 M, which served as the stabilizing agent. The Pt precursor was reduced upon quick addition of 500 μL of $NaBH_4$ (0.015 M), evidenced by the dark brown color of the final solution. Finally, the solution was left undisturbed for 10 minutes [184].

The as-synthesized PtNPs were functionalized with PSSH2k by phase transfer as described in a previous report [185]. In detail, the aqueous PtNPs dispersion (1000 μL) was mixed with PSSH2k (1100 μL, 0.18 mM) in toluene and ethanol (1000 μL). After vigorous shaking, phase separation was facilitated by addition of some mg sodium chloride. The toluene phase with the PtNPs was then carefully removed and used for self-assembly experiments without further purification. The PtNPs had a diameter of 2.7 ± 0.6 nm and the platinum concentration in the final dispersion in toluene was 9.6 mg/L corresponding to 65 nM particle concentration.

Self-Assembly Self-assembly of pure and mixed samples of polystyrene-functionalized NPs took place on DEG as a liquid subphase as described previously [93, 186]. Different volume ratios of AuNS@PSSH and PtNP@PSSH2k were pipetted onto the DEG and the sample cell covered was with glass cover slip to slow down the evaporation of the toluene. After 16-24 h crystalline films had formed, which were carefully skimmed of with TEM grids or transferred to ITO substrates for catalysis experiments. Crystalline films with

2D-hexagonal symmetry and incorporated PtNPs formed with all tested conditions. The samples differed in platinum loading and resulting interparticle spacing. For the controls just AuNS@PSSH or just PtNP@PSSH2k were used accordingly.

Appendix C

7.2.1 Temperature modelling of core@shell nanoparticles

The temperature field T(r) of core@shell NPs can be calculated using the heat diffusion equation. Therefore, for a system in which core is material 1, shell is material 2 and the surrounding medium is material 3, the solutions with radial symmetry in the steady states reads:

$$-\kappa\frac{1}{r^2}\partial r(r^2\partial rT) = q \tag{7.22}$$

r<b (core)

$$T(r) = -\frac{-q_1}{6\kappa_1}r^2 + \frac{c_0}{r} + c_1 \tag{7.23}$$

(core) b<r<a (shell)

$$T(r) = -\frac{-q_2}{6\kappa_2}r^2 + \frac{c_2}{r} + c_3 \tag{7.24}$$

r>a

$$T(r) = -\frac{c_4}{r} + c_5 \tag{7.25}$$

where c_0 to c_5 are integration constants. c_5=T(∞)=T_0 with T_0 equal the room temperature. Non divergence at T(0)leads to c_0=0. The others four constant can be obtained from the following boundary conditions.

1- Energy conservations demands that the integrated heat flux J crossing interface 2-3 should be equal to the absorbed heat Q by the NP.

$$4\pi a^2|J(a^+)| = Q \tag{7.26}$$

Using J(r)= $\kappa\nabla$T(r) leads to

$$C_4 = \frac{Q}{4\pi\kappa_3} \tag{7.27}$$

2- Heat flux conservation at the interface 2-3

$$|J(a^-)| = |J(a^+)| \tag{7.28}$$

Leads to

$$c_2 = \frac{\kappa_3}{\kappa_2} c_4 - \frac{q_2 a^3}{3\kappa_2} \tag{7.29}$$

3- Temperature boundary condition at the interface 2-3

$$T(a^-) - T(a^+) = |J(a^+)| R^{th}_{2-3} \tag{7.30}$$

R^{th}_{2-3} is the Kapitza interfacial thermal resistance between materials 2 and 3. This leads to

$$c_3 = \frac{\kappa_3 R^{th}_{2-3} c_4}{a^2} + \frac{c_4}{a} + \frac{q_2 a^2}{6\kappa_2} - \frac{c_2}{a} + T_0 \tag{7.31}$$

4- Temperature boundary condition at the interface 1-2

$$T(b^-) - T(b^+) = |J(b)| R^{th}_{1-2} \tag{7.32}$$

Using $4\pi\ \mathrm{b}^2\ J(\mathrm{b}) = \frac{4}{3}\ \pi\ \mathrm{b}^3\ \mathrm{q}_1$, leads to

$$c_1 = \frac{1}{3} q_1 b R^{th}_{1-2} + c_3 + \frac{c_2}{b} + \frac{q_1 b^2}{6\kappa_1} - \frac{q_2 b^2}{6\kappa_2} \tag{7.33}$$

The model was extracted from [156].

Appendix D

7.3 Quantifying metallic loads in Au and AuPt metasurfaces

Aware of potential losses during photocatalytic experiments, an optical microscope was used to monitor the losses (Table 7.3) and adjust the H_2 generation rate in each round of experiments.

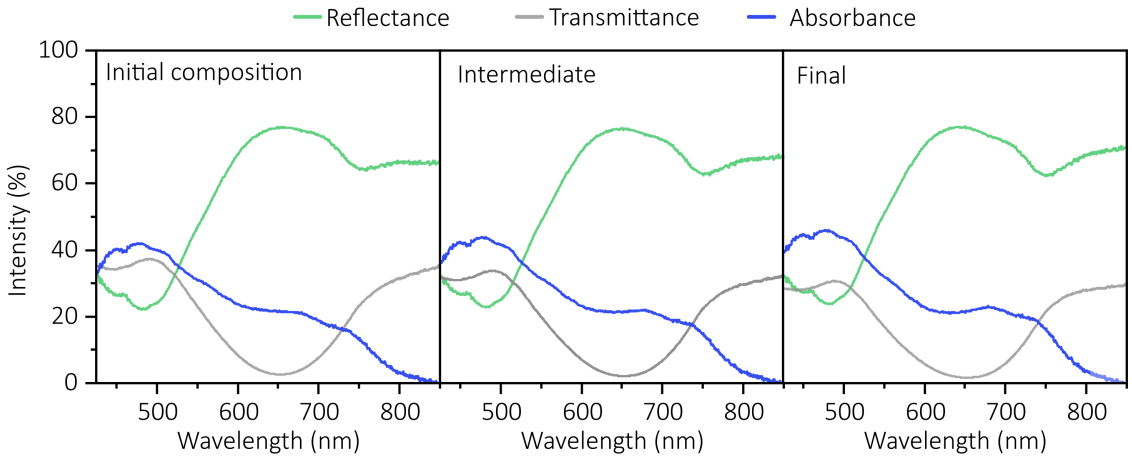

Figure 7.1: **Material Losses**. Comparison of the optical response (reflectance, transmission and absorbance) of the AuPt meatasurface between the catalysis experiments. Showing the calculated optical response of the initial composition, an intermediate one and the final. It shows that the material loss did not change the total optical behavior of the sample.

Figure 7.1 shows the weighted reflectance (green), transmittance (grey) and absorbance (blue) of the AuPt metasurface. The spectra were acquired prior to its use in photocatalysis (initial), in an intermediate stage in which some photocatalytic experiments were conducted, and at the very end of our experiments (final). The initial composition was

already presented in Figure 6.7B for this system. As can be observed from their comparison, irrespective of the extensive use in catalysis, the overall features of their optical behaviour were not heavily modified. When comparing the final composition with respect to the initial composition, the shoulder containing the polaritonic modes was slightly more noticeable, suggesting that across the experiments, the sample presented a very behaved optically the same.

It was not until the end of the experiments that the metallic loads were quantified, so below we present the procedures employed to quantify the mass at each of the stages mentioned above. The total mass of the catalysts was determined employing ICP-MS at the end of experiments. Results are shown in Table 7.4.

Table 7.3: Losses estimation on photocatalytic experiments in AuPt supercrystal, determined by using an optical microscope in transmisstion mode using the different clue colors to distinguish between the different thicknesses.

Au-Pt Supercrystal	Initial	Intermediate	Final
Monolayer (1L)	8.3 mm^2 (60.7 %)	3.8 mm^2 (48.8 %)	1.5 mm^2 (36.5 %)
Bilayer (2L)	1.3 mm^2 (9.6 %)	1.2 mm^2 (15.2 %)	0.9 mm^2 (22.3 %)
Multilayer (3L+)	4.1 mm^2 (29.7 %)	2.8 mm^2 (36.0 %)	1.7 mm^2 (41.2 %)
Total	13.7 mm^2	7.8 mm^2	4.2 mm^2

Table 7.4: Total catalyst mass determined by ICP-MS

Sample	Au mass	Pt mass
Au supercrystal	2.6 μg	-
AuPt supercrystal	3.5 μg	4.2 ng
Pt control	-	23.6 ng

Table 7.5: Pt total mass estimation in AuPt supercrystal combining TEM and microabsorbance estimations

AuPt surface	Initial (Mass x Area)	Intermediate (Mass x Area)	Final (Mass x Area)
Monolayer (1L)	8.8 ng	4.0 ng	1.6 ng
Bilayer (2L)	2.7 ng	2.5 ng	1.9 ng
MultiLayer (3L+)	12.9 ng	8.9 ng	5.4 ng
Total	24.4 ng	15.4 ng	8.9 ng

Additionally, to estimate the mass lost in each step, the mass of both Au and Pt per mm^2 were estimated from a metasurface's monolayer TEM image as follows:

$$m_{Au-sphere} = V_{Au-sphere} \times \rho_{Au} = \frac{4\pi r^3_{Au-sphere}}{3} \times \rho_{Au} \tag{7.34}$$

$$m_{Pt-sphere} = V_{Pt-sphere} \times \rho_{Pt} = \frac{4\pi r_{Pt-sphere}^3}{3} \times \rho_{Pt} \tag{7.35}$$

$$\begin{aligned}
&\text{Au mass per 1L mm}^2 = \frac{N \times m_{Au-sphere}}{\text{Area}} = 0.185\ \mu\text{g Au mm}^{-2} \\
&\text{Au mass per 2L mm}^2 = 2 \times \text{Au mass per 1L mm}^2 = 0.370\ \mu\text{g Au mm}^{-2} \\
&\text{Au mass per 3L+ mm}^2 = 3 \times \text{Au mass per 1L mm}^2 = 0.555\ \mu\text{g Au mm}^{-2}
\end{aligned} \tag{7.36}$$

$$\begin{aligned}
&\text{Pt mass per 1L mm}^2 = \frac{N \times m_{Pt-sphere}}{\text{Area}} = 1.1\ \text{ng Pt mm}^{-2} \\
&\text{Pt mass per 2L mm}^2 = 2 \times \text{Pt mass per 1L mm}^2 = 2.1\ \text{ng Pt mm}^{-2} \\
&\text{Pt mass per 3L+ mm}^2 = 3 \times \text{Pt mass per 1L mm}^2 = 3.2\ \text{ng Pt mm}^{-2}
\end{aligned} \tag{7.37}$$

The total mass was then estimated multiplying the mass of Pt per mm^2 by the corresponding area, presented in Table 7.3.

Table 7.6: Au total mass estimation in AuPt supercrystal combining TEM and microabsorbance estimations

AuPt surface	Initial (Mass x Area)	Intermediate (Mass x Area)	Final (Mass x Area)
Monolayer (1L)	1.53 μg	0.7003 μg	0.278 μg
Bilayer (2L)	0.49 μg	0.444 μg	0.333 μg
MultiLayer (3L+)	2.27 μg	1.554 μg	0.944 μg
Total	4.29 μg	2.702 μg	1.555 μg

A similar analysis was conducted for Au supercrystal, shown in Equations 7.38 and Supplementary Table 7.7.

$$\begin{aligned}
&\text{Au mass per 1L mm}^2 = \frac{N \times m_{Au-sphere}}{\text{Area}} = 0.07\ \mu\text{g Au mm}^{-2} \\
&\text{Au mass per 2L mm}^2 = 2 \times \text{Au mass per 1L mm}^2 = 0.13\ \mu\text{g Au mm}^{-2} \\
&\text{Au mass per 3L+ mm}^2 = 3 \times \text{Au mass per 1L mm}^2 = 0.20\ \mu\text{g Au mm}^{-2}
\end{aligned} \tag{7.38}$$

Table 7.7: Au total mass estimation in Au supercrystal combining TEM and optical microscope estimations

AuPt surface	Initial (Mass x Area)	Final (Mass x Area)
Monolayer (1L)	0.97 μg	0.37 μg
Bilayer (2L)	0.37 μg	0.10 μg
MultiLayer (3L+)	1.25 μg	0.09 μg
Total	1.44 μg	0.55 μg

Bibliography

[1] H. Ritchie, M. Roser, and P. Rosado, "Energy," *Our World in Data*, 2022. https://ourworldindata.org/energy.

[2] H. H. Cho, V. Strezov, and T. J. Evans, "A review on global warming potential, challenges and opportunities of renewable hydrogen production technologies," *Sustainable Materials and Technologies*, p. e00567, 2023.

[3] H. Ritchie, M. Roser, and P. Rosado, "Co_2 and greenhouse gas emissions," *Our world in data*, 2020.

[4] A. A. Lacis, G. A. Schmidt, D. Rind, and R. A. Ruedy, "Atmospheric co2: Principal control knob governing earth's temperature," *Science*, vol. 330, no. 6002, pp. 356–359, 2010.

[5] H. Ritchie, M. Roser, and P. Rosado, "Co2 and greenhouse gas emissions," *Our World in Data*, 2020. https://ourworldindata.org/co2-and-other-greenhouse-gas-emissions.

[6] E. Papadis and G. Tsatsaronis, "Challenges in the decarbonization of the energy sector," *Energy*, vol. 205, p. 118025, 2020.

[7] I. E. Agency, "Net zero by 2050," *License: CC BY 4.0*, 2021. https://www.iea.org/reports/net-zero-by-2050.

[8] J. R. Adleman, D. A. Boyd, D. G. Goodwin, and D. Psaltis, "Heterogenous catalysis mediated by plasmon heating," *Nano letters*, vol. 9, no. 12, pp. 4417–4423, 2009.

[9] P. Christopher, H. Xin, and S. Linic, "Visible-light-enhanced catalytic oxidation reactions on plasmonic silver nanostructures," *Nature chemistry*, vol. 3, no. 6, pp. 467–472, 2011.

[10] S. Linic, P. Christopher, and D. B. Ingram, "Plasmonic-metal nanostructures for efficient conversion of solar to chemical energy," *Nature materials*, vol. 10, no. 12, pp. 911–921, 2011.

[11] S. Mukherjee, F. Libisch, N. Large, O. Neumann, L. V. Brown, J. Cheng, J. B. Lassiter, E. A. Carter, P. Nordlander, and N. J. Halas, "Hot electrons do the impossible:

plasmon-induced dissociation of h2 on au," *Nano letters*, vol. 13, no. 1, pp. 240–247, 2013.

[12] J. M. P. Martirez, J. L. Bao, and E. A. Carter, "First-principles insights into plasmon-induced catalysis," *Annual Review of Physical Chemistry*, vol. 72, pp. 99–119, 2021.

[13] V. Jain, R. K. Kashyap, and P. P. Pillai, "Plasmonic photocatalysis: Activating chemical bonds through light and plasmon," *Advanced Optical Materials*, vol. 10, no. 15, p. 2200463, 2022.

[14] U. Aslam, V. G. Rao, S. Chavez, and S. Linic, "Catalytic conversion of solar to chemical energy on plasmonic metal nanostructures," *Nature Catalysis*, vol. 1, no. 9, pp. 656–665, 2018.

[15] S. Linic, S. Chavez, and R. Elias, "Flow and extraction of energy and charge carriers in hybrid plasmonic nanostructures," *Nature Materials*, pp. 1–9, 2021.

[16] S. A. Maier, *Plasmonics: fundamentals and applications*, vol. 1. Springer.

[17] P. Biagioni, J.-S. Huang, and B. Hecht, "Nanoantennas for visible and infrared radiation," *Reports on Progress in Physics*, vol. 75, no. 2, p. 024402, 2012.

[18] V. N'Tsame Guilengui, L. Cerutti, J.-B. Rodriguez, E. Tournié, and T. Taliercio, "Localized surface plasmon resonances in highly doped semiconductors nanostructures," *Applied Physics Letters*, vol. 101, no. 16, p. 161113, 2012.

[19] C. F. Bohren and D. R. Huffman, *Absorption and scattering of light by small particles*. John Wiley & Sons, 2008.

[20] R. Feynman, *The Feynman Lectures on Physics Vol ll*. Narosa, 1986.

[21] S. Hofmann, *Auger-and X-ray photoelectron spectroscopy in materials science: a user-oriented guide*, vol. 49. Springer Science & Business Media, 2012.

[22] J. B. Khurgin, "How to deal with the loss in plasmonics and metamaterials," *Nature nanotechnology*, vol. 10, no. 1, pp. 2–6, 2015.

[23] S. Schlücker, "Surface-enhanced raman spectroscopy: Concepts and chemical applications," *Angewandte Chemie International Edition*, vol. 53, no. 19, pp. 4756–4795, 2014.

[24] C. F. Bohren, "How can a particle absorb more than the light incident on it?," *American Journal of Physics*, vol. 51, no. 4, pp. 323–327, 1983.

[25] K. L. Kelly, E. Coronado, L. L. Zhao, and G. C. Schatz, "The optical properties of metal nanoparticles: the influence of size, shape, and dielectric environment," 2003.

[26] P. Camargo and E. Cortés, *Plasmonic Catalysis: From Fundamentals to Applications*. Wiley, 2021. ISBN: 978-3-527-34750-6.

[27] A. M. Brown, R. Sundararaman, P. Narang, W. A. Goddard III, and H. A. Atwater, "Nonradiative plasmon decay and hot carrier dynamics: effects of phonons, surfaces, and geometry," *ACS nano*, vol. 10, no. 1, pp. 957–966, 2016.

[28] M. L. Brongersma, N. J. Halas, and P. Nordlander, "Plasmon-induced hot carrier science and technology," *Nature nanotechnology*, vol. 10, no. 1, pp. 25–34, 2015.

[29] L. V. Besteiro, X.-T. Kong, Z. Wang, G. Hartland, and A. O. Govorov, "Understanding hot-electron generation and plasmon relaxation in metal nanocrystals: Quantum and classical mechanisms," *Acs Photonics*, vol. 4, no. 11, pp. 2759–2781, 2017.

[30] G. Baffou, P. Berto, E. Bermúdez Ureña, R. Quidant, S. Monneret, J. Polleux, and H. Rigneault, "Photoinduced heating of nanoparticle arrays," *Acs Nano*, vol. 7, no. 8, pp. 6478–6488, 2013.

[31] G. Baffou and R. Quidant, "Thermo-plasmonics: using metallic nanostructures as nano-sources of heat," *Laser & Photonics Reviews*, vol. 7, no. 2, pp. 171–187, 2013.

[32] S. Link and M. A. El-Sayed, "Shape and size dependence of radiative, non-radiative and photothermal properties of gold nanocrystals," *International reviews in physical chemistry*, vol. 19, no. 3, pp. 409–453, 2000.

[33] E. Dulkeith, T. Niedereichholz, T. Klar, J. Feldmann, G. Von Plessen, D. Gittins, K. Mayya, and F. Caruso, "Plasmon emission in photoexcited gold nanoparticles," *Physical Review B*, vol. 70, no. 20, p. 205424, 2004.

[34] Y.-Y. Cai, J. G. Liu, L. J. Tauzin, D. Huang, E. Sung, H. Zhang, A. Joplin, W.-S. Chang, P. Nordlander, and S. Link, "Photoluminescence of gold nanorods: Purcell effect enhanced emission from hot carriers," *Acs Nano*, vol. 12, no. 2, pp. 976–985, 2018.

[35] M. Barella, I. L. Violi, J. Gargiulo, L. P. Martinez, F. Goschin, V. Guglielmotti, D. Pallarola, S. Schlücker, M. Pilo-Pais, G. P. Acuna, S. A. Maier, E. Cortés, and F. D. Stefani, "In situ photothermal response of single gold nanoparticles through hyperspectral imaging anti-stokes thermometry," *ACS Nano*, vol. 15, no. 2, pp. 2458–2467, 2021.

[36] A. Tcherniak, S. Dominguez-Medina, W.-S. Chang, P. Swanglap, L. S. Slaughter, C. F. Landes, and S. Link, "One-photon plasmon luminescence and its application to correlation spectroscopy as a probe for rotational and translational dynamics of gold nanorods," *The Journal of Physical Chemistry C*, vol. 115, no. 32, pp. 15938–15949, 2011.

[37] G. V. Hartland, L. V. Besteiro, P. Johns, and A. O. Govorov, "What's so hot about electrons in metal nanoparticles?," *ACS Energy Letters*, vol. 2, no. 7, pp. 1641–1653, 2017.

[38] B. Wang, P. Yu, W. Wang, X. Zhang, H.-C. Kuo, H. Xu, and Z. M. Wang, "High-q plasmonic resonances: Fundamentals and applications," *Advanced Optical Materials*, vol. 9, no. 7, p. 2001520, 2021.

[39] W. Rechberger, A. Hohenau, A. Leitner, J. Krenn, B. Lamprecht, and F. Aussenegg, "Optical properties of two interacting gold nanoparticles," *Optics communications*, vol. 220, no. 1-3, pp. 137–141, 2003.

[40] N. J. Halas, S. Lal, W.-S. Chang, S. Link, and P. Nordlander, "Plasmons in strongly coupled metallic nanostructures," *Chemical reviews*, vol. 111, no. 6, pp. 3913–3961, 2011.

[41] J. H. Yoon, F. Selbach, L. Langolf, and S. Schlücker, "Ideal dimers of gold nanospheres for precision plasmonics: Synthesis and characterization at the single-particle level for identification of higher order modes," *Small*, vol. 14, no. 4, p. 1702754, 2018.

[42] H. Cha, J. H. Yoon, and S. Yoon, "Probing quantum plasmon coupling using gold nanoparticle dimers with tunable interparticle distances down to the subnanometer range," *ACS nano*, vol. 8, no. 8, pp. 8554–8563, 2014.

[43] E. Cortés, F. J. Wendisch, L. Sortino, A. Mancini, S. Ezendam, S. Saris, L. de S. Menezes, A. Tittl, H. Ren, and S. A. Maier, "Optical metasurfaces for energy conversion," *Chemical Reviews*, vol. 0, no. 0, p. null, 0. PMID: 35728004.

[44] C. Zhan, X.-J. Chen, J. Yi, J.-F. Li, D.-Y. Wu, and Z.-Q. Tian, "From plasmon-enhanced molecular spectroscopy to plasmon-mediated chemical reactions," *Nature Reviews Chemistry*, vol. 2, no. 9, pp. 216–230, 2018.

[45] Y. Wy, H. Jung, J. W. Hong, and S. W. Han, "Exploiting plasmonic hot spots in au-based nanostructures for sensing and photocatalysis," *Accounts of Chemical Research*, vol. 55, no. 6, pp. 831–843, 2022.

[46] J. Gargiulo, R. Berté, Y. Li, S. A. Maier, and E. Cortés, "From optical to chemical hot spots in plasmonics," *Accounts of chemical research*, vol. 52, no. 9, pp. 2525–2535, 2019.

[47] E. Cortés, W. Xie, J. Cambiasso, A. S. Jermyn, R. Sundararaman, P. Narang, S. Schlücker, and S. A. Maier, "Plasmonic hot electron transport drives nano-localized chemistry," *Nature communications*, vol. 8, p. 14880, 2017.

[48] S. Lee, H. Hwang, W. Lee, D. Schebarchov, Y. Wy, J. Grand, B. Auguié, D. H. Wi, E. Cortés, and S. W. Han, "Core–shell bimetallic nanoparticle trimers for efficient light-to-chemical energy conversion," *ACS Energy Letters*, vol. 5, no. 12, pp. 3881–3890, 2020.

[49] V. Mkhitaryan, K. March, E. N. Tseng, X. Li, L. Scarabelli, L. M. Liz-Marzán, S.-Y. Chen, L. H. Tizei, O. Stéphan, J.-M. Song, *et al.*, "Can copper nanostructures sustain high-quality plasmons?," *Nano Letters*, vol. 21, no. 6, pp. 2444–2452, 2021.

[50] Y. Negrín-Montecelo, M. Comesana-Hermo, L. K. Khorashad, A. Sousa-Castillo, Z. Wang, M. Perez-Lorenzo, T. Liedl, A. O. Govorov, and M. A. Correa-Duarte, "Photophysical effects behind the efficiency of hot electron injection in plasmon-assisted catalysis: the joint role of morphology and composition," *ACS Energy Letters*, vol. 5, no. 2, pp. 395–402, 2019.

[51] J. Pérez-Juste, I. Pastoriza-Santos, L. M. Liz-Marzán, and P. Mulvaney, "Gold nanorods: synthesis, characterization and applications," *Coordination chemistry reviews*, vol. 249, no. 17-18, pp. 1870–1901, 2005.

[52] L. Scarabelli and L. M. Liz-Marzan, "An extended protocol for the synthesis of monodisperse gold nanotriangles," 2021.

[53] S. Mukherjee, L. Zhou, A. M. Goodman, N. Large, C. Ayala-Orozco, Y. Zhang, P. Nordlander, and N. J. Halas, "Hot-electron-induced dissociation of h2 on gold nanoparticles supported on sio2," *Journal of the American Chemical Society*, vol. 136, no. 1, pp. 64–67, 2014.

[54] A. Manjavacas, J. G. Liu, V. Kulkarni, and P. Nordlander, "Plasmon-induced hot carriers in metallic nanoparticles," *ACS nano*, vol. 8, no. 8, pp. 7630–7638, 2014.

[55] C. Boerigter, R. Campana, M. Morabito, and S. Linic, "Evidence and implications of direct charge excitation as the dominant mechanism in plasmon-mediated photocatalysis," *Nature communications*, vol. 7, no. 1, p. 10545, 2016.

[56] W. Ho, "Reactions at metal surfaces induced by femtosecond lasers, tunneling electrons, and heating," *The Journal of Physical Chemistry*, vol. 100, no. 31, pp. 13050–13060, 1996.

[57] P. Avouris and R. E. Walkup, "Fundamental mechanisms of desorption and fragmentation induced by electronic transitions at surfaces," *Annual Review of Physical Chemistry*, vol. 40, no. 1, pp. 173–206, 1989.

[58] M. Bonn, S. Funk, C. Hess, D. N. Denzler, C. Stampfl, M. Scheffler, M. Wolf, and G. Ertl, "Phonon-versus electron-mediated desorption and oxidation of co on ru (0001)," *Science*, vol. 285, no. 5430, pp. 1042–1045, 1999.

[59] E. Oksenberg, I. Shlesinger, A. Xomalis, A. Baldi, J. J. Baumberg, A. F. Koenderink, and E. C. Garnett, "Energy-resolved plasmonic chemistry in individual nanoreactors," *Nature Nanotechnology*, pp. 1–8, 2021.

[60] S. A. Lee and S. Link, "Chemical interface damping of surface plasmon resonances," *Accounts of Chemical Research*, vol. 54, no. 8, pp. 1950–1960, 2021.

[61] G. Baffou, R. Quidant, and C. Girard, "Heat generation in plasmonic nanostructures: Influence of morphology," *Applied Physics Letters*, vol. 94, no. 15, p. 153109, 2009.

[62] E. Cortés, L. V. Besteiro, A. Alabastri, A. Baldi, G. Tagliabue, A. Demetriadou, and P. Narang, "Challenges in plasmonic catalysis," *ACS nano*, vol. 14, no. 12, pp. 16202–16219, 2020.

[63] L. Zhou, D. F. Swearer, C. Zhang, H. Robatjazi, H. Zhao, L. Henderson, L. Dong, P. Christopher, E. A. Carter, P. Nordlander, *et al.*, "Quantifying hot carrier and thermal contributions in plasmonic photocatalysis," *Science*, vol. 362, no. 6410, pp. 69–72, 2018.

[64] Y. Sivan, J. Baraban, I. W. Un, and Y. Dubi, "Comment on "quantifying hot carrier and thermal contributions in plasmonic photocatalysis"," *Science*, vol. 364, no. 6439, p. eaaw9367, 2019.

[65] Y. Sivan, J. Baraban, and Y. Dubi, "Further comments on" quantifying hot carrier and thermal contributions in plasmonic photocatalysis"," 2020.

[66] Y. Dubi, I. W. Un, and Y. Sivan, "Thermal effects–an alternative mechanism for plasmon-assisted photocatalysis," *Chemical Science*, vol. 11, no. 19, pp. 5017–5027, 2020.

[67] K. Wu, J. Chen, J. R. McBride, and T. Lian, "Efficient hot-electron transfer by a plasmon-induced interfacial charge-transfer transition," *Science*, vol. 349, no. 6248, pp. 632–635, 2015.

[68] C. Zhan, Q.-X. Wang, J. Yi, L. Chen, D.-Y. Wu, Y. Wang, Z.-X. Xie, M. Moskovits, and Z.-Q. Tian, "Plasmonic nanoreactors regulating selective oxidation by energetic electrons and nanoconfined thermal fields," *Science advances*, vol. 7, no. 10, p. eabf0962, 2021.

[69] S. Ezendam, M. Herran, L. Nan, C. Gruber, Y. Kang, F. Gröbmeyer, R. Lin, J. Gargiulo, A. Sousa-Castillo, and E. Cortés, "Hybrid plasmonic nanomaterials for hydrogen generation and carbon dioxide reduction," *ACS Energy Letters*, vol. 7, no. 2, pp. 778–815, 2022.

[70] J. K. Nørskov, F. Abild-Pedersen, F. Studt, and T. Bligaard, "Density functional theory in surface chemistry and catalysis," *Proceedings of the National Academy of Sciences*, vol. 108, no. 3, pp. 937–943, 2011.

[71] B. Hammer and J. K. Norskov, "Why gold is the noblest of all the metals," *Nature*, vol. 376, no. 6537, pp. 238–240, 1995.

[72] J. K. Nørskov, F. Studt, F. Abild-Pedersen, and T. Bligaard, *Fundamental concepts in heterogeneous catalysis*. John Wiley & Sons, 2014.

[73] Z. Zheng, T. Tachikawa, and T. Majima, "Plasmon-enhanced formic acid dehydrogenation using anisotropic pd–au nanorods studied at the single-particle level," *Journal of the American Chemical Society*, vol. 137, no. 2, pp. 948–957, 2015.

[74] P. Xu, W. Lu, J. Zhang, and L. Zhang, "Efficient hydrolysis of ammonia borane for hydrogen evolution catalyzed by plasmonic ag@ pd core–shell nanocubes," *ACS Sustainable Chemistry & Engineering*, vol. 8, no. 33, pp. 12366–12377, 2020.

[75] J.-L. Yang, Y.-L. He, H. Ren, H.-L. Zhong, J.-S. Lin, W.-M. Yang, M.-D. Li, Z.-L. Yang, H. Zhang, Z.-Q. Tian, *et al.*, "Boosting photocatalytic hydrogen evolution reaction using dual plasmonic antennas," *ACS Catalysis*, vol. 11, no. 9, pp. 5047–5053, 2021.

[76] L. Qin, G. Wang, and Y. Tan, "Plasmonic pt nanoparticles—tio2 hierarchical nanoarchitecture as a visible light photocatalyst for water splitting," *Scientific reports*, vol. 8, no. 1, p. 16198, 2018.

[77] K. Sytwu, M. Vadai, and J. A. Dionne, "Bimetallic nanostructures: combining plasmonic and catalytic metals for photocatalysis," *Advances in Physics: X*, vol. 4, no. 1, p. 1619480, 2019.

[78] G. T. Forcherio, B. Ostovar, J. Boltersdorf, Y.-Y. Cai, A. C. Leff, K. N. Grew, C. A. Lundgren, S. Link, and D. R. Baker, "Single-particle insights into plasmonic hot carrier separation augmenting photoelectrochemical ethanol oxidation with photocatalytically synthesized pd–au bimetallic nanorods," *ACS nano*, vol. 16, no. 8, pp. 12377–12389, 2022.

[79] C. Engelbrekt, K. T. Crampton, D. A. Fishman, M. Law, and V. A. Apkarian, "Efficient plasmon-mediated energy funneling to the surface of au@ pt core–shell nanocrystals," *ACS nano*, vol. 14, no. 4, pp. 5061–5074, 2020.

[80] U. Aslam, S. Chavez, and S. Linic, "Controlling energy flow in multimetallic nanostructures for plasmonic catalysis," *Nature nanotechnology*, vol. 12, no. 10, pp. 1000–1005, 2017.

[81] K. Tedsree, T. Li, S. Jones, C. W. A. Chan, K. M. K. Yu, P. A. Bagot, E. A. Marquis, G. D. Smith, and S. C. E. Tsang, "Hydrogen production from formic acid decomposition at room temperature using a ag–pd core–shell nanocatalyst," *Nature nanotechnology*, vol. 6, no. 5, pp. 302–307, 2011.

[82] C. Zhang, H. Zhao, L. Zhou, A. E. Schlather, L. Dong, M. J. McClain, D. F. Swearer, P. Nordlander, and N. J. Halas, "Al–pd nanodisk heterodimers as antenna–reactor photocatalysts," *Nano letters*, vol. 16, no. 10, pp. 6677–6682, 2016.

[83] K. Li, N. J. Hogan, M. J. Kale, N. J. Halas, P. Nordlander, and P. Christopher, "Balancing near-field enhancement, absorption, and scattering for effective antenna–reactor plasmonic photocatalysis," *Nano letters*, vol. 17, no. 6, pp. 3710–3717, 2017.

[84] J. He, N. J. Johnson, A. Huang, and C. P. Berlinguette, "Electrocatalytic alloys for co2 reduction," *ChemSusChem*, vol. 11, no. 1, pp. 48–57, 2018.

[85] J. M. Rahm, C. Tiburski, T. P. Rossi, F. A. A. Nugroho, S. Nilsson, C. Langhammer, and P. Erhart, "A library of late transition metal alloy dielectric functions for nanophotonic applications," *Advanced Functional Materials*, vol. 30, no. 35, p. 2002122, 2020.

[86] J. A. Esterhuizen, B. R. Goldsmith, and S. Linic, "Theory-guided machine learning finds geometric structure-property relationships for chemisorption on subsurface alloys," *Chem*, vol. 6, no. 11, pp. 3100–3117, 2020.

[87] L. Zhou, J. M. P. Martirez, J. Finzel, C. Zhang, D. F. Swearer, S. Tian, H. Robatjazi, M. Lou, L. Dong, L. Henderson, *et al.*, "Light-driven methane dry reforming with single atomic site antenna-reactor plasmonic photocatalysts," *Nature Energy*, vol. 5, no. 1, pp. 61–70, 2020.

[88] H. Zhang, G. Liu, L. Shi, and J. Ye, "Single-atom catalysts: emerging multifunctional materials in heterogeneous catalysis," *Advanced Energy Materials*, vol. 8, no. 1, p. 1701343, 2018.

[89] S. Zafeiratos, S. Piccinin, and D. Teschner, "Alloys in catalysis: phase separation and surface segregation phenomena in response to the reactive environment," *Catalysis Science & Technology*, vol. 2, no. 9, pp. 1787–1801, 2012.

[90] J. Polte, "Fundamental growth principles of colloidal metal nanoparticles–a new perspective," *CrystEngComm*, vol. 17, no. 36, pp. 6809–6830, 2015.

[91] N. T. Thanh, N. Maclean, and S. Mahiddine, "Mechanisms of nucleation and growth of nanoparticles in solution," *Chemical reviews*, vol. 114, no. 15, pp. 7610–7630, 2014.

[92] Y. Li, W. Zhou, I. Tanriover, W. Hadibrata, B. E. Partridge, H. Lin, X. Hu, B. Lee, J. Liu, V. P. Dravid, *et al.*, "Open-channel metal particle superlattices," *Nature*, vol. 611, no. 7937, pp. 695–701, 2022.

[93] F. Schulz, O. Pavelka, F. Lehmkühler, F. Westermeier, Y. Okamura, N. S. Mueller, S. Reich, and H. Lange, "Structural order in plasmonic superlattices," *Nature communications*, vol. 11, no. 1, pp. 1–9, 2020.

[94] M. S. Lee, D. W. Yee, M. Ye, and R. J. Macfarlane, "Nanoparticle assembly as a materials development tool," *Journal of the American Chemical Society*, vol. 144, no. 8, pp. 3330–3346, 2022.

[95] M. Grzelczak, L. M. Liz-Marzán, and R. Klajn, "Stimuli-responsive self-assembly of nanoparticles," *Chemical Society Reviews*, vol. 48, no. 5, pp. 1342–1361, 2019.

[96] Z. Cheng and M. R. Jones, "Assembly of planar chiral superlattices from achiral building blocks," *Nature Communications*, vol. 13, no. 1, pp. 1–11, 2022.

[97] *https://www.schaefer-tec.it/en/cat-prodotti/zeta-potential-measurement*.

[98] M. Faraday, "X. the bakerian lecture.—experimental relations of gold (and other metals) to light," *Philosophical transactions of the Royal Society of London*, no. 147, pp. 145–181, 1857.

[99] Y. Zheng, X. Zhong, Z. Li, and Y. Xia, "Successive, seed-mediated growth for the synthesis of single-crystal gold nanospheres with uniform diameters controlled in the range of 5–150 nm," *Particle & Particle Systems Characterization*, vol. 31, no. 2, pp. 266–273, 2014.

[100] X. Xia, S. Xie, M. Liu, H.-C. Peng, N. Lu, J. Wang, M. J. Kim, and Y. Xia, "On the role of surface diffusion in determining the shape or morphology of noble-metal nanocrystals," *Proceedings of the National Academy of Sciences*, vol. 110, no. 17, pp. 6669–6673, 2013.

[101] L. Qiao, N. Pollard, R. Senanayake, Z. Yang, M. Kim, A. Ali, M. T. Hoang, N. Yao, Y. Han, R. Hernandez, *et al.*, "Particle or cluster: On the atomic structure of the seeds used in gold nanoparticle synthesis," 2022.

[102] S.-C. Hsu, Y.-C. Chuang, B. T. Sneed, D. A. Cullen, T.-W. Chiu, and C.-H. Kuo, "Turning the halide switch in the synthesis of au–pd alloy and core–shell nanoicosahedra with terraced shells: performance in electrochemical and plasmon-enhanced catalysis," *Nano letters*, vol. 16, no. 9, pp. 5514–5520, 2016.

[103] J. A. d. Silva, R. P. Dias, G. C. da Hora, T. A. Soares, and M. R. Meneghetti, "Molecular dynamics simulations of cetyltrimethylammonium bromide (ctab) micelles and their interactions with a gold surface in aqueous solution," *Journal of the Brazilian Chemical Society*, vol. 29, pp. 191–199, 2018.

[104] W. Xie, B. Walkenfort, and S. Schlücker, "Label-free sers monitoring of chemical reactions catalyzed by small gold nanoparticles using 3d plasmonic superstructures," *Journal of the American Chemical Society*, vol. 135, no. 5, pp. 1657–1660, 2013.

[105] C. Hu, Y. Hu, C. Fan, L. Yang, Y. Zhang, H. Li, and W. Xie, "Surface-enhanced raman spectroscopic evidence of key intermediate species and role of nife dual-catalytic

center in water oxidation," *Angewandte Chemie*, vol. 133, no. 36, pp. 19927–19931, 2021.

[106] K. Zhang, L. Yang, Y. Hu, C. Fan, Y. Zhao, L. Bai, Y. Li, F. Shi, J. Liu, and W. Xie, "Synthesis of a gold–metal oxide core–satellite nanostructure for in situ sers study of cuo-catalyzed photooxidation," *Angewandte Chemie*, vol. 132, no. 41, pp. 18159–18165, 2020.

[107] D. Wang, F. Shi, J. Jose, Y. Hu, C. Zhang, A. Zhu, R. Grzeschik, S. Schlücker, and W. Xie, "In situ monitoring of palladium-catalyzed chemical reactions by nanogap-enhanced raman scattering using single pd cube dimers," *Journal of the American Chemical Society*, vol. 144, no. 11, pp. 5003–5009, 2022.

[108] H. Hu, F. Ji, Y. Xu, J. Yu, Q. Liu, L. Chen, Q. Chen, P. Wen, Y. Lifshitz, Y. Wang, *et al.*, "Reversible and precise self-assembly of janus metal-organosilica nanoparticles through a linker-free approach," *ACS nano*, vol. 10, no. 8, pp. 7323–7330, 2016.

[109] F. Schulz and H. Lange, "Optimizing interparticle gaps in large-scale gold nanoparticle supercrystals for flexible light-matter coupling," *Advanced Optical Materials*, vol. 10, no. 24, p. 2202064, 2022.

[110] G. V. Hartland, "Measurements of the material properties of metal nanoparticles by time-resolved spectroscopy," *Physical Chemistry Chemical Physics*, vol. 6, no. 23, pp. 5263–5274, 2004.

[111] A. Schirato, M. Maiuri, G. Cerullo, and G. Della Valle, "Ultrafast hot electron dynamics in plasmonic nanostructures: experiments, modelling, design," *Nanophotonics*, 2023.

[112] E. Tan, "Fundamental implicit fdtd schemes for computational electromagnetics and educational mobile apps (invited review)," *Progress In Electromagnetics Research*, vol. 168, pp. 39–59, 2020.

[113] D. E. McCoy, A. V. Shneidman, A. L. Davis, and J. Aizenberg, "Finite-difference time-domain (fdtd) optical simulations: A primer for the life sciences and bio-inspired engineering," *Micron*, vol. 151, p. 103160, 2021.

[114] K. Sytwu, M. Vadai, F. Hayee, D. K. Angell, A. Dai, J. Dixon, and J. A. Dionne, "Driving energetically unfavorable dehydrogenation dynamics with plasmonics," *Science*, vol. 371, no. 6526, pp. 280–283, 2021.

[115] J. U. Salmón-Gamboa, M. Romero-Gómez, D. J. Roth, A. V. Krasavin, P. Wang, W. Dickson, and A. V. Zayats, "Rational design of bimetallic photocatalysts based on plasmonically-derived hot carriers," *Nanoscale Adv.*, vol. 3, pp. 767–780, 2021.

[116] L. Scarabelli, A. Sánchez-Iglesias, J. Pérez-Juste, and L. M. Liz-Marzán, "A "tips and tricks" practical guide to the synthesis of gold nanorods," *The Journal of Physical Chemistry Letters*, vol. 6, no. 21, pp. 4270–4279, 2015.

[117] S. Sarina, H. Zhu, E. Jaatinen, Q. Xiao, H. Liu, J. Jia, C. Chen, and J. Zhao, "Enhancing catalytic performance of palladium in gold and palladium alloy nanoparticles for organic synthesis reactions through visible light irradiation at ambient temperatures," *Journal of the American Chemical Society*, vol. 135, no. 15, pp. 5793–5801, 2013.

[118] V. Pifferi, C. E. Chan-Thaw, S. Campisi, A. Testolin, A. Villa, L. Falciola, and L. Prati, "Au-based catalysts: electrochemical characterization for structural insights," *Molecules*, vol. 21, no. 3, p. 261, 2016.

[119] M. Valenti, N. P. Prasad, R. Kas, D. Bohra, M. Ma, V. Balasubramanian, L. Chu, S. Gimenez, J. Bisquert, B. Dam, *et al.*, "Suppressing h2 evolution and promoting selective co2 electroreduction to co at low overpotentials by alloying au with pd," *ACS Catalysis*, vol. 9, no. 4, pp. 3527–3536, 2019.

[120] J. S. Jirkovsky, I. Panas, E. Ahlberg, M. Halasa, S. Romani, and D. J. Schiffrin, "Single atom hot-spots at au–pd nanoalloys for electrocatalytic h2o2 production," *Journal of the American Chemical Society*, vol. 133, no. 48, pp. 19432–19441, 2011.

[121] S.-J. Li, Y.-T. Zhou, X. Kang, D.-X. Liu, L. Gu, Q.-H. Zhang, J.-M. Yan, and Q. Jiang, "A simple and effective principle for a rational design of heterogeneous catalysts for dehydrogenation of formic acid," *Advanced Materials*, vol. 31, no. 15, p. 1806781, 2019.

[122] C.-R. Kao, Y.-C. Huang, B. Talukdar, Y.-C. Chuang, Y.-R. Lu, H.-M. Lin, W.-C. Chou, D. A. Cullen, C.-L. Dong, and C.-H. Kuo, "Aupd nanoicosahedra: Atomic-level surface modulation for optimization of electrocatalytic and photocatalytic energy conversion," *ACS Applied Energy Materials*, 2021.

[123] C. H. Kelly, T. M. Benedetti, A. Alinezhad, J. J. Gooding, and R. D. Tilley, "Controlling metallic nanoparticle redox properties for improved methanol oxidation reaction electrocatalysis," *ChemCatChem*, vol. 11, no. 24, pp. 5989–5993, 2019.

[124] Z.-Q. Tian, B. Ren, J.-F. Li, and Z.-L. Yang, "Expanding generality of surface-enhanced raman spectroscopy with borrowing sers activity strategy," *Chemical Communications*, no. 34, pp. 3514–3534, 2007.

[125] Y. Li, Y. Hu, F. Shi, H. Li, W. Xie, and J. Chen, "C- h arylation on nickel nanoparticles monitored by in situ surface-enhanced raman spectroscopy," *Angewandte Chemie International Edition*, vol. 58, no. 27, pp. 9049–9053, 2019.

[126] M. Mao, B. Zhou, X. Tang, C. Chen, M. Ge, P. Li, X. Huang, L. Yang, and J. Liu, "Natural deposition strategy for interfacial, self-assembled, large-scale, densely packed, monolayer film with ligand-exchanged gold nanorods for in situ surface-enhanced raman scattering drug detection," *Chemistry–A European Journal*, vol. 24, no. 16, pp. 4094–4102, 2018.

[127] W.-Y. Yu, G. M. Mullen, D. W. Flaherty, and C. B. Mullins, "Selective hydrogen production from formic acid decomposition on pd–au bimetallic surfaces," *Journal of the American Chemical Society*, vol. 136, no. 31, pp. 11070–11078, 2014.

[128] H.-X. Zhang, S.-H. Wang, K. Jiang, T. André, and W.-B. Cai, "In situ spectroscopic investigation of co accumulation and poisoning on pd black surfaces in concentrated hcooh," *Journal of Power Sources*, vol. 199, pp. 165–169, 2012.

[129] B. Wu, J. Lee, S. Mubeen, Y.-S. Jun, G. D. Stucky, and M. Moskovits, "Plasmon-mediated photocatalytic decomposition of formic acid on palladium nanostructures," *Advanced Optical Materials*, vol. 4, no. 7, pp. 1041–1046, 2016.

[130] P. K. Jain, "Taking the heat off of plasmonic chemistry," *The Journal of Physical Chemistry C*, vol. 123, no. 40, pp. 24347–24351, 2019.

[131] I.-W. Un and Y. Sivan, "The role of heat generation and fluid flow in plasmon-enhanced reduction–oxidation reactions," *ACS Photonics*, vol. 8, no. 4, pp. 1183–1190, 2021.

[132] Ö. Metin, X. Sun, and S. Sun, "Monodisperse gold–palladium alloy nanoparticles and their composition-controlled catalysis in formic acid dehydrogenation under mild conditions," *Nanoscale*, vol. 5, no. 3, pp. 910–912, 2013.

[133] S. Chavez, U. Aslam, and S. Linic, "Design principles for directing energy and energetic charge flow in multicomponent plasmonic nanostructures," *ACS Energy Letters*, vol. 3, no. 7, pp. 1590–1596, 2018.

[134] D. F. Swearer, H. Zhao, L. Zhou, C. Zhang, H. Robatjazi, J. M. P. Martirez, C. M. Krauter, S. Yazdi, M. J. McClain, E. Ringe, *et al.*, "Heterometallic antenna- reactor complexes for photocatalysis," *Proceedings of the National Academy of Sciences*, vol. 113, no. 32, pp. 8916–8920, 2016.

[135] M. Herran, A. Sousa-Castillo, C. Fan, S. Lee, W. Xie, M. Döblinger, B. Auguié, and E. Cortés, "Tailoring plasmonic bimetallic nanocatalysts toward sunlight-driven h2 production," *Advanced Functional Materials*, vol. 32, no. 38, p. 2203418, 2022.

[136] E. Pensa, J. Gargiulo, A. Lauri, S. Schlücker, E. Cortés, and S. A. Maier, "Spectral screening of the energy of hot holes over a particle plasmon resonance," *Nano letters*, vol. 19, no. 3, pp. 1867–1874, 2019.

[137] E. Y. Santiago, L. V. Besteiro, X.-T. Kong, M. A. Correa-Duarte, Z. Wang, and A. O. Govorov, "Efficiency of hot-electron generation in plasmonic nanocrystals with complex shapes: surface-induced scattering, hot spots, and interband transitions," *ACS Photonics*, vol. 7, no. 10, pp. 2807–2824, 2020.

[138] P. Rodenas, T. Song, P. Sudhagar, G. Marzari, H. Han, L. Badia-Bou, S. Gimenez, F. Fabregat-Santiago, I. Mora-Sero, J. Bisquert, *et al.*, "Quantum dot based heterostructures for unassisted photoelectrochemical hydrogen generation," *Advanced Energy Materials*, vol. 3, no. 2, pp. 176–182, 2013.

[139] Y. Kim, S.-h. Kim, H. C. Ham, and D. H. Kim, "Mechanistic insights on aqueous formic acid dehydrogenation over pd/c catalyst for efficient hydrogen production," *Journal of Catalysis*, vol. 389, pp. 506–516, 2020.

[140] M. Navlani-García, K. Mori, D. Salinas-Torres, Y. Kuwahara, and H. Yamashita, "New approaches toward the hydrogen production from formic acid dehydrogenation over pd-based heterogeneous catalysts," *Frontiers in Materials*, p. 44, 2019.

[141] Z. Lou, M. Fujitsuka, and T. Majima, "Pt–au triangular nanoprisms with strong dipole plasmon resonance for hydrogen generation studied by single-particle spectroscopy," *ACS nano*, vol. 10, no. 6, pp. 6299–6305, 2016.

[142] B. Seemala, A. J. Therrien, M. Lou, K. Li, J. P. Finzel, J. Qi, P. Nordlander, and P. Christopher, "Plasmon-mediated catalytic o2 dissociation on ag nanostructures: Hot electrons or near fields?," *ACS Energy Letters*, vol. 4, no. 8, pp. 1803–1809, 2019.

[143] Z. Zheng, T. Tachikawa, and T. Majima, "Single-particle study of pt-modified au nanorods for plasmon-enhanced hydrogen generation in visible to near-infrared region," *Journal of the American Chemical Society*, vol. 136, no. 19, pp. 6870–6873, 2014.

[144] P. R. West, S. Ishii, G. V. Naik, N. K. Emani, V. M. Shalaev, and A. Boltasseva, "Searching for better plasmonic materials," *Laser & photonics reviews*, vol. 4, no. 6, pp. 795–808, 2010.

[145] G. V. Naik, J. L. Schroeder, X. Ni, A. V. Kildishev, T. D. Sands, and A. Boltasseva, "Titanium nitride as a plasmonic material for visible and near-infrared wavelengths," *Optical Materials Express*, vol. 2, no. 4, pp. 478–489, 2012.

[146] P. Zolotavin, A. Alabastri, P. Nordlander, and D. Natelson, "Plasmonic heating in au nanowires at low temperatures: the role of thermal boundary resistance," *ACS nano*, vol. 10, no. 7, pp. 6972–6979, 2016.

[147] D.-K. Lim, A. Barhoumi, R. G. Wylie, G. Reznor, R. S. Langer, and D. S. Kohane, "Enhanced photothermal effect of plasmonic nanoparticles coated with reduced graphene oxide," *Nano letters*, vol. 13, no. 9, pp. 4075–4079, 2013.

[148] M. J. Penelas, G. F. Arenas, F. Trabadelo, G. J. Soler-Illia, S. E. Moya, P. C. Angelomé, and C. E. Hoppe, "Importance of the structural and physicochemical properties of silica nanoshells in the photothermal effect of silica-coated au nanoparticles suspensions," *Langmuir*, vol. 38, no. 12, pp. 3876–3886, 2022.

[149] H. Robatjazi, J. L. Bao, M. Zhang, L. Zhou, P. Christopher, E. A. Carter, P. Nordlander, and N. J. Halas, "Plasmon-driven carbon–fluorine (c (sp 3)–f) bond activation with mechanistic insights into hot-carrier-mediated pathways," *Nature Catalysis*, vol. 3, no. 7, pp. 564–573, 2020.

[150] Y. Dubi, I. W. Un, J. H. Baraban, and Y. Sivan, "Distinguishing thermal from nonthermal contributions to plasmonic hydrodefluorination," *Nature Catalysis*, vol. 5, no. 4, pp. 244–246, 2022.

[151] G. Baffou, "Anti-stokes thermometry in nanoplasmonics," *ACS nano*, vol. 15, no. 4, pp. 5785–5792, 2021.

[152] A. Movsesyan, S. Marguet, A. Muravitskaya, J. Béal, P.-M. Adam, and A.-L. Baudrion, "Influence of the ctab surfactant layer on optical properties of single metallic nanospheres," *JOSA A*, vol. 36, no. 11, pp. C78–C84, 2019.

[153] J. Gargiulo, I. L. Violi, S. Cerrota, L. Chvatal, E. Cortés, E. M. Perassi, F. Diaz, P. Zemánek, and F. D. Stefani, "Accuracy and mechanistic details of optical printing of single au and ag nanoparticles," *ACS nano*, vol. 11, no. 10, pp. 9678–9688, 2017.

[154] A. S. Urban, A. A. Lutich, F. D. Stefani, and J. Feldmann, "Laser printing single gold nanoparticles," *Nano letters*, vol. 10, no. 12, pp. 4794–4798, 2010.

[155] Z. Ge, D. G. Cahill, and P. V. Braun, "Thermal conductance of hydrophilic and hydrophobic interfaces," *Physical review letters*, vol. 96, no. 18, p. 186101, 2006.

[156] J. Gargiulo, M. Herran, I. Violi, A. Sousa-Castillo, L. Martinez, S. Ezendam, M. Barella, H. Giesler, R. Grzeschik, S. Schluecker, *et al.*, "Single particle thermometry in bimetallic plasmonic nanostuctures," 2022.

[157] J. Park and D. G. Cahill, "Plasmonic sensing of heat transport at solid–liquid interfaces," *The Journal of Physical Chemistry C*, vol. 120, no. 5, pp. 2814–2821, 2016.

[158] H. Hu and Y. Sun, "Effect of nanopatterns on kapitza resistance at a water-gold interface during boiling: A molecular dynamics study," *Journal of Applied Physics*, vol. 112, no. 5, p. 053508, 2012.

[159] H. Harikrishna, W. A. Ducker, and S. T. Huxtable, "The influence of interface bonding on thermal transport through solid–liquid interfaces," *Applied Physics Letters*, vol. 102, no. 25, p. 251606, 2013.

[160] J. Vera and Y. Bayazitoglu, "Temperature and heat flux dependence of thermal resistance of water/metal nanoparticle interfaces at sub-boiling temperatures," *International Journal of Heat and Mass Transfer*, vol. 86, pp. 433–442, 2015.

[161] S. Li, Y. Chen, J. Zhao, C. Wang, and N. Wei, "Atomic structure causing an obvious difference in thermal conductance at the pd–h 2 o interface: a molecular dynamics simulation," *Nanoscale*, vol. 12, no. 34, pp. 17870–17879, 2020.

[162] G. Baffou and R. Quidant, "Nanoplasmonics for chemistry," *Chemical Society Reviews*, vol. 43, no. 11, pp. 3898–3907, 2014.

[163] N. J. Hogan, A. S. Urban, C. Ayala-Orozco, A. Pimpinelli, P. Nordlander, and N. J. Halas, "Nanoparticles heat through light localization," *Nano letters*, vol. 14, no. 8, pp. 4640–4645, 2014.

[164] Y. Kim, J. G. Smith, and P. K. Jain, "Harvesting multiple electron–hole pairs generated through plasmonic excitation of au nanoparticles," *Nature chemistry*, vol. 10, no. 7, pp. 763–769, 2018.

[165] P. K. Jain, W. Qian, and M. A. El-Sayed, "Ultrafast cooling of photoexcited electrons in gold nanoparticle- thiolated dna conjugates involves the dissociation of the gold-thiol bond," *Journal of the American Chemical Society*, vol. 128, no. 7, pp. 2426–2433, 2006.

[166] S. K. Boong, C. Chong, J.-K. Lee, Z. Z. Ang, H. Li, and H. K. Lee, "Superlattice-based plasmonic catalysis: Concentrating light at the nanoscale to drive efficient nitrogen-to-ammonia fixation at ambient conditions," *Angewandte Chemie International Edition*, 2022.

[167] R. Yalavarthi, O. Henrotte, Š. Kment, and A. Naldoni, "Determining the role of pd catalyst morphology and deposition criteria over large area plasmonic metasurfaces during light-enhanced electrochemical oxidation of formic acid," *The Journal of Chemical Physics*, vol. 157, no. 11, p. 114706, 2022.

[168] R. Yalavarthi, O. Yesilyurt, O. Henrotte, Š. Kment, V. M. Shalaev, A. Boltasseva, and A. Naldoni, "Multimetallic metasurfaces for enhanced electrocatalytic oxidations in direct alcohol fuel cells," *Laser & Photonics Reviews*, p. 2200137, 2022.

[169] V. G. Kravets, A. V. Kabashin, W. L. Barnes, and A. N. Grigorenko, "Plasmonic surface lattice resonances: a review of properties and applications," *Chemical reviews*, vol. 118, no. 12, pp. 5912–5951, 2018.

[170] R. F. Hamans, M. Parente, G. W. Castellanos, M. Ramezani, J. Gómez Rivas, and A. Baldi, "Super-resolution mapping of enhanced emission by collective plasmonic resonances," *ACS nano*, vol. 13, no. 4, pp. 4514–4521, 2019.

[171] N. S. Mueller, Y. Okamura, B. G. M. Vieira, S. Juergensen, H. Lange, E. B. Barros, F. Schulz, and S. Reich, "Deep strong light–matter coupling in plasmonic nanoparticle crystals," *Nature*, vol. 583, pp. 780–784, 2020.

[172] N. S. Mueller, B. G. M. Vieira, F. Schulz, P. Kusch, V. Oddone, E. B. Barros, H. Lange, and S. Reich, "Dark interlayer plasmons in colloidal gold nanoparticle bi- and few-layers," *ACS Photonics*, vol. 5, no. 10, pp. 3962–3969, 2018.

[173] N. S. Mueller, E. Pfitzner, Y. Okamura, G. Gordeev, P. Kusch, H. Lange, J. Heberle, F. Schulz, and S. Reich, "Surface-enhanced raman scattering and surface-enhanced infrared absorption by plasmon polaritons in three-dimensional nanoparticle supercrystals," *ACS nano*, vol. 15, no. 3, pp. 5523–5533, 2021.

[174] B. G. M. Vieira, N. S. Mueller, E. B. Barros, and S. Reich, "Plasmonic properties of close-packed metallic nanoparticle mono- and bilayers," *The Journal of Physical Chemistry C*, vol. 123, no. 29, pp. 17951–17960, 2019.

[175] R. C. Elias and S. Linic, "Elucidating the roles of local and nonlocal rate enhancement mechanisms in plasmonic catalysis," *Journal of the American Chemical Society*, 2022.

[176] P. D. Dongare, Y. Zhao, D. Renard, J. Yang, O. Neumann, J. Metz, L. Yuan, A. Alabastri, P. Nordlander, and N. J. Halas, "A 3d plasmonic antenna-reactor for nanoscale thermal hotspots and gradients," *ACS nano*, vol. 15, no. 5, pp. 8761–8769, 2021.

[177] J. Eppinger and K.-W. Huang, "Formic acid as a hydrogen energy carrier," *ACS Energy Letters*, vol. 2, no. 1, pp. 188–195, 2017.

[178] M. Rodio, M. Graf, F. Schulz, N. S. Mueller, M. Eich, and H. Lange, "Experimental evidence for nonthermal contributions to plasmon-enhanced electrochemical oxidation reactions," *ACS catalysis*, vol. 10, no. 3, pp. 2345–2353, 2020.

[179] G. Baffou, I. Bordacchini, A. Baldi, and R. Quidant, "Simple experimental procedures to distinguish photothermal from hot-carrier processes in plasmonics," *Light: Science & Applications*, vol. 9, no. 1, pp. 1–16, 2020.

[180] D. Hoeing, F. Schulz, N. S. Mueller, S. Reich, and H. Lange, "Dark plasmon modes for efficient hot electron generation in multilayers of gold nanoparticles," *The Journal of chemical physics*, vol. 152, no. 6, p. 064710, 2020.

[181] V. G. Rao, U. Aslam, and S. Linic, "Chemical requirement for extracting energetic charge carriers from plasmonic metal nanoparticles to perform electron-transfer reactions," *Journal of the American Chemical Society*, vol. 141, no. 1, pp. 643–647, 2018.

[182] S. Zhao, M. Riedel, J. Patarroyo, N. G. Bastús, V. Puntes, Z. Yue, F. Lisdat, and W. J. Parak, "Tailoring of the photocatalytic activity of ceo 2 nanoparticles by the presence of plasmonic ag nanoparticles," *Nanoscale*, vol. 14, no. 33, pp. 12048–12059, 2022.

[183] B. Lim, M. Jiang, J. Tao, P. H. Camargo, Y. Zhu, and Y. Xia, "Shape-controlled synthesis of pd nanocrystals in aqueous solutions," *Advanced Functional Materials*, vol. 19, no. 2, pp. 189–200, 2009.

[184] M. Sanles-Sobrido, M. A. Correa-Duarte, S. Carregal-Romero, B. Rodriguez-Gonzalez, R. A. Alvarez-Puebla, P. Hervés, and L. M. Liz-Marzán, "Highly catalytic single-crystal dendritic pt nanostructures supported on carbon nanotubes," *Chemistry of Materials*, vol. 21, no. 8, pp. 1531–1535, 2009.

[185] F. Schulz, S. Tober, and H. Lange, "Size-dependent phase transfer functionalization of gold nanoparticles to promote well-ordered self-assembly," *Langmuir*, vol. 33, no. 50, pp. 14437–14444, 2017.

[186] A. Dong, J. Chen, P. M. Vora, J. M. Kikkawa, and C. B. Murray, "Binary nanocrystal superlattice membranes self-assembled at the liquid–air interface," *Nature*, vol. 466, no. 7305, pp. 474–477, 2010.

Acknowledgements

The acknowledgments were left to the very end on purpose, to motivate myself to finish this summary of the last 4 years. I hope that every person mentioned here can feel how thankful I find myself to them for such a lovely time together.

I would like to start with the person who made all this possible. Emi, there are countless of moments, talks, advises, dinners, beers, and trips that I really appreciated along the way. However, the main thing that I want to thank you, is for changing completely my entire life. By giving me the chance to do a PhD in your team, without realizing, you granted me with the chance to accomplish a life dream. I will always be grateful for all the time you spent ensuring my comfort and helping me to progress in professional and personal aspects. I wish you, Eva and Nina nothing but the best.

To Martina Edenhofer, Namvar Jahanmehr and Reinhold Rath, our very supportive team. I really appreciate the times you helped me through when I found myself in troubles with either procedures or devices. Especially, I want to thank Martina for treating me so lovingly.

To Sebastian Schlücker and his group, who hosted me during my first month in Germany.

To Center of Nanoscience (CeNS) for providing the funds for me to assist to conferences.

To Baptiste Auguié for the scientific discussions and the beers on your visit.

To Florian Schulz and Sabrina Jürgensen for the scientific discussions in our shared project.

Also, to the former and current members of Hybrid Nanosystems Chair. The working atmosphere, the mensa lunches and the beers in the evenings made these days way funnier and entertaining.

To Paula Neumann, for deciding to do an internship with Simone and myself. Thanks for all the funny moments!

To the incredible friends I made along this journey. Simone Ezendam, Christoph Gruber, Andrea Mancini, Lin Nan, Andrei Stefancu, Joong Bum Lee, Fedja Wendisch, Luca Sortino, Seryio Saris, Benni Tillmann. I will really miss you. The betting for football matches, the shared cookies, Lin's funny weirdness, Simone's unprecedented kindness, the loud talks with Chris and Andrea, living with JB, the river-beers during the pandemic

with Andrei and the every day laughter are just a few stories that I keep to myself. I found way more fantastic people that what I expected.

To Juli Gargiulo, who I had the pleasure to meet at my arrival, and work during his second stay. For the insightful discussions and for pushing me these lasts days to finish. Thanks for your friendship julito!

To perhaps one of the most important people in this thesis. Ana Sousa Castillo, it is fun that our chemistry was fantastic from the beginning. Thanks for teaching me, for always pushing me to work even though things were not going so well, and always welcome my suggestions. For singing and laughing all day long in the chem lab! I want to meet Lola.

I also want to thank my little Argentinian community, Centro Argentino de Munich. The football and barbecues help me to deal with the loneliness of Sundays in the best way.

Nereo Delgado, Cris Ayllon and Anouk, you made me feel part of your family, specially during the pandemic. This was more than lovely from you.

To my friends in Argentina, who always made me know how happy they were for me and waited for me every summer to celebrate as in the old days.

I want to finish with my family. My parents Daniela y Daniel, my siblings Martin, Rodrigo, Pablo y Lucia, my sisters-in-law Vale y Caro, and my charming nephews and nieces: Pipi, Maria Emilia, Manu, Pedro y Valen. Your love is what encouraged me to endure the first tough months and to continue pursuing my dreams. I still remember how hard was for us the first farewell and want you to know that it has not gotten easier for me. I love you all.